Multimodal and multiscale characterization of bone and bone interfaces in health and disease

Chiara Micheletti

Department of Biomaterials

Institute of Clinical Sciences

Sahlgrenska Academy, University of Gothenburg

UNIVERSITY OF GOTHENBURG

Gothenburg 2023

Cover illustration: Examples of multimodal and multiscale characterization of bone and bone interfaces from the studies in this thesis, including both images and hyperspectral maps, as well as two- and three-dimensional techniques. Illustration by Chiara Micheletti.

Multimodal and multiscale characterization of bone
and bone interfaces in health and disease

Thesis in cotutelle with McMaster University,
Department of Materials Science and Engineering
Hamilton, ON, Canada

chiara.micheletti@biomaterials.gu.se
michelec@mcmaster.ca

ISBN 978-91-8069-183-3 (PRINT)
ISBN 978-91-8069-184-0 (PDF)
http://hdl.handle.net/2077/75903

Printed by Stema Specialtryck AB, Borås, Sweden 2023

SVANENMÄRKET
Trycksak
3041 0234

For the things we have to learn before we can do them,
we learn by doing them.

Aristotle

Abstract

Seeing is believing. Our understanding of phenomena often involves their direct observation. However, bone architecture is challenging to visualize given its multi-level hierarchical organization. In this thesis, bone and bone interfaces are characterized via multimodal and multiscale platforms, combining different techniques across several length scales. Imaging techniques across the micro-nano continuum are complemented by spectroscopy methods to explore, respectively, the structure and composition of bone and bone interfaces, using both light and electron probes. By applying a characterization methodology more typical of materials science, this thesis aims to unveil structural and compositional abnormalities of bone induced by disease [Papers I-II], and bone response to functionalized biomaterials in compromised conditions [Papers III-IV]. Additionally, it expands three-dimensional (3D) characterization opportunities at the nanoscale in both native and peri-implant bone [Papers V-VI].

This characterization approach uncovered changes in bone quality (structure and/or composition) in the compromised conditions under investigation in this thesis, i.e., leptin receptor (LepR) deficiency and medication-related osteonecrosis of the jaw (MRONJ) [Papers I-II]. In a preclinical model of LepR deficiency for type 2 diabetes/obesity, multimodal characterization of bone at the microscale showed structural abnormalities indicative of delayed skeletal development, despite unaffected bone matrix composition [Paper I]. A combination of multiscale imaging and spectroscopy techniques spanning the micro-to-nanoscale enabled a detailed study of the interface between necrotic bone and bacteria in a case of MRONJ, shedding light on possible mechanisms of bone degradation. When applied to bone-biomaterial interfaces, the application of a multimodal and multiscale characterization workflow informed perspectives on bone response to novel biomaterial solutions aimed to promote osseointegration in osteoporotic conditions via local drug delivery of phytoestrogens [Paper III] or anabolic agents [Paper IV]. This highlighted the importance of studying peri-implant bone at the mesoscale [Paper III] and of confirming biomaterial behaviour *in vivo* in the presence of surface functionalization [Paper IV]. Lastly, this thesis emphasized the importance of 3D imaging at the nanoscale with electron tomography to resolve bone ultrastructure at biomaterial interfaces [Paper V] and in native conditions [Paper VI]. Specifically, in Paper VI, artifact-free on-axis electron tomography resolved some long-debated aspects regarding the organization of mineralized collagen fibrils, the fundamental building block units of bone.

Keywords: *bone; osseointegration; characterization; mineralization; ultrastructure; diabetes; osteoporosis; MRONJ; surface functionalization; local drug delivery; titanium; bioactive glass; imaging; spectroscopy; microscale; nanoscale; micro-computed X-ray tomography; micro-Raman spectroscopy; scanning electron microscopy; transmission electron microscopy; PFIB-SEM tomography; electron tomography.*

Sammanfattning på svenska

Så som flera ordspråk säger, ”man tror på det man kan se” och ”en bild säger mer än tusen ord”, är visuella avbildningar av fenomen viktig för vår förståelse och kunskapsutveckling. Med den utgångspunkten så tar denna avhandling ett kliv mot en ökad förståelse och kunskap om den strukturella uppbyggnaden av benvävnad och dess gränssnitt mot biomaterial. Genom en kombination av flera olika avbildnings- och analystekniker, som spänner över flera längdskalor, kan den fascinerande hierarkiska strukturen av benvävnad fastställas på ett bättre sätt, från makro via meso till nanonivå. Ett vanligt ljusoptiskt mikroskop har begränsningar i upplösning vilket kan överkommas genom att istället använda elektroner som källa för avbildning och analys, där nanometerupplösning tillåts. Dessa tekniker är främst utvecklade för materialvetenskap och dess användning för att förstå hur vanliga folksjukdomar som diabetes och benskörhet påverkar vår benvävnad [artikel I och II], samt benförankring av implantat [artikel III och IV] utvärderas i denna avhandling. Dessutom ger dessa tekniker möjligheten till att med bevarad nanometerupplösning skapa 3D avbildning av både benvävnad och dess gränszon mot biomaterial [artikel V och VI].

I artikel I utvärderas en ny preklinisk modell för diabetes typ2/fetma, en folksjukdom som ökar i prevalens, och mer kunskap om dess påverkan på skelettet är viktig. Resultatet visar på strukturella avvikelser som pekar mot en försenad, långsammare utveckling av skelettet trots att den kemiska sammansättningen och mekaniska egenskapen lokalt verkar vara opåverkad. I artikel II studeras benbiopsier uttagna efter osteonekros i käken med en kombination av avbildning och spektroskopitekniker som spänner över mikro-till-nanoskala. Detta möjliggör en detaljerad bild av hur gränssnittet mellan nekrotiskt ben och bakterier ser ut, och belyser möjliga mekanismer för hur benvävnaden bryts ned. I nästföljande artiklar tillämpas denna analysstrategi på gränssnitt mellan ben och biomaterial och ger ett perspektiv på hur benresponsen sker för nya biomateriallösningar som syftar till att främja benförankringen och osseointegrationen i benskört tillstånd via lokal läkemedelsfrigivning. Dessa studier visar vikten av att studera benvävnad även i mesonivå för att bättre förstå benvävnads uppbyggnad under läkning [artikel III], samt hur tillväxtläkemedel hämmar den negativa effekten av benskörhet under läkningsprocessen [artikel IV]. Slutligen visar denna avhandling vikten av tredimensionell avbildning med nanometers upplösning för att förstå ultrastrukturen i benvävnaden som ansluter till ett biomaterial [artikel V], samt vår kunskap om hur benvävnad är uppbyggd på dess minsta nivå [artikel VI]. Specifikt ger analysstrategin i artikel VI med korrelativ strukturell och kemisk analys i 3D, ett tydligt bevis på hur det mineraliserade kollagenet i benvävnad är uppbyggt, något som har varit debatterat genom åren.

List of papers

This thesis is based on the following studies, referred to in the text by their Roman numerals.

I. Micheletti C, Jolic M, Grandfield K, Shah FA, Palmquist A. Bone structure and composition in a hyperglycemic, obese, and leptin receptor-deficient rat: Microscale characterization of femur and calvarium. Bone. 2023;172:116747.

II. Micheletti C, DiCecco L-A, Larsson Wexell C, Binkley DM, Palmquist A, Grandfield K, Shah FA. Multimodal and multiscale characterization of the bone-bacteria interface in a case of medication-related osteonecrosis of the jaw. JBMR Plus. 2022;6:e10693.

III. Micheletti C, DiCecco L-A[#], Deering J[#], Chen W, Ervolino da Silva AC, Shah FA, Palmquist A, Okamoto R, Grandfield K. Micro-to-nanoscale characterization of the osseointegration and lacuno-canalicular network at the interface with an additively manufactured implant for local genistein delivery. *Submitted for publication.*
[#]Equal contribution.

IV. Gomes-Ferreira PHS, Micheletti C, Buzo Frigério P, de Souza Batista FR, Monteiro NG, Bim-júnior O, Lisboa-Filho PN, Grandfield K, Okamoto R. PTH 1-34-functionalized bioactive glass improves peri-implant bone repair in orchiectomized rats: Microscale and ultrastructural evaluation. Biomater Adv. 2022;134:112688.

V. Micheletti C, Gomes-Ferreira PHS, Casagrande T, Lisboa-Filho PN, Okamoto R, Grandfield K. From tissue retrieval to electron tomography: Nanoscale characterization of the interface between bone and bioactive glass. J R Soc Interface. 2021;18:20210181.

VI. Micheletti C, Shah FA, Palmquist A, Grandfield K. Shedding light (… electrons) on human bone ultrastructure with correlative on-axis electron tomography and energy-dispersive X-ray spectroscopy tomography. *Submitted for publication.*
Preprint available in *bioRxiv*, DOI: 10.1101/2023.04.20.537681.

Additional publications not included in the thesis:

I. Micheletti C, Hurley A, Gourrier A, Palmquist A, Tang T, Shah FA, Grandfield K. Bone mineral organization at the mesoscale: A review of mineral ellipsoids in bone and at bone interfaces. Acta Biomater. 2022;142:1–13.

II. Grandfield K, Micheletti C, Deering J, Arcuri G, Tang T, Langelier B. Atom probe tomography for biomaterials and biomineralization. Acta Biomater. 2022;148:44–60. *Invited article.*

III. Fu L[#], Williams J[#], Micheletti C, Lee BEJ, Xu G, Huang J, Engqvist H, Xia W, Grandfield K. Three-dimensional insights into interfacial segregation at the atomic scale in a nanocrystalline glass-ceramic. Nano Lett. 2021;21:6898–6906. [#]Equal contribution.

IV. Shah FA, Jolic M, Micheletti C, Omar O, Norlindh B, Emanuelsson L, Engqvist H, Engstrand T, Palmquist A, Thomsen P. Bone without borders – Monetite-based calcium phosphate guides bone formation beyond the skeletal envelope. Bioact Mater. 2023;19:103–114.

Content

Abbreviations

2D	Two dimensions, two-dimensional
3D	Three dimensions, three-dimensional
4D	Four dimensions, four-dimensional
AGE	Advanced glycation end-product
AM	Additive manufacturing, additively manufactured
APT	Atom probe tomography
BF	Bright-field
BIC	Bone-implant contact
BMD	Bone mineral density
BSE	Backscattered electron
Cp-Ti	Commercially pure titanium
EDX	Energy-dispersive X-ray spectroscopy
EELS	Electron energy loss spectroscopy
FIB	Focused ion beam
HAADF	High-angle annular dark-field
LCN	Lacuno-canalicular network
Lep	Leptin
LepR	Leptin receptor
L-PBF	Laser powder bed fusion
MetS	Metabolic syndrome
Micro-CT	Micro-computed X-ray tomography
MRONJ	Medication related osteonecrosis of the jaw
ORX	Orchiectomy, orchiectomized
OVX	Ovariectomy, ovariectomized
PFIB	Plasma focused ion beam
PTH	Parathyroid hormone
qBEI	Quantitative backscattered electron imaging
ROI	Region of interest
RPI	Reference point indentation
SAED	Selected area electron diffraction
SE	Secondary electron
SEM	Scanning electron microscopy
SIRT	Simultaneous iterative reconstruction technique
STEM	Scanning transmission electron microscopy
T2DM	Type 2 diabetes mellitus
TEM	Transmission electron microscopy
TMD	Tissue mineral density
Z	Atomic number

Introduction

This chapter introduces relevant background information to the studies in this thesis.

In the first section, the multiscale, hierarchical structure of bone is described, with a focus on the main components (collagen fibrils and mineral) and on the mineralized collagen fibril. Concepts related to how bones form, model, and remodel are also reviewed. Bone repair and regeneration following biomaterial implantation, i.e., osseointegration, are explained especially in relation to the two biomaterials examined in this thesis, i.e., titanium and bioactive glass [Papers III-V]. Some notions on surface functionalization for local drug delivery are also provided, given its relevance to this thesis [Papers III-IV].

In the second section, an introduction to bone density (quantity) and quality is provided, followed by their contextualization in the two diseased conditions relevant to this thesis, i.e., diabetes mellitus and osteoporosis. An overview of the main therapies used in osteoporosis is given, together with some reported side effects, specifically osteonecrosis of the jaw, as these aspects are relevant to Papers II-IV.

In the third and last section, technical information and example applications of the main techniques used in this thesis to characterize bone and bone interfaces are reviewed.

BONE

Bones in the skeletal system of vertebrates play paramount functions in the body, from protecting internal organs, to working in concert with muscles and other connective tissues to allow the body to move; from storing minerals like calcium and phosphorus, to releasing them when needed[1]. To fulfill the requirements set by evolution, bones need to be lightweight, capable to adapt to the external stimuli and self-repair, and at the same time tough and strong[2]. It is this unique combination of strength (i.e., resistance to non-recoverable deformation) and toughness (i.e., resistance to fracture), which is hard to achieve in material design, that has prompted research to unveil structural-functional relationships in bone to learn from nature to inspire biomimetic design[3]. In a sense, nature has "engineered" bones with an exquisite architecture to serve specific structural demands, in addition to key biological functions.

Bone matrix is composed of organic (24 wt%) and inorganic elements (70 wt%), together with water (6 wt%)[4]. The organic phase mostly comprises type I collagen (85-90%), in addition to a small fraction of non-collagenous proteins[5]. The inorganic phase is a calcium phosphate mineral similar to hydroxyapatite [$Ca_{10}(PO_4)_6(OH)_2$], substituted with carbonate [CO_3^{2-}] (up to 6 wt%) and other elements (e.g., magnesium and sodium)[6]. It is the hierarchical organization of the organic and inorganic components across multiple length scales that imparts strength and toughness to the bone matrix[7–9]. Specifically, collagen and mineral contribute to elasticity and stiffness, respectively[10]. Water also plays a role, increasing the deformability of collagen[5] and affecting the viscoelastic behaviour of bone[11]. The interplay between collagen and mineral makes bone a composite material, which has the "mineralized collagen fibril" as its building block unit at the nanoscale[9,12]. The term "bone" may actually be used in reference to a family of materials (more precisely, biogenic minerals) sharing the mineralized collagen fibril as their structural nanoscopic module[7]. Other than bone tissue in the vertebrate skeleton, other members of the bone family are dentin, cementum, and mineralized tendons. In this thesis, the term "bone" is used to indicate skeletal bone tissue, mostly in reference to bone matrix only.

Bone hierarchical structure

As mentioned above, the mineralized collagen fibril is just the building block for a highly complex hierarchical structure, as shown in Figure 1. At the molecular level, three polypeptide chains of type I collagen (two α_1 chains and one α_2 chain) are twisted in a right-handed triple helix, forming tropocollagen molecules that are 1.5 nm in diameter and 300 nm in length[13]. Tropocollagen molecules self-arrange in a quarter-staggered fashion creating a 67 nm-periodicity of alternating gap (40 nm) and overlap regions (27 nm)[14]. Such an assembly, 80-100 nm in diameter but with unspecified length, is commonly referred to as the "collagen fibril"[9,15].

Collagen fibrils are mineralized into what becomes the "mineralized collagen fibril". The exact spatial relationship between mineral and collagen in the mineralized collagen fibrils has been debated over the years, leading to different ultrastructural models being proposed. Overall, it is now accepted that mineralization occurs both inside an individual fibril, mainly in the gap regions (intra-fibrillar mineralization)[16], and on the fibril's outer surface, hence in between neighbouring fibrils (extra- or inter-fibrillar mineralization)[17]. However, while early investigators suggested that most of the mineral is located within the gap zones, eventually extending into the overlap regions[16,18], others have indicated that mineral is mainly extra-fibrillar[19,20], and it is organized in stacks of plates called "mineral lamellae", which wrap around the fibrils[21]. More recently, the mineral phase has been shown to exceed the dimensions of a single fibril, spanning several fibrils instead (cross-fibrillar mineralization)[22,23]. However, none of the different models for the spatial organization of collagen fibrils and mineral crystals proposed to date has been fully adopted by the entire bone research community. This is studied in this thesis in Paper VI.

Mineral crystals are aligned with their longest dimension, i.e., the *c*-axis of the unit cell, to the long axis of the collagen fibrils[24,25]. The crystals are typically described as plate-shaped, 50 nm in length[26], 25 nm in width[26], and 2-4 nm in thickness[27], but varying dimensions and morphologies, specifically needles/rods instead of plates[23,28–30], have also been reported[6]. Mineral plates aggregate into larger assemblies, becoming themselves a hierarchical structure[23]. At the mesoscale, i.e., at a level connecting the nano- and microscale, mineral aggregates have the geometrical shape of ellipsoids[22,31,32]. Mineral ellipsoids have been only recently identified, but they appear to be ubiquitously found in native bone and at bone interfaces in different species and anatomical locations, as reviewed by the author of this thesis (see reference 33).

At the next levels in bone's multiscale architecture, mineralized collagen fibrils are assembled in bundles, which in turn are organized in arrays whose pattern varies based on the type of bone, i.e., lamellar *vs.* woven *vs.* parallel fibered[9]. In lamellar bone, which is the dominant type in the skeleton of humans and other mammals[8], fibril bundles 1-3 μm in size[34] are organized in 2-6 μm thick sheets called "lamellae"[5]. In addition to lamellae in circumferential lamellar bone, two structural motifs can be identified in lamellar bone, i.e., trabeculae and osteons. Lamellae are organized in packets with slightly different orientations in the trabeculae, while they form concentric layers around blood vessels in the osteons[9]. In particular, secondary osteons, which form as a result of bone remodeling, are also sometimes referred to as the "Haversian system", as the lamellae encircle the Haversian canal, which hosts blood vessels and nerves[5]. Osteonal lamellar bone is commonly described as a twisted/rotated plywood structure, where arrays of mineralized collagen fibrils are oriented at different angles in different (sub)lamellae[35,36]. However, other models have also been proposed[37].

Lastly, at the whole bone level, i.e., macroscopically, compact and trabecular bone can be distinguished. Compact bone is the outer, dense shell that encloses a porous, sponge-like interior, i.e., trabecular bone.

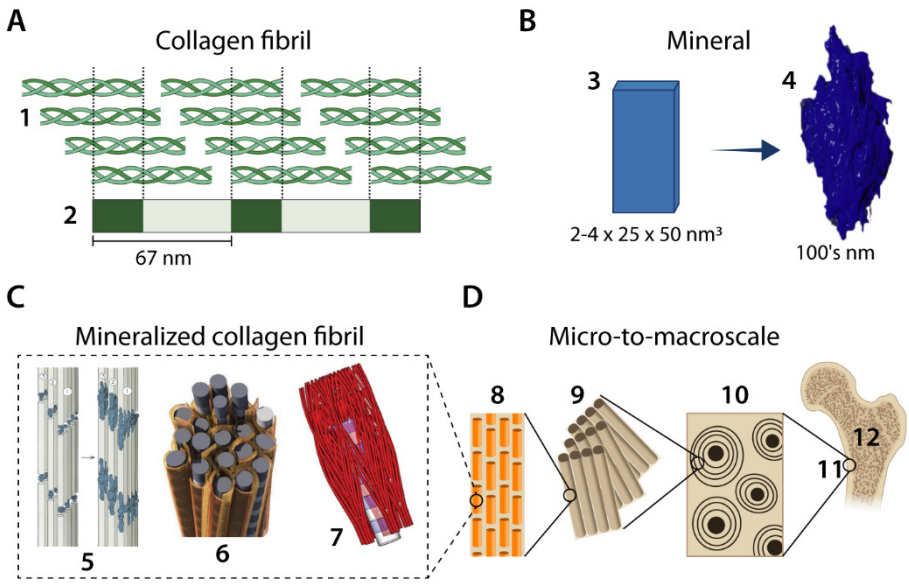

Figure 1. *Schematic representation of bone hierarchical structure, starting from the two main components, i.e., collagen fibrils (A) and mineral (B). In A, arrays of tropocollagen molecules (1) are staggered to form a collagen fibril, characterized by alternating gap (dark-coloured) and overlap (light-coloured) regions with 67 nm periodicity. In B, mineral platelets (3) assemble in ellipsoidal-shaped structures (4). At the mineralized collagen fibril level (C), the collagen-mineral spatial relationship has been proposed to be mostly intra- (5), extra- (6), or cross-fibrillar (7). At the next levels (D), shown in detail for osteonal bone, arrays of fibrils (8) assemble in lamellae (9), which in turn are organized in a twisted/rotated plywood fashion in the osteons (10). At the whole bone level, cortical (11) and trabecular (12) bone can be distinguished. [Images numbered 4 to 7 are reproduced with permission from references 31, 38 (original from 18), 39, and 23, respectively. Images numbered 1-2 and 11-12 are created with icons from BioRender.com].*

Bone formation, modeling, and remodeling

Bones are primarily formed by either endochondral or intramembranous ossification[40–42]. Endochondral ossification proceeds through a cartilage template. As this cartilage matrix grows, it progressively calcifies and is replaced by bone tissue[1]. In intramembranous ossification, bone tissue is laid down directly (*de novo*) without the intervention of the cartilage precursor[40–42]. This ossification route is followed by several bones in the skull[40]. In general, bones grow by apposition of new tissue at the outer surface (periosteum). Long bones formed by endochondral ossification also grow longitudinally at the growth (epiphyseal) plate, which is the cartilage layer separating epiphysis and diaphysis until growth is complete in adulthood[1]. The counterpart of the growth plate in cranial bones formed by intramembranous ossification is represented by cranial sutures. Sutures act as centres of intramembranous bone growth, with new bone being deposited at their edge in response to signals from the expanding cranium[43].

During skeletal development, the size and shape of bones are adjusted through the process of "bone modeling", where bone is formed or removed by two distinct types of bone cells, i.e., osteoblasts (the bone-forming cells) and osteoclasts (the bone-resorbing cells)[40]. Bone formation and resorption during modeling occur independently from each other and are mostly initiated in response to stimuli of a mechanical nature, ensuring that the overall structure is adapted to the mechanical function[5,40]. This adaptation is exemplified by the fact that both osteons in cortical bone and trabeculae in trabecular bone are oriented along the direction of the principal stresses[1,5]. In the well-known law bearing his name, Wolff observed that the pattern of the trabeculae in the proximal femur is analogous to that of the stress trajectories in the Culmann crane[44]. Analogously, in long bones, osteons are parallel to the long axis of the bone[1].

Osteoblasts and osteoclasts work instead in a coupled manner in the process of "bone remodeling", which is at the basis of bone's dynamic nature. Every year, about 4% and 20% of cortical and trabecular bone, respectively, are replaced to remove microdamaged and old tissue, as well as to maintain bone mass and regulate mineral homeostasis[1]. A remodeling cycle is composed of five phases: i) activation, where osteoclasts are recruited at the remodeling site; ii) resorption, where bone is removed by the osteoclasts; iii) reversal, where the transition from resorption to formation occurs; iv) formation, where new bone is deposited by the osteoblasts, first in the form of an organic matrix, the osteoid, which later becomes mineralized; v) quiescence (resting), where formation stops and bone lining cells cover the quiescent bone surface[40].

Osteocytes and lacuno-canalicular network

Increasing evidence points towards the osteocytes, i.e., the resident bone cells, as having a role as orchestrators of bone remodeling[45]. Osteocytes are the most abundant type of bone cells, constituting over 90% of bone cells in the mature human skeleton[45,46] for an estimated total of 42 billion[47]. Osteocytes differentiate from osteoblasts as these become buried in their own mineralizing matrix[48]. Each osteocyte resides inside within a lens-shaped space called "lacuna" and connects with neighbouring osteocytes through its cell processes, which are housed in narrow channels, the "canaliculi"[5]. In osteonal lamellar bone, lacunae are primarily disposed in concentric layers around the Haversian canal, while canaliculi run in the orthogonal direction, i.e., perpendicular to the Haversian canal[49]. The extensive network of lacunae and canaliculi within the hierarchically structured bone matrix constitutes the so-called "lacuno-canalicular network" (LCN), which is key to the sensing and transmission of mechanical loads[45,50]. Specifically, osteocytes act as mechanotransducers, i.e., they sense mechanical strains to then coordinate the response of osteoblasts and osteoclasts[51]. Hence, osteocytes play an important part in regulating bone metabolism and bone quality[48,50], not just in native bone, but also in bone forming at the interface with biomaterials[52].

Bone repair: biomaterials and osseointegration

Bone tissue is a "smart material" capable of self-repair. Fracture healing and bone repair follow similar steps as embryonic skeletal development, specifically endochondral ossification, where bone formation is preceded by a cartilage matrix[53]. However, to augment or restore lost functions when self-repair is not enough, for example in the case of large and complex defects or compromised healing conditions, biomaterials are often needed. In addition to common biomaterial requirements such as biocompatibility, bone-interfacing biomaterials, such as hearing implants and endosseous dental implants, are selected also based on their ability to osseointegrate. The term "osseointegration" refers to "a direct – on light microscopic level – contact between living bone and implant"[54], although it is now clear that this contact occurs at the (sub)nanoscale, at a level beyond what light microscopy can resolve[55–57]. Various ultrastructural arrangements of the bone-implant interface have been proposed over the years, but current interpretations emphasize the role of mineralized collagen fibrils as the building blocks of the interface, similarly to native bone[56]. Interestingly, peri-implant bone initially laid down as woven bone is remodeled to closely mimic its native status. The bone-implant interface is thus hierarchical in nature, with intermixing between implant surface elements and bone at the atomic level, and mineralized collagen fibrils oriented parallel to the implant surface at the nanoscale[52,58,59]. At the microscale, osteocytes connect through their processes to the implant surface, establishing a mechanosensing-based communication pathway with the implant itself[60].

The ultimate goal of osseointegration is to close the gap between the implant and native bone with new bone. New bone formation occurs over two fronts: one directed from native bone towards the implant (distance osteogenesis), and the other directed from the implant itself towards native bone (contact osteogenesis), for which it is important that the implant surface displays optimal physicochemical properties to promote formation of bone directly on it[61].

An important distinction should be made between degradable and non-degradable implant materials. In the case of degradable materials, the bone-implant interface is not in a fixed position in the peri-implant compartment, but moves as the implant itself degrades[56]. In this thesis, both non-degradable titanium-based implants and degradable bioactive glass particles are used, hence more background information on these biomaterials are introduced in the following sub-sections.

Titanium-based bone implants

The mechanical properties of titanium, combined with its biocompatibility and corrosion resistance, make it a suitable candidate for load-bearing bone implants[62]. Commercially pure titanium (cp-Ti) and the alloy Ti-6Al-4V are extensively employed in dental and orthopedic applications, respectively[56]. Titanium spontaneously passivates in air forming a 5-10 nm-thick layer of titania (TiO_2)[63]. This surface oxide layer effectively renders the

implant a "ceramic" material from the viewpoint of the host environment, and favours osseointegration thanks to its bioactive nature[63].

The physicochemical properties of the implant surface greatly affect osseointegration outcomes[64]. Implant surface topography is often modified to introduce micro- and/or nanoscale features, which are beneficial to osseointegration[61,64–67]. Common surface modification strategies include acid etching to add sub-micron texturing to the implant surface[64]. Micro-rough surface topography can be directly obtained without the need of post-processing by additive manufacturing (AM) via powder bed fusion techniques due to residual microparticles from incomplete melting/sintering of feedstock powders[68]. AM also offers highly customizable solutions, including engineered porous implants with precise control over pore size, volume, and architecture[69,70]. Bone ingrowth can occur within the pores, increasing the area of bone-implant contact (BIC), in turn improving implant stability and osseointegration[71,72].

Bioactive glasses

Bioactive glasses are a class of silica-based bioceramics usually made of SiO_2, Na_2O, CaO, and P_2O_5. Specifically, the first developed bioactive glass, 45S5 Bioglass®, has the following composition by weight: 45 wt% SiO_2; 24.5 wt% Na_2O; 24.5 wt% CaO; and 6 wt% P_2O_5 [73]. This is analogous to Biogran® used in this thesis [Papers IV-V], which is a bioactive glass commercialized in the form of granules typically 300-360 μm in size. Biogran® granules are used in the clinical practice as fillers to augment bone volume, for example to elevate the sinus floor prior to implant installation in edentulous patients[74].

Bioactive glasses display high surface reactivity *in vivo*, making them chemically bond with bone. On the biomaterial side, five reactions take place: i) leaching, i.e., release of alkali and alkaline elements via ion exchange; ii) dissolution through breaking of –Si–O–Si– bonds; iii) formation of a SiO_2-rich gel; iv) migration of Ca^{2+} and PO_4^{3-} to the SiO_2-rich surface and formation of a CaP-rich outer layer around the Si-rich gel core; v) crystallization of the CaP layer[75]. On the host side, phagocytosing cells reach the Si-rich core through cracks in the CaP-rich outer layer and start resorbing it[76]. Undifferentiated mesenchymal cells also migrate through these cracks and adhere to the CaP surface, which triggers their differentiation into osteoblasts, likely due to its bone-like composition[76]. Osteoblasts then start depositing new bone, promoting osseointegration via contact osteogenesis.

Surface functionalization for local drug delivery

Not only can the surface of biomaterials be modified to optimize its physical and/or chemical properties, but it can also be functionalized to deliver specific molecules and therapeutic agents locally at the implant site[77]. Local drug delivery presents advantages over conventional systemic administration in terms of tuning drug concentration and bioavailability at the site of interest, and avoiding adverse side effects in unaffected parts of the body. Enhancing bone response in the peri-implant space by local release of therapeutics can especially be useful when systemic conditions compromise bone repair

and regeneration[78]. For example, in a study by Bai et al., a porous titanium scaffold fabricated by AM was injected with a hydrogel loaded with a common medication to treat osteoporosis, which was released *in vivo* upon hydrogel degradation, in turn improving osseointegration in osteoporotic rabbits[79]. In this thesis, surface functionalization of two different biomaterials (titanium and bioactive glass) for local drug delivery purposes is explored to promote osseointegration in osteoporotic-like conditions [Papers III-IV]. The specific therapeutic agents used in those studies are introduced in the *Osteoporosis* section (see page 12).

BONE QUANTITY AND QUALITY IN DISEASE

The hierarchical organization of bone and its maintenance through modeling and remodeling are essential to the mechanical functioning. Imbalances in bone remodeling, with bone resorption prevailing over formation, or vice versa, can lead to sub-optimal bone mass. A parameter routinely monitored in the clinical practice is bone mineral density (BMD), which represents the amount of bone mass per unit volume (expressed in g/cm^3) and is typically measured by dual-energy X-ray absorptiometry[80]. However, BMD is not the sole determinant of bone fragility. In addition to this quantity-related metric, the concept of "bone quality" has been developed to encompass "the totality of features and characteristics that influence a bone's ability to resist fracture"[81]. These features are mostly bone material properties related to its structure (e.g., shape, micro-architecture, micro-porosity) and composition (e.g., degree of mineralization, properties of bone mineral and/or collagen)[82,83].

The increase in bone fragility that accompanies aging and/or diseases can often be attributed to altered bone turnover, affecting bone quantity, and/or to structural and compositional changes deteriorating bone quality[83,84]. Hereinafter, abnormalities in bone quantity and quality will be reviewed in greater detail for diabetes mellitus, especially type 2, and osteoporosis, which are relevant to this thesis.

Diabetes mellitus

Diabetes mellitus is a "group of metabolic disorders characterized and identified by the presence of hyperglycemia in the absence of treatment"[85]. Chronic hyperglycemia is due to abnormal functioning of pancreatic β-cells, which are responsible for secreting insulin, the hormone controlling blood glucose levels. According to the World Health Organization, 422 million people were affected by diabetes mellitus in 2014[86]. The vast majority (90-95%) of cases are of type 2 diabetes mellitus (T2DM), characterized by insulin resistance[85]. Other common forms of diabetes include type 1 diabetes, which is an autoimmune disease leading to β-cell destruction and insulin deficiency, and gestational diabetes[85].

The number of people with diabetes has been rising over the past three decades. In particular, T2DM is now considered epidemic, as sedentary lifestyles have contributed to an increasing prevalence of obesity, which is a significant risk factor for T2DM[87]. T2DM often co-exists not only with obesity, but also with other metabolic disturbances, creating a cluster of conditions labelled as "metabolic syndrome" (MetS), which increases the susceptibility to cardiovascular disease[88].

The metabolic changes caused by diabetes and/or obesity affect many organs and tissues, including bone. Individuals with T2DM are at greater risk of bone fractures, yet they often display a normal or even higher BMD compared to healthy individuals[89]. While this

apparent contradiction could be in part attributed to collateral effects such as a greater likelihood of falls[90], the overall reduction in bone strength can be explained by changes in bone material properties, i.e., bone quality[84,91]. A positive correlation between BMD and body weight, as well as fat and lean mass, is commonly reported[92] and attributed to skeletal adaptation to mechanical stimuli, with increased loading promoting bone formation[93]. This regulation pathway of bone mass related to mechanical loading has been termed as the "mechanostat"[94].

The accumulation of advanced glycation end-products (AGEs) in hyperglycemia is often indicated as one of the main culprits of the increase in skeletal fragility in T2DM[91]. Cross-linking types of AGEs like pentosidine induce non-enzymatic cross-linking of collagen, which causes fibril embrittlement[95]. Together with non-crosslinking types of AGEs, such as carboxymethyl-lysine, the interaction between AGE and its receptor induces oxidative stresses and inflammation[96], with consequences on osteoblastic and osteoclastic activity.

Hyperglycemia and obesity have been associated with a low rate of bone turnover. One of the possible explanations is that adipogenesis is favoured over osteoblastogenesis in obesity due to the preferential differentiation of mesenchymal stem cells in adipocytes rather than osteoblasts[97]. The AGE-AGE receptor axis and oxidative stresses play a role in bone formation, with higher levels of AGEs and oxidative stresses leading to reduced osteoblast proliferation and differentiation[98,99]. It remains controversial whether and how osteoclastic activity is affected by T2DM. Chronic inflammation in obesity appears to increase the production of pro-inflammatory cytokines that stimulate osteoclast-induced bone resorption through the activation of the osteoprotegerin/RANKL (RANK-ligand)/RANK (receptor activator of nuclear factor kappa-B) pathway[100].

Leptin and bone metabolism

Energy and bone metabolism are interconnected through the action of leptin. Leptin is an adipokine, i.e., a cytokine produced by the adipose tissue, responsible for controlling energy storage and appetite[101]. For example, low leptin levels during starvation stimulate appetite. Leptin acts directly on bone cells and indirectly on bone metabolism via the hypothalamus and sympathetic nervous system[102]. Inconsistencies in the indirect effects of leptin on bone mass have been reported. In general, leptin displays an anabolic action through the peripheral pathway and a catabolic effect through the central pathway[103], although deviations from this behaviour have also been reported[104].

Given the effect of leptin on bone metabolism, various animal models employed in T2DM research have mutations in the gene encoding leptin (Lep) or its receptor (LepR). Abnormal leptin signaling results in hyperphagia, hence Lep/LepR-deficient animals become obese, in turn displaying hyperglycemia and impaired glucose tolerance analogously to T2DM conditions[105]. T2DM etiology in humans does not typically involve genetic mutations, but some rare cases of humans with Lep/LepR mutations, causing severe obesity at an early age, have been reported[106–109]. A novel monogenic obese rodent model, the Lund MetS rat[110], is examined in this thesis [Paper I].

Osteoporosis

Osteoporosis, or "porous bone disease", has been defined as a "systemic skeletal disease characterised by low bone mass and microarchitectural deterioration of bone tissue with a consequent increase in bone fragility and susceptibility to fracture"[111]. Osteoporosis is typically associated with aging, although it can also develop as "secondary osteoporosis", for example due to glucocorticoids therapies (steroid-induced osteoporosis)[112]. Osteoporosis-related fragility fractures, i.e., fractures occurring at low-to-moderate levels of trauma, account for around 60% of all bone fractures in individuals above 50 years of age[113]. As the aging population keeps surging across the globe[114], the diagnosis, prevention, and treatment of osteoporosis become increasingly important for the quality of life of the senior population, as well as the economic burden on the health care system.

Osteoporosis is characterized by low bone mass. In the diagnosis of osteoporosis, BMD is typically expressed as the "T-score" in terms of standard deviation from the mean value in the young healthy population. A T-score below -2.5 is indicative of osteoporosis, between -1 and -2.5 determines osteopenia, and above -1 is considered normal[80]. Loss in bone mass in osteoporosis is due to imbalanced bone remodeling with bone resorption prevailing over bone formation[112]. This naturally occurs with aging due to the decline in hormone levels, especially estrogen, which affect bone metabolism. The effects of aging-related hormone deficiency on bone strength are especially apparent in postmenopausal women, and age-adjusted fracture risk is significantly higher in female than male individuals[113].

Estrogen is the main hormonal regulator of bone metabolism in both sexes[115]. Estrogen has direct effects on various bone cells, specifically decreasing apoptosis of osteocytes and osteoblasts, and, conversely, increasing apoptosis of osteoclasts and decreasing their formation and activity[115,116]. Estrogen appears to modulate strain sensing via the "mechanostat"[94], and it is involved in the intestinal absorption of calcium and its renal conservation[116]. Collectively, direct and indirect effects of estrogen on bone metabolism make bone resorption outweigh bone formation in contexts of estrogen deficiency, such as after menopause[116]. In male individuals, estrogen bioavailability decreases with age[117]. Additionally, androgen levels affect bone remodeling. This is mostly noted in androgen deprivation therapy to treat prostate cancer (chemical/surgical castration), where lower levels of androgen lead to an increased rate of bone loss[118,119].

Because of the role of sex hormones in bone metabolism, widespread animal models used in osteoporosis research are subjected to gonadectomy surgery, i.e., ovariectomy (OVX) in females and orchiectomy (ORX) in males. The OVX rat is especially used to mimic postmenopausal osteoporosis[120,121]. While aged rats represent a more accurate model, mature rats are typically preferred due to their lower cost and greater availability[121]. The male counterpart is the ORX rat, which mimics conditions of androgen deprivation[122].

Not only bone density, but also bone quality is affected by osteoporosis. Deterioration in bone microarchitecture is especially apparent in the trabecular compartment, with

reduction in bone volume and trabecular thickness and/or number[121]. Other changes have been reported in both bone structure and composition, e.g., increased cortical porosity, greater mineral crystallinity, and lower mineral heterogeneity[83,84].

Given the altered bone metabolism, it is reasonable to postulate that bone healing at a biomaterial interface may be compromised in osteoporotic individuals. However, there is no clear consensus on the effect of osteoporosis on osseointegration, and osteoporosis is not typically considered a contraindication to the installation of bone implants[123]. On the other hand, it is known that bone quantity and quality are key parameters to successful osseointegration[124]. The systemic alteration in bone metabolism, as well as the deteriorated bone structure, could affect primary implant stability and early biological fixation, in turn compromising osseointegration[125]. Slower osseointegration, higher failure rates and peri-implant bone loss, and lower values of BIC have been reported for implants placed in osteoporotic bone[123,125–127]. Bone healing and osseointegration in OVX/ORX rat models are studied in this thesis in Papers III-IV, especially to examine the effect of local drug delivery on bone repair using some of the therapeutic agents described below.

Common and emerging therapies

Therapies to counteract bone loss are administered to both osteoporotic individuals and to those deemed at high risk of fracture in order to prevent this from occurring. Commonly used medications are anti-resorptive agents, but anabolic therapies are also available. The therapeutic agents to treat osteoporosis relevant to this thesis [Papers II-IV] are briefly discussed hereinafter.

Anti-resorptive medications are the gold standard in the treatment of osteoporosis, acting to suppress bone resorption. In this group, bisphosphonates are widely used to treat skeletal disorders, not just limited to osteoporosis but also skeletal complications due to metastatic cancer[128]. With a composition similar to that of pyrophosphates, i.e., mineral inhibitors found in the body fluids[129], bisphosphonates can inhibit mineralization and prevent the breakdown of hydroxyapatite crystals when bound to their surface[130,131]. Bisphosphonates also display toxicity towards osteoclasts, and limit their formation and activity[128].

Possible treatment alternatives are based on hormone replacement, specifically of estrogen, as bone loss post-menopause is primarily caused by estrogen deficiency[112]. However, hormone replacement therapy may have significant side effects, as an increased incidence of breast cancer has been reported[132]. Lower breast cancer rates have instead been noted for individuals consuming diets rich in phytoestrogens found, for example, in isoflavones in soybeans[133]. Therefore, phytoestrogens could offer an alternative treatment for osteoporosis while avoiding harmful side effects. An example of isoflavone used in this thesis is genistein [Paper III]. Genistein has shown a positive effect on bone mass on postmenopausal individuals treated in a randomized trial[134]. However, the use of genistein in bone applications has mostly been explored via systemic administration and not locally as investigated in Paper III.

Differently from anti-resorptive medications, anabolic agents act by enhancing bone formation in the remodeling cycle[135]. The 1-34 fragment of parathyroid hormone (PTH), teriparatide (PTH 1-34), was the first anabolic drug approved for clinical use in osteoporosis. Its intermittent use has anabolic effects on bone, for example via promotion of osteoblastogenesis, suppression of sclerostin, and hinderance of osteoclast differentiation[136]. In this thesis, the influence of PTH 1-34 administration on osseointegration in osteoporotic-like conditions is studied in the context of local delivery in the peri-implant space via surface functionalization of bioactive glass [Paper IV].

Side effects of bisphosphonates: osteonecrosis of the jaw

A prolonged or high-dose intake of bisphosphonates has been associated with a greater risk of developing medication-related osteonecrosis of the jaw (MRONJ)[137–140]. According to the American Association of Oral and Maxillofacial Surgeons, MRONJ can be diagnosed when necrotic bone in the jaw does not heal within eight weeks after intervention in an individual without any metastasis or history of radiation therapy in that area[140]. The pathogenesis of MRONJ is still not fully elucidated due to its complexity and multi-factorial nature. Possible causes include the unresponsive status of bone where resorption is suppressed, and the impaired healing due to toxicity of bisphosphonates to cells of the soft tissue and immune system[141,142]. Bacteria are commonly found at the necrotic sites in the jaw, but the causal/temporal relationship between infection and necrosis is not fully understood[142–144]. This thesis includes a study on the effect of bacteria on bone matrix properties and degradation in a case of MRONJ [Paper II].

MULTISCALE ANALYTICAL TOOLS FOR BONE AND BONE INTERFACES

Owing to its hierarchical architecture spanning from the macro- to the nanoscale, the structure and composition of bone, both native and at biomaterial interfaces, can be examined using a plethora of techniques, each addressing specific features of interest at certain levels in its hierarchy. In other words, comprehensive characterization of bone and bone interfaces is best done by adopting a multiscale approach, correlating information acquired over multiple length scales[55,57,145,146]. This thesis applies a multiscale characterization platform, which is often also multimodal, i.e., different techniques based on dissimilar working principles are used, and sometimes multidimensional, combining two- and three-dimensional (2D and 3D) data. Hereinafter, a review of the technical details of the main characterization tools used in this thesis is provided, together with relevant examples from the literature of their application in the study of bone and bone-biomaterial interfaces. The characterization techniques described are organized based on the nature of the main information provided, i.e., structural or compositional. The typical spatial (lateral) resolution and field of view analyzed are graphically represented in reference to bone structure in Figure 2.

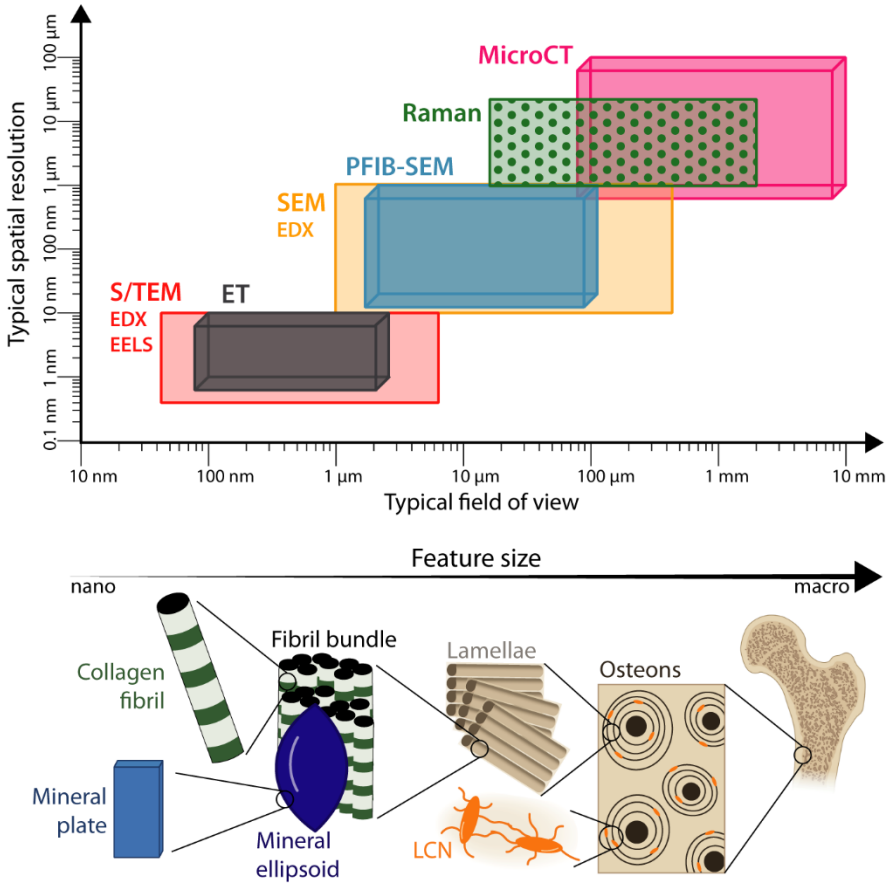

Figure 2. *Graph showing the typical field of view and spatial resolution for the main characterization techniques used in this thesis, in relation to relevant features in bone hierarchical structure. In the graph, the following abbreviations are used: micro-CT (micro-computed X-ray tomography); Raman (micro-Raman spectroscopy); SEM (scanning electron microscopy); PFIB (plasma focused ion beam); S/TEM (scanning/transmission electron microscopy); ET (electron tomography); EDX (energy-dispersive X-ray spectroscopy); and EELS(electron energy loss spectroscopy). 2D and 3D techniques are shown as rectangles and cuboids, respectively. A dotted pattern is used for the purely spectroscopy technique to differentiate it from the imaging techniques used for structural characterization (unless combined with spectroscopy as in SEM/STEM-EDX or STEM-EELS).*

Characterization of bone structure

Light probes: optical microscopy and micro-CT

Visible light microscopy

The most immediate tool to produce magnified images of bone structure is the optical microscope, or, more precisely, the visible light microscope. Imaging of bone with light microscopy dates back to the 17th century where some structural elements now known as lamellae and osteons were visualized[9]. In the 1960s, Brånemark's discovery that bone can form a direct contact with titanium was based on light microscopy observations, and in fact the term osseointegration was first defined "on light microscopic level"[54]. Light microscopy remains the primary tool used in histology to examine bone tissue, including at biomaterial interfaces, both quantitatively and qualitatively. Quantitatively, bone histomorphometry provides information on four types of measurements, i.e., area, length (perimeter or boundary), distance between points/lines, and number of some features of interest (e.g., cells)[147]. Qualitatively, histological sections provide information on the general morphology and structural patterns (e.g., woven *vs.* lamellar bone), the state of the tissue (e.g., signs of necrosis), and which cells are present in it (e.g., bone cells, but also from nearby tissues other than bone), especially when specific features can be enhanced by appropriate stains[57].

Micro-computed X-ray tomography

Bone histomorphometry is performed on 2D sections, and inferring 3D information using stereology has limitations[147]. A solution is offered by micro-computed X-ray tomography (micro-CT). Micro-CT is based on X-ray absorption imaging, where images, i.e., radiographs, are formed by the X-rays transmitted through an object, which are attenuated based on absorption and density differences within the object itself and its thickness. In micro-CT experiments, the sample is mounted on a rotating stage. The stage is rotated typically over 180°-360°, and a radiograph is acquired at each rotation step. These radiographs represent 2D projections of the object at different angular positions of the stage[148]. The projections are reconstructed by specific algorithms (e.g., back-projection) to obtain a 3D representation of the object. The term "topography" (*tomos*, "section", and *graphe*, "to write") refers to this specific type of imaging based on 2D slices (projections) that are then combined to reproduce the original 3D object[55]. Some important parameters that determine the quality and resolution of the micro-CT reconstruction include the X-ray energy, intensity, and tube potential, the voxel size (pixel size in x, y, z), the duration of each projection (integration time), the number of repeated acquisitions at each step (frame averaging), and the number of projections collected, which is related to the rotation steps[149].

Micro-CT reconstructions provide an accurate 3D representation of the overall geometry and microstructure of bone or bone-biomaterial interfaces[55,57,146]. In addition to qualitative observations, various morphometry parameters can be quantified in 3D. These parameters can characterize relevant structural properties of cortical bone, such as cortical thickness, cortical bone area, and cortical area fraction, as well as properties of the trabecular compartment, such as bone volume fraction, trabecular thickness, trabecular separation, and trabecular number[149]. In micro-CT volumes of a bone sample interfacing with a biomaterial, BIC can be quantified. However, metal implants typically induce artifacts in the reconstruction, especially at the bone-implant interface, due to beam hardening and scattering[150], in turn challenging the reliability of BIC measurements[151]. While micro-CT primarily provides structural information, by using standards of hydroxyapatite of known density, it is possible to obtain a liner correlation between grey-levels and density, which can be used to estimate the tissue mineral density (TMD) of bone samples acquired with the same settings as the standard[149].

Electron probes: SEM, FIB-SEM tomography, S/TEM, and electron tomography

Resolution in light microscopy is diffraction-limited, as first theorized by Abbe. In electron microscopy, thanks to the much smaller wavelength of electrons compared to light, a higher spatial (lateral) resolution can be achieved. The interaction between an electron beam and the atoms of a sample generates multiple signals that can provide several information, both of structural and compositional nature. This section focuses on electron signals used to obtain structural information, while signals employed in spectroscopy techniques are reviewed in the *Characterization of bone composition* section (see page 25). Despite focused ion beam-scanning electron microscopy (FIB-SEM) also involves the use of an ion beam, as explained below, this technique is included in this section as imaging is accomplished by the electron probe.

Scanning electron microscopy

SEM is based on the rastering of a finely focused electron beam across the surface of a sample placed in a high-vacuum chamber ($<10^{-3}$-10^{-4} Pa) (Figure 3A). Some instruments can also be operated in higher pressure regimes (1-2000 Pa), for example by supplying water vapour. This type of SEM is known as low-vacuum or variable pressure SEM, or sometimes environmental SEM in the high pressure range, and it is especially useful to image insulating samples without any conductive coatings, otherwise necessary to reduce charging[152].

The interaction of the incident electron beam with the sample generates several signals (Figure 3B). Two of these signals, secondary electrons (SEs) and backscattered electrons (BSEs), are used to form SEM images. SEs are inelastically scattered electrons,

corresponding to weakly bound electrons in the outer atomic shell that are ejected due to the energy transferred by the incident beam (i.e., the primary beam, hence the term "secondary" electron). BSEs are elastically scattered electrons, corresponding to the electrons in the incident beam that are deflected "back" out of the sample due to the interaction with the atomic electric fields. If BSEs have high enough energy to eject weakly bound outer shell electrons, they can also generate SEs when interacting with the atoms of the sample. SEs have low energy, hence only those produced close to the sample surface (few nanometers) can escape and reach the detector. On the other hand, BSEs come from deeper within the sample, up to hundreds-to-thousands of nanometers below the surface[152].

The collection of SEs or BSEs by appropriate detectors produces an image of the sample surface. As the SEs that escape from the sample are those generated up to few nanometers below its surface, the contrast, i.e., the difference in intensity between two adjacent areas[153], in SE-SEM images provides information on the surface morphology and topography. By optimizing the acquisition conditions, 3D-like images with high depth of focus can be obtained. The number of BSEs produced (BSE coefficient) increases with the atomic number (Z), thus contrast in BSE-SEM images reflects variations in composition, with heavier elements appearing brighter, and, conversely, lighter elements appearing darker. This type of contrast is referred to as "Z-contrast" or "compositional contrast"[152].

SEM is widely used to characterize bone structure, especially in BSE mode as this allows for the easy identification of regions with dissimilar composition, for example, bone *vs.* embedding resin or bone *vs.* implant (Figure 3C). Other features like osteons and lamellae, as well as osteocyte lacunae within the bone matrix, can also be imaged[154]. Thanks to Z-contrast, areas with heterogenous levels of mineralization can be readily visualized. Specifically, if the grey-levels of BSE-SEM images are calibrated using a standard of known Z, it is possible to convert grey-levels into mineral content, expressing it as calcium content (wt% Ca). This technique, termed "quantitative backscattered electron imaging" (qBEI), can be used to map the BMD distribution. Standards for qBEI are typically made of carbon (Z = 6) and aluminum (Z = 13) and their average grey-levels are set to 25 and 225, respectively, during image acquisition to ensure a linear correlation between grey-level and calcium content in the compositional range relevant to bone[155].

SE-SEM images of bone are mostly useful when surface topography provides valuable information, for example in the case of fracture surfaces or when selected tissue components are removed, such as to examine marquise-shaped mineral aggregates post-deproteinization[156]. SE-SEM imaging can also be used to visualize the LCN after resin cast etching (Figure 3D), a treatment that removes both the inorganic and organic components of bone matrix, while preserving the resin-infiltrated LCN[157].

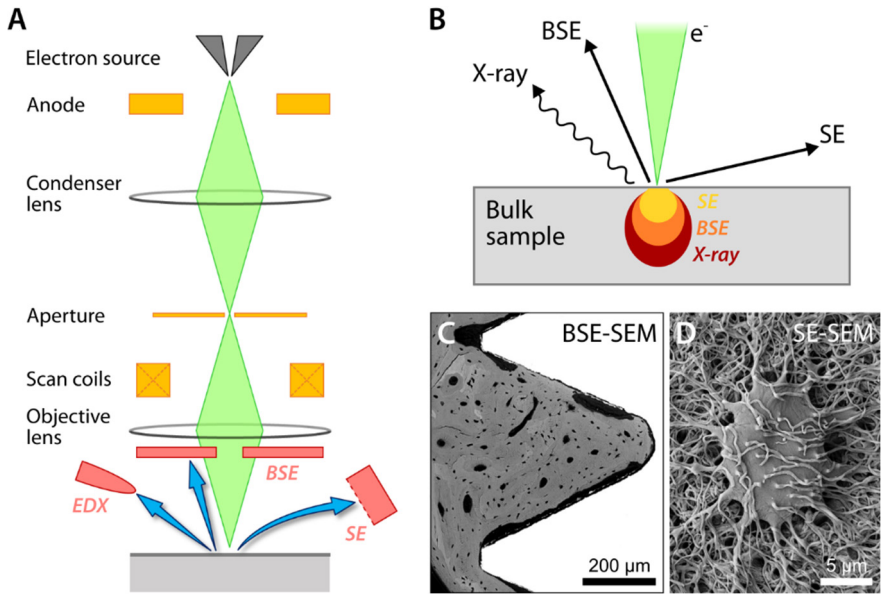

Figure 3. *Schematic representation of an SEM instrument (A) and signals generated of interest to this thesis with relative interaction volumes (B). The use of X-rays is discussed in the "Characterization of bone composition" section on page 25. Examples of SEM images in bone research: BSE-SEM image of a bone-implant interface (C) and SE-SEM image of an osteocyte lacuna after resin cast etching (D). [A is adapted with permission from reference [154], courtesy of Dr. Shah. C and D are reproduced with permission from references 158 and 157, respectively].*

Focused ion beam-scanning electron microscopy tomography

Although SEM is a powerful tool in bone research, SEM images are 2D and provide information on the sample surface only. On the other hand, by collecting a stack of 2D SEM images at successive intervals, it is possible to generate a 3D dataset. This is the working principle of FIB-SEM tomography, sometimes also referred to as "serial surface view", "serial slice-and-view", or "serial sectioning"[159]. This technique requires instruments equipped with two beams, i.e., an electron beam for imaging and an ion beam for milling. After milling with the ion beam a thin slice of material, typically in the 10 nm-range, the exposed cross-section is imaged with the electron beam, and the SE/BSE signal is collected. This sequence of milling and imaging is repeated in alternating steps until a stack of 2D SEM images is obtained. This stack is then assembled to generate a 3D image of the area examined, i.e., where the sequence milling-imaging took place[159]. Conventional dual-beam instruments are equipped with a Ga^+ ion column, but other ions can also be used offering different advantages and limitations. For example, instruments with a Xe^+ ion column, like that used in this thesis [Paper III], also called plasma FIB (PFIB), allows for higher removal rates, yielding volumes hundreds of micrometers in size, as opposed to tens of micrometers for Ga^+ FIB[160].

In bone research, FIB-SEM has been widely used to analyze the hierarchical organization of lamellar bone in relation to the arrangement of collagen fibril bundles[161,162]. Other applications relevant to this thesis include the examination of mineral ellipsoids at the mesoscale, accomplished using both PFIB-SEM[31] and conventional Ga^+ FIB-SEM instruments[22]. FIB-SEM has also been used to probe nanochannels, i.e., a network of nanopores thought to transport ions and small molecules within bone[163,164]. In the study of bone-implant interfaces, FIB-SEM tomography was first applied in 2005 to visualize bone growing into the pores of a dental implant[165]. FIB-SEM can be especially valuable to evaluate osseointegration in 3D to bridge the length scales probed by micro-CT and electron tomography[55].

Dual-beam instruments can be used not just for 3D tomography, but also for site-specific and minimally destructive preparation of electron transparent samples of bone and bone-biomaterial interfaces for transmission electron microscopy (TEM)[166]. As this is not a characterization-intended application, but a method for advanced sample preparation, it is more fitting to describe its working principle and use in this thesis in the *Materials and methods* chapter (see page 32).

Scanning/transmission electron microscopy

In TEM, an ultrathin sample (<100-200 nm) is illuminated by a (nearly) parallel electron beam, and, conversely from SEM, the signal used to form images is that transmitted through the sample. Various signals are generated from the electron beam-sample interaction, which are both back-scattered or forward-scattered, i.e., transmitted (Figure 4A). A dominant imaging mode in TEM is bright-field (BF), where images are formed by the direct electron beam that is transmitted, undeviated, through the sample. In BF-TEM images, the contrast originates from mass/thickness variations and diffraction. If only certain scattered electrons are selected, then a dark-field TEM image is obtained. Selection of a set of elastically scattered electrons to form dark-field TEM images can be done by placing an aperture (the objective aperture) over specific diffraction spots, instead of over the direct beam like in BF-TEM. The diffraction spots are visible when operating the TEM in diffraction mode, i.e., when imaging the back focal plane of the objective lens (reciprocal space). These diffraction patterns provide information on the crystal structure of the sample. Typically, electron diffraction is performed by illuminating a specific area in the sample using an aperture to collect diffraction information only from that region, hence the term "selected area electron diffraction" (SAED)[153].

Instead of a parallel beam like in traditional TEM, it is also possible to form a convergent electron probe. The convergent beam is rastered across the sample, and scattered electrons are collected at each point (pixel) on the sample. Due to the scanning nature of the probe, this imaging mode is called scanning TEM (STEM). Electrons used for STEM images are typically those incoherently scattered at high angles (Rutherford scattering), which are collected using high-angle annular dark-field (HAADF) detectors (Figure 4B).

HAADF-STEM images are formed by Z-contrast, and the scattering intensity is roughly proportional to Z^2 [167].

As electrons have smaller wavelength at higher energies, resolution achievable in S/TEM, with typical accelerating voltages ranging from 80 to 300 kV, is higher than in SEM. This makes S/TEM a powerful tool to image bone and bone interfaces with (sub)nanoscale resolution. BF-TEM has been extensively used to study the ultrastructure of bone, i.e., its nanoscale organization, for example to visualize the characteristic banding pattern of collagen fibrils and the spatial relationship between collagen fibrils and mineral, as well as the orientation of the mineral when combined with electron diffraction[145]. Since the pioneering work of Robinson, TEM has also been employed to study the shape and size of bone mineral[26]. Especially relevant to this thesis [Paper VI] was the use of BF-TEM and HAADF-STEM to reveal distinct organizational motifs in bone sections based on the orientation of the collagen fibrils with respect to the image plane, i.e., parallel *vs.* perpendicular[23,168–170], as shown in Figure 4C-E. In the context of bone implants, TEM imaging, often completed in HAADF-STEM mode, clearly demonstrated that osseointegration with several biomaterials, such as titanium[58,65,171] and hydroxyapatite[172], occurs at the nanoscale, redefining it as "nano-osseointegration".

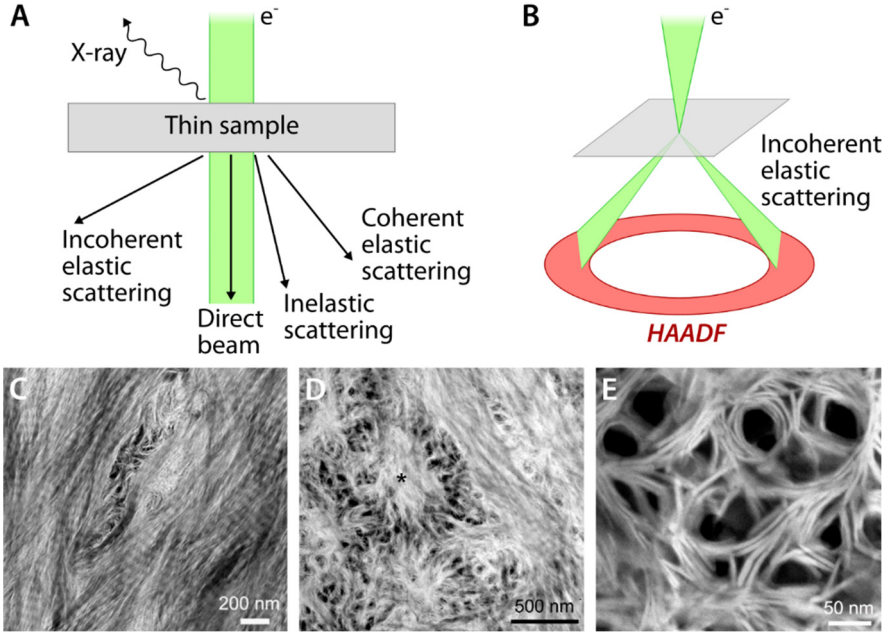

Figure 4. *Schematic representation of the signals generated in S/TEM of interest to this thesis (A), with a focus on HAADF-STEM (B). Characteristic HAADF-STEM images of sections of human femoral cortical bone oriented parallel (C) and perpendicular (D-E) to the long axis of the femur [reproduced with permission from reference 170].*

Electron tomography

While S/TEM images can provide structure-related information with nanoscale resolution, they suffer from the significant drawback of being 2D projection images of a 3D sample. In other words, all features along the sample thickness are projected onto the same plane, hence understanding their arrangement in 3D is not possible and can lead to misinterpretations of the spatial relationship between different components, for example, collagen fibrils and mineral in bone. Such a limitation can be overcome by electron tomography, which is based on the acquisition of S/TEM images at successive tilt angles, typically every 1-2°. This series of images, commonly referred to as "tilt series" in the field, is then aligned, e.g., by cross-correlation, and reconstructed into a 3D representation of the original object thanks to mathematical algorithms, such as simultaneous iterative reconstruction technique (SIRT)[173,174].

The quality of the 3D reconstruction is highly influenced by the number of projections, i.e., images acquired at different tilt angles. However, in conventional (single-tilt) electron tomography, shadowing of the sample holder and reduced size of the instrument chamber limit the tilt range typically to ±70°, producing an unsampled region, called "the missing wedge" due to its shape, where no projections can be acquired[173,174]. Specialized holders allowing for ±90° tilt or even full 360° rotation exist to overcome this limitation when used in conjunction with rod-shaped samples. This technique is called "on-axis electron tomography" and eliminates missing wedge artifacts in the final reconstruction, leading to improved quality and fidelity[175] (Figure 5).

Electron tomography can be carried out in both TEM and STEM mode. An essential requirement is that the image intensity at every tilt angle is a monotonic function of a certain property in the sampled volume, as stated in the "projection theorem". It follows that BF-TEM tomography cannot be used for crystalline samples, as diffraction contrast violates this theorem. On the other hand, samples containing crystalline phases, such as bone, can be successfully imaged using Z-contrast electron tomography, based on the acquisition of tilt series in HAADF-STEM mode[176].

In bone research, electron tomography has been a primary tool to probe collagen-mineral relationships in 3D and aid the formulation of the main ultrastructural models proposed to date[18,23,177]. Z-contrast electron tomography has also been applied to the study of osseointegration, demonstrating contact between bone and titanium at the nanoscale in 3D[178]. The use of Z-contrast tomography in osseointegration research has also encompassed on-axis electron tomography[179]. Moreover, by removing missing wedge artifacts, on-axis electron tomography presents several advantages for further elucidating bone ultrastructure at the nanoscale, especially collagen-mineral relationships, as demonstrated in this thesis in Paper VI.

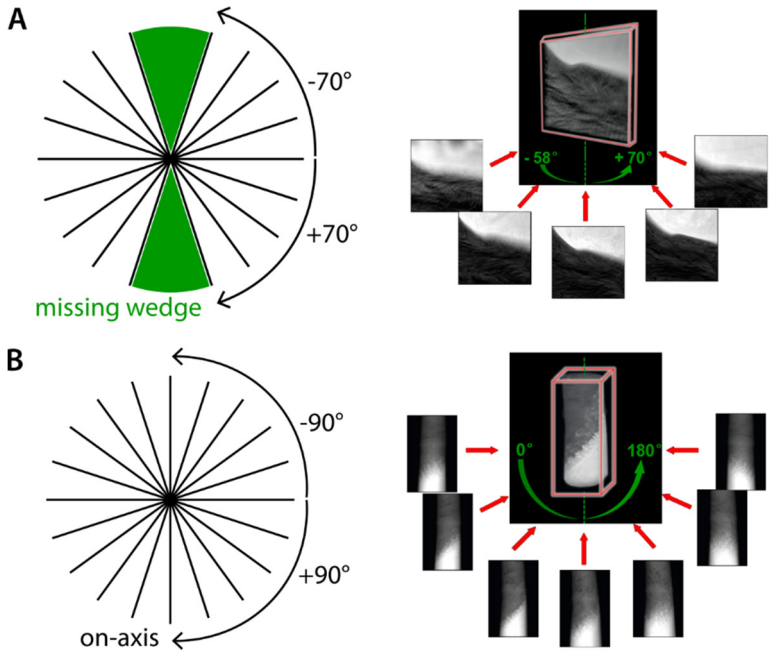

Figure 5. *Tilt range and examples of acquired projection images and final 3D reconstruction of a bone-implant interface in conventional (single-tilt) (A) and on-axis electron tomography (B). [Right images are adapted with permission from reference 179, courtesy of Dr. Wang].*

Characterization of bone composition

Despite BSE-SEM and HAADF-STEM images offering some insights into composition, they cannot determine which elements/compounds are present. Therefore, structural characterization should be complemented with spectroscopy techniques to determine compositional information in qualitative and/or quantitative terms. In this thesis, three spectroscopy techniques are employed, where the signals of interest are produced either using a light probe in the red range (micro-Raman spectroscopy) or an electron probe (energy-dispersive X-ray spectroscopy, EDX; and electron energy loss spectroscopy, EELS).

Micro-Raman spectroscopy

Raman spectroscopy is based on the Raman effect, i.e., the inelastic scattering of photons by matter. When photons of a single quantum energy (e.g., from a laser source) interact with the atoms of a sample, some photons (~1 in 10^7) experience a shift in quantum energy with respect to the source due to the transfer of part of their energy to molecules in the sample that become excited in vibrational states. The shift in energy, i.e., the Raman shift (expressed as frequency/wavenumber in cm^{-1}) can be used to identify the molecular compounds in the sample, as the vibrational states are characteristic of each molecule.

After the laser source has interacted with the sample, backscattered photons are collected by a spectrometer where a diffraction grating "splits" them in different components based on their energy. The signal intensity of each component is then recorded by a detector[180].

A schematic representation of the standard set-up of an instrument for Raman spectroscopy is given in Figure 6A. When a Raman spectrometer is integrated with an optical microscope, e.g., a confocal system, the technique is more precisely labelled as "micro-Raman spectroscopy". Raman spectra can be acquired in specific points of interest on the sample surface, but hyperspectral mapping can also be accomplished. This is done by recording a Raman spectrum at constant steps (pixels) over an area of interest, and then using a specific spectral parameter (e.g., peak intensity) to map its distribution and variation in the examined region. With transparent samples, hyperspectral mapping can be extended in the third dimension, i.e., the sample depth, to produce 3D maps[180].

Micro-Raman spectroscopy can provide information regarding bone quality, both in native and peri-implant bone. The typical Raman spectrum of bone is shown in Figure 6B. Bone matrix composition is often expressed in terms of mineral-to-matrix ratio to evaluate the degree of mineralization[181]. This ratio is obtained from integral areas of bands characteristic of the mineral phase, i.e., the phosphate peaks, and of the organic phase, e.g., the amide peaks, which are mostly representative of collagen[182]. Another compositional metric is the carbonate-to-phosphate ratio, from which the extent of carbonate substitution, typically increasing with age, can be inferred[181]. Lastly, structure-related information can also be obtained, as the full width at half maximum of the phosphate band at ~959 cm^{-1} is related to the mineral crystallinity, with higher crystallinity yielding sharper peaks[181].

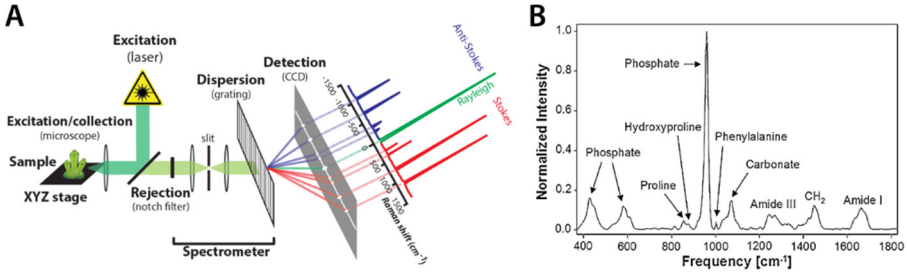

Figure 6. *Schematic representation of the typical configuration of a Raman spectrometer (A) and typical Raman spectrum of bone (B). [A and B are reproduced with permission from references 180 and 181, respectively].*

Energy-dispersive X-ray spectroscopy

The interaction of an electron beam with the atoms of a sample generates not only electron signals, but also X-rays. When the incident electron beam has a high enough energy, above the critical ionization energy, it can cause a core electron, i.e., an electron from an inner shell, to be ejected from the atom, leaving behind a vacancy. This hole can be filled by an electron from a higher energy shell. When this occurs, the excess energy is emitted as a photon, more precisely, an X-ray. These X-rays are called "characteristic" because their energy is unique to each element in the periodic table. This phenomenon is at the basis of EDX, where characteristic X-rays are detected to determine the elemental composition of the sample, also allowing for (semi)quantitative analysis[152]. EDX analyses can be completed in both SEM and TEM instruments if equipped with X-ray detectors. In TEM, EDX is carried out in STEM mode to acquire EDX spectra in specific points, across a line, or also over an entire region of the sample (spectral imaging)[153].

SEM-EDX can be used in bone research to examine bone matrix mineralization, for example in terms of the calcium-to-phosphorus ratio, or to evaluate trends in elemental variation across interfaces[154]. This can be especially applicable to the study of bone-biomaterial interfaces. STEM-EDX can have similar applications, but offers a greater spatial resolution than SEM-EDX as the interaction volume is reduced compared to bulk SEM samples[153]. Some examples include the quantification of intra- and extra-fibrillar mineralization in native bone[169], or the determination of chemical gradients within the interface between bone and metallic or ceramic implants[171,172,183]. Notably, this thesis includes a novel application of STEM-EDX in bone research, i.e., in tomography mode [Paper VI].

Electron energy loss spectroscopy

In S/TEM, some of the incident electrons lose part of their energy due to inelastic scattering and are slightly deviated from their trajectory as they traverse the sample. These electrons, together with the unscattered ones (direct beam), can be collected by a spectrometer to generate a plot of the signal intensity (electron count) as a function of the energy loss. This type of spectroscopy, called EELS, can provide different information based on the region of the EELS spectrum considered, i.e., the zero-loss, corresponding to the unscattered beam, low-loss, or high-loss region. The high-loss spectrum, also termed "core-loss", which is employed in this thesis, corresponds to electrons scattered inelastically due to the interaction with tightly bound core electrons of the atoms of the sample. Hence, the energy loss in this region represents ionization edges that can be used for elemental fingerprinting. EELS is mostly coupled with STEM to acquire spectral images, where each pixel in the image corresponds to an EELS spectrum. EELS offers higher energy and spatial resolution than EDX, but it has strict requirements in terms of sample thickness as the signal collected is that transmitted through the sample[153,184].

The high spatial resolution of EELS has been employed to probe the chemical composition of nanoscale features in bone, specifically of low Z-contrast circular spaces

that are interpreted as cross-sectional views of collagen fibrils by some authors, who corroborated their hypothesis using EELS mapping of carbon and nitrogen as markers for collagen[185,186]. In the study of bone-implant interfaces, a notable application of EELS involved the acquisition of EELS data in tomography mode, i.e., collecting a spectral image together with a HAADF-STEM image at each tilt angle in the tomography experiment[187]. This made it possible to reconstruct the bone-implant interface in four dimensions (4D), i.e., combining 3D structural and compositional information, with nanoscale resolution.

Aim

The overarching goal of this thesis is to apply multimodal and multiscale characterization approaches typical of materials science to understand abnormalities in the structure, composition, and repair of compromised bone, and to advance nanoscale analyses to elucidate bone ultrastructure.

The specific aims are:

1. To determine the structure and composition of bones formed by endochondral (femur) and intramembranous (calvarium in the parietal region) ossification in the Lund MetS rat, a novel animal model for LepR deficiency, obesity, and hyperglycemia (T2DM-like) [Paper I].

2. To resolve the interface between bone and bacteria from the micro- to the nanoscale in MRONJ to inform perspectives on the eventual role played by bacteria in the necrosis of the jaw [Paper II].

3. To examine the bone-implant interface and the LCN in peri-implant bone for a novel AM implant with engineered porosity and genistein functionalization for local drug delivery, in particular bridging micro- and nanoscale considerations via development of mesoscale analyses [Paper III].

4. To evaluate the effect of the local delivery of PTH 1-34, administered via surface-functionalized bioactive glass, on bone repair and osseointegration in ORX rats [Paper IV].

5. To demonstrate a micro-to-nanoscale characterization workflow for bone-bioactive glass interfaces, including 3D high-resolution imaging with electron tomography to resolve and understand the interface and the ultrastructure of bone in its proximity [Paper V].

6. To shed light on bone ultrastructure, specifically the low-contrast spaces characteristic of the lacy pattern and the morphology and organization of the extra-fibrillar mineral, using correlative on-axis Z-contrast electron tomography and EDX tomography [Paper VI].

Materials and methods

BONE MODELS AND BIOMATERIALS

Samples from human [Papers II, VI] and rat bone [Papers I, III-V] were examined in both healthy, i.e., without any known bone disease [Papers V-VI, plus control groups in Papers I-II, IV], and compromised conditions [Papers I-IV]. Different preclinical rat models were used, as described in the following section [Papers I, III-V]. This thesis includes samples from both male and female humans/rats, but both sexes were not evaluated in a same study. Bone samples were collected either from native tissue [Papers I-II, VI] or from the peri-implant compartment [Papers III-V].

Table 1 summarizes the main information on bone samples in terms of species, anatomical location, and sex, as well as eventual compromised conditions and biomaterials present. The use of human tissues and the animal studies were approved by the following committees:

- Animal Research Ethics Committee of Gothenburg, Sweden (Dnr. 14790/2019) [Paper I].
- Regional Ethical Review Board of Gothenburg, Sweden (Dnr. 424-08) [Paper II].
- Ethics Committee on the Use of Animals (CEUA) at UNESP, Brazil (approval no. 00733-2020) [Paper III].
- Ethics Committee on the Use of Animals (CEUA) at UNESP, Brazil (approval no. 00199-2017) [Papers IV-V].
- Hamilton Integrated Research Ethics Board (HIREB) at McMaster University, ON, Canada (approval no. 12-085-T) [Paper VI].

Experimental animal models

LepR-deficient model

In Paper I, 20-week-old Lund MetS male rats were studied. Due to a LepR genetic mutation, these rats are a monogenic model of obesity with potential applications in T2DM research[110,188]. While $LepR^{+/+}$ rats are lean and euglycemic, $LepR^{-/-}$ rats display severe obesity and hyperglycemia. Both $LepR^{+/+}$ and $LepR^{-/-}$ animals were considered by analyzing structure and composition of their femurs and calvaria in the parietal region.

Osteoporotic models

In Paper III, 3-month-old OVX Wistar female rats were used. At 30 days after OVX surgery, the animals received Ti-6Al-4V implants in their tibia and were sacrificed 28 days after implant installation.

In Paper IV, 6-month-old ORX Wistar male rats were used. Non-ORX rats, subjected to sham surgery, were also included as healthy controls. At 30 days after ORX/sham surgery, a defect was created in the tibia of the animals and filled with bioactive glass (Biogran®), without and with PTH 1-34 functionalization, prior to installation of a cp-Ti implant. Animals were sacrificed at 30 days after implant installation for electron microscopy experiments, and 60 days after implant installation for all the other analyses. One of the rats from the control group in Paper IV was used for the experiments completed in Paper V.

Clinical samples

In Paper II, necrotic and non-necrotic bone samples were retrieved from the upper and lower jaws of a 73-year-old female individual diagnosed with osteoporosis and MRONJ. The sampling procedure occurred 1.5 years after the interruption of a 23-year-long oral therapy with bisphosphonates (alendronate tablets).

In Paper VI, cortical bone prepared from the femur of a 68-year-old male individual without any known bone diseases was examined.

Biomaterials

In Paper III, a Ti-6Al-4V implant with a porous mid-section (45% porosity, 500 μm pore size) was manufactured by laser powder bed fusion (L-PBF). The implant surface was acid-etched with sulfuric acid (H_2SO_4) and functionalized with genistein by an electrochemical layer-by-layer method [patent application BR 10 2021 019134 1, Instituto Nacional da Propriedade Industrial, Brazil].

In Papers IV-V, particles of Biogran®, a commercially available bioactive glass, were used to fill a surgical defect in the rat tibia prior to the installation of a cp-Ti (grade IV) implant. In Paper IV, some animals received Biogran® previously functionalized with PTH 1-34 by sonochemistry following the protocol described by Gomes-Ferreira et al.[189].

Table 1. *Information on the bone samples used in this thesis in terms of species, anatomical locations, and sex. Implanted biomaterials and the type of compromised condition present are also reported when applicable (otherwise stated as not applicable, N/A).*

Paper	Species	Anatomical location	Sex	Biomaterial(s)	Compromised condition
I	Rat (Lund MetS)	Femur Calvarium	Male	N/A	LepR deficiency, obesity, hyperglycemia
II	Human	Maxilla Mandible	Female	N/A	Osteoporosis MRONJ
III	Rat (Wistar)	Tibia	Female	Ti-6Al-4V implant (porous, acid-etched, genistein-coated)	OVX
IV	Rat (Wistar)	Tibia	Male	Bioactive glass (without and with PTH 1-34) Cp-Ti implant	ORX
V	Rat (Wistar)	Tibia	Male	Bioactive glass Cp-Ti implant [not studied]	N/A
VI	Human	Femur	Male	N/A	N/A

SAMPLE PREPARATION

Retrieval, preservation, and preparation of *bulk* samples

In Paper I, femurs and calvaria were retrieved at 20 weeks of age, fixed, and dehydrated. Femurs were cut transversally to separate proximal and distal sections, which were then cut longitudinally. Longitudinal femur sections and calvaria were resin-embedded in LR White and polished. After embedding, the calvaria were cut along the coronal plane to have a cross-sectional view of the parietal region and the sagittal suture.

In Paper II, samples were retrieved from the upper (left side: non-necrotic; right side: necrotic) and lower (right side: necrotic) jaws of a human subject. Samples were fixed, dehydrated, resin-embedded in LR White, and processed for a central histological ground-section stained with toluidine blue. Leftover blocks were polished.

In Papers III-V, implants and peri-implant tissues were retrieved *en bloc*, fixed, dehydrated, and resin-embedded in polymethyl methacrylate [Paper III] or Technovit [Papers IV-V]. Embedded blocks were sectioned longitudinally along the implant and polished. Sections for immunohistochemistry in Paper IV did not follow this preparation route, but were instead demineralized in 10% EDTA (ethylenediaminetetraacetic acid) after fixation, dehydrated, diaphanized in xylol, embedded in paraffin, and cut to a thickness of 5 μm.

For samples in Papers I-V, fixation was done in 10% neutral buffered formalin, and dehydration took place in a graded ethanol series (steps differ in length and concentration in the Papers).

In Paper VI, a section of human femur was fixed in 4% glutaraldehyde in a 0.1 M cacodylate buffer for one week, cut transversally, dehydrated in a graded ethanol series, resin-embedded in Embed812, and polished.

Electron transparent samples for S/TEM

Electron transparent samples for S/TEM experiments were prepared by *in situ* lift-out in dual-beam FIB instruments equipped with a 30 kV Ga^+ ion column, a gas injection system to deposit a protective layer of carbon and/or tungsten over the region of interest (ROI), and a micromanipulator to lift-out and manoeuvre the sample. A schematic representation of a typical dual-beam instrument is provided in Figure 7A.

In Papers II-VI, electron transparent samples were prepared in the conventional form of wedge-shaped lamellae following existing protocols[190], as schematically shown in Figure 7B-C. In short, after depositing a layer of carbon and/or tungsten over the ROI, typically 12×2 μm^2, coarse trenches were milled around it at 30 kV and currents in the 6.5-65 nA

range (lower currents closer to the ROI). The sample was then lifted-out using the micromanipulator, attached to a copper grid for TEM holders, and thinned to electron transparency at 30 kV and progressively lower currents (from at most 0.79 nA down to 40 pA), with a final step at low voltage (5-10 kV) and current (60-80 pA) to limit Ga^+ implantation and amorphization damage.

In Paper VI, one sample was lifted-out in a *plan-view* fashion[191]. A large ROI, 15 × 15 μm², was coated with a tungsten deposit. Similarly to the lift-out protocol described above, after coarse milling around the ROI, the sample was lifted-out and attached to a copper grid for TEM holders, which had been previously mounted horizontally in a specialized stub (described by Huang et al.[192]). Thanks to its design with two orthogonal pins, the stub was removed from the holder and re-inserted after a 90° rotation so that the copper grid became oriented vertically. Thinning to electron transparency then proceeded normally.

In Paper VI, two rod-shaped samples were also prepared. The lift-out process was analogous to that for wedge-shaped samples, the main differences being the size of the ROI selected (3 × 3 μm²) and the use 1 mm cylindrical posts for TEM rotation holders, instead of conventional copper grids. Thinning to electron transparency was completed by annular milling at 30 kV and 40-150 pA (Figure 7D).

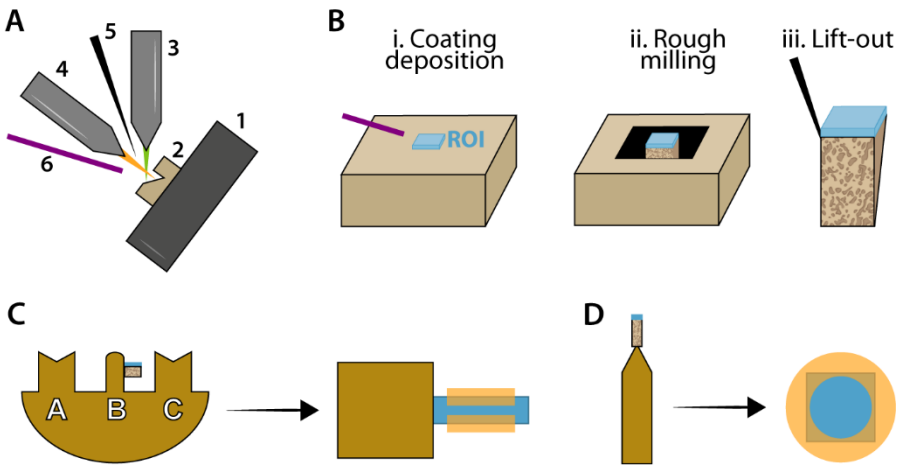

Figure 7. *Schematic representation of the main components of a dual-beam instrument (A): stage (1); sample (2); electron beam column (electron beam is shown in green) (3); ion beam column (ion beam is shown in orange) (4), typically oriented at 52-54° with respect to the electron beam column; micromanipulator (5); and gas injection system (6) [Note: detectors are not shown for simplicity]. Main steps of sample preparation for S/TEM experiments (B-D): after depositing a protective coating (light blue) over the ROI via the gas injection system (step i in B) and milling coarse trenches around it (step ii in B), the sample is lifted-out with the micromanipulator and attached to a copper grid for conventional wedge-shaped samples (C) or to a cylindrical post for rod-shaped samples (D). Thinning to electron transparency is performed by milling on both sides in C, or by annular milling in D.*

Resin cast etching

Resin cast etching was used in Papers II-III to expose resin-infiltrated elements below the surface such as the LCN, as well as bacteria in Paper II. In Paper II, samples were immersed in 9% phosphoric acid (H_3PO_4) for 30 s, while in Paper III a shorter immersion time (10 s) was employed, but in a more concentrated acid solution (37%). In both studies, after rinsing with deionized water, samples were immersed in 5% sodium hypochlorite (NaOCl) for 5 min, then rinsed again and let air-dry overnight. The steps in phosphoric acid and sodium hypochlorite remove the inorganic and organic components in bone, respectively[157].

X-RAY, ELECTRON, AND ION MICROSCOPY

Micro-CT

Micro-CT was completed in Papers I and IV, prior to resin embedding, to evaluated bone morphometry in 3D. In Paper I, micro-CT scans were acquired for femurs and calvaria to obtain 3D reconstructions of the overall bone geometry, as well as to gain microstructural information. Specifically, in the femurs, various morphometry metrics were quantified in cortical bone (cortical thickness, cortical bone area, total cross-sectional area inside the periosteal envelope, and cortical area fraction) and trabecular bone (bone volume fraction, trabecular thickness, trabecular separation, and trabecular number), together with TMD in both regions. In the calvaria, the analyses focused on the parietal region to measure its thickness and on the sagittal suture to evaluate its thickness and length. In Paper IV, micro-CT was used to assess various morphometry parameters in peri-implant bone (bone volume fraction, trabecular thickness, trabecular separation, and trabecular number), and to measure BIC in order to evaluate osseointegration.

SEM

Polished samples for SEM experiments were mounted on aluminum stubs using conductive tapes (silver/carbon) and/or paint (silver/nickel). In Papers II-VI, these samples were coated with either carbon or gold (~10-20 nm-thick) for imaging in high-vacuum conditions.

BSE-SEM

All the Papers in this thesis included the use of SEM imaging in BSE mode. In Papers III-VI, BSE-SEM images were acquired in high-vacuum conditions, while in Papers I-II the SEM instrument was operated in low-vacuum regime (water vapour pressure of 1 Torr). Accelerating voltage ranged from 5 to 20 kV.

In the Papers, BSE-SEM imaging mainly served the following aims:

- Examination of bone microstructure and differently mineralized areas [Papers I-II].
- Assessment of bone growth in the peri-implant space, e.g., to identify distance and contact osteogenesis and regions of bone-biomaterial contact [Papers III-V].
- Selection of ROIs for STEM sample preparation [Papers II-VI].
- Identification of ROIs for other analyses, i.e., SEM-EDX [Papers II, IV] and micro-Raman spectroscopy [Papers I-II].

qBEI

In Paper I, qBEI was completed to convert grey-levels in BSE-SEM images into mineral content (wt% Ca). The experimental set-up followed published protocols[155], using a standard made of carbon and aluminum and adjusting the brightness and contrast in the BSE-SEM images of the standard to have average grey-levels equal to 25 and 225 in the carbon and aluminum regions, respectively. The following metrics were evaluated: weighted mean calcium concentration; peak height of the distribution; peak position of the most frequent calcium concentration; full width at half maximum of the calcium peak; spread of the distribution on the low concentration side; and spread of the distribution on the high concentration side.

SE-SEM

In Papers II-III, SE-SEM images were acquired for bone samples after resin cast etching to visualize bone cells [Papers II-III] and bacteria [Paper II]. For the acquisition of SE-SEM images, microscopes were operated in high-vacuum conditions at 3-7 kV.

S/TEM imaging and electron diffraction

STEM

Except for Paper I, all the other Papers included the use of HAADF-STEM imaging. This was completed to resolve bone ultrastructure [Papers II-VI] and/or the interface between bone and biomaterials [Papers III-V] at the nanoscale. The S/TEM instruments were operated at 200-300 kV.

BF-TEM and SAED

In Paper II, a S/TEM instrument was operated at 200 kV in TEM mode to acquire BF images and complete SAED experiments in a region of necrotic bone interfacing with bacteria-invaded resin. The insertion of the aperture illuminated an area of the sample approximately 250 nm in width from which the diffraction pattern was collected.

STEM tomography

In Paper V, conventional (single-tilt) Z-contrast electron tomography using a wedge-shaped electron transparent sample was completed to reconstruct the interface between bone and bioactive glass in 3D, as well as the ultrastructure of bone at said interface. HAADF-STEM images were collected over a tilt range from -60° to +74° with 2° tilt steps. The S/TEM instrument was operated at 300 kV.

In Paper VI, on-axis Z-contrast electron tomography using rod-shaped samples was completed. A specialized holder for rotation tomography was used to extend the tilt range

compared to single-tilt electron tomography. Four tilt series were acquired in total: two over a ±90° tilt range, and two over a ±85° tilt range. The tilt step was equal to 2° in one tilt series, and 5° in the other three. In all tilt series, HAADF-STEM images were collected. In one tilt series, BF-STEM images were also acquired alongside HAADF-STEM images. In three tilt series, EDX maps were also collected at each tilt angle, as reported in more detail in the *EDX* section (see page 39). For all acquisitions, the instrument was operated at 200 kV. During the tilt series collection, focusing and image shifting were done automatically in the tomography acquisition software. Tilt series were aligned by cross-correlation and reconstructed using SIRT with 25 iterations.

PFIB-SEM tomography

In Paper III, 3D imaging of a volume of implant and peri-implant bone was accomplished by PFIB-SEM tomography using a dual-beam FIB instrument equipped with a Xe^+ ion column. Ion milling was carried out at 30 kV and 4 nA, with a slice thickness of 30 nm. Imaging with the electron beam was done in BSE mode at 1.2 kV. The stack of BSE-SEM images was aligned to generate a 3D volume, which was mainly used to investigate mineral ellipsoids and the LCN in peri-implant bone.

SPECTROSCOPY

Micro-Raman spectroscopy

Micro-Raman spectroscopy was applied in Papers I-II to gain information on bone quality, primarily in relation to bone matrix composition. Specifically, in Paper I, Raman spectra were collected at each pixel over a rectangular area, in fact obtaining hyperspectral maps. In Paper II, line scans across the bone-resin interface were acquired instead. Raman spectra were acquired with varying step size (1 μm in Papers I-II; 10 μm in Paper I), exposure time (1 s in Paper I; 3 s in Paper II), and accumulations (2 in Paper I; 5 in Paper II) using an instrument equipped with a 633 nm laser and 1800 g mm^{-1} grating. Spectra were baseline subtracted, cleaned of cosmic rays, and denoised. In Paper I, compositional measures, i.e., mineral-to-matrix ratio and carbonate-to-phosphate ratio, and crystallinity of bone mineral were evaluated in different ROIs in femurs and calvaria. In Paper II, only the mineral-to-matrix ratio was measured.

EDX

Both SEM-EDX [Papers II, IV] and STEM-EDX [Papers III, VI] were completed in some of the studies included in this thesis. In particular, EDX was done in tomography mode in Paper VI.

SEM-EDX

In Paper II, SEM-EDX was used to compare mineralization gradients at the bone-resin interface in necrotic and non-necrotic bone, specifically evaluating trends in calcium, phosphorus, and carbon in line scans acquired across the interface. EDX acquisition was carried out in an SEM instrument operated at 20 kV in low-vacuum conditions (water vapour pressure of 1 Torr). In Paper IV, SEM-EDX was used to evaluate compositional gradients within bioactive glass particles after ionic exchange and degradation taking place *in vivo*. This was done by mapping the amount of calcium, phosphorus, and silicon in bioactive glass particles, and extracting line profiles across them. For this analysis, a microscope operated at 10 kV in high-vacuum mode was used.

STEM-EDX

In Paper III, STEM-EDX was used to examine the compositional gradients across the bone-implant interface with nanoscale resolution, mapping the content in implant elements (titanium, aluminum, vanadium, oxygen) and bone elements (calcium, phosphorus). Maps were acquired with a pixel dwell time of 10 μs, integrating over 1000 frames. The microscope was operated at 200 kV, and the EDX signal was acquired using a Super-X detector, which is composed of four in-column silicon drift detectors.

STEM-EDX tomography

In Paper VI, STEM-EDX was coupled with tomography acquisition, i.e., EDX maps were acquired at each angle in the tilt series at the same time as HAADF-STEM images. Elemental maps were acquired for carbon and nitrogen as markers of type I collagen, and calcium and phosphorus as markers of bone mineral. Maps were acquired with a pixel dwell time of 50 μs, integrating over 10 frames. The tilt series of EDX maps of each element were aligned and reconstructed by SIRT (25 iterations) based on the HAADF signal. Similarly to Paper III, EDX signal acquisition was carried out in a S/TEM instrument equipped with a Super X-detector and operated at 200 kV.

EELS

In Paper II, EELS was completed at the bone front interfacing with the bacteria-invaded resin space to assess mineralization gradients at the nanoscale. EELS spectral images were acquired at 300 kV, with 0.5 eV/channel energy dispersion, 5 nm pixel size, and 0.05 s exposure time per pixel. After background subtraction, elemental maps for calcium, phosphorus, and carbon were obtained from the EELS spectra by extracting the signal in the energy loss window characteristic of each element.

OTHER ANALYTICAL TECHNIQUES

This section briefly summarizes methodological details for the complementary analytical techniques used in this thesis, beyond the main characterization tools previously reviewed.

Reference point indentation

In Paper I, reference point indentation (RPI) measurements were completed on the periosteal surface of the proximal femurs using a microindenter to evaluate the following parameters: 1st cycle indentation distance; 1st cycle unloading slope; 1st cycle creep indentation distance; total indentation distance; indentation distance increase; average creep indentation distance; average energy dissipated; and average unloading slope. These measures are related to the resistance to indentation, hence they provide information on bone mechanical properties.

Static/dynamic histology and immunohistochemistry

In Paper II, histology was used to assess the presence of necrosis and bacterial infection, as well as other relevant cells (e.g., multinucleated cells). Ground sections stained with toluidine blue were imaged in a light microscope with ×4, ×10, ×20, and ×40 objectives.

In Paper IV, dynamic histology was carried out by injection of fluorochromes during the animal study (calcein and alizarin red at 14 and 42 days after implant installation, respectively). Sections obtained from longitudinal cuts in correspondence of the third-to-fifth implant thread were imaged by confocal laser microscopy with a ×10 objective to measure fluorochrome area, daily bone mineral apposition rate, and neoformed bone area.

In Paper IV, immunohistochemistry using TRAP (tartrate-resistant acid phosphatase) staining was performed to assess osteoclast activity. Immunolabelling was classified based on the percentage of positive immunolabels within the ROI as mild (25%), moderate (50%), or intense (75%).

Removal torque

In Paper IV, removal torque measurements were performed to quantify implant anchorage from a biomechanical perspective. Removal torque was applied counter-clockwise with increasing values until disruption of the bone-implant interface occurred. The maximum reverse torque value registered in this process was the one considered for inter-group statistical comparison.

Gene expression

In Paper IV, after the disruption of the bone-implant interface during removal torque measurements, bone tissue in the peri-implant compartment was collected, flash-frozen, and stored at -80 °C until further processing. Total RNA was extracted using a spin-column method, quantified with spectrophotometry, and cDNA synthesized. qPCR (quantitative polymerase chain reaction) was performed to quantify the relative gene expression of alkaline phosphatase and osteocalcin.

IMAGE ANALYSIS

Images were analyzed not just in qualitative terms, but segmentation of features of interest was also performed for quantification purposes or to identify specific ROIs for subsequent analyses.

In Paper I, micro-CT data were analyzed using the ORS Dragonfly software. Femurs were evaluated with the "Bone Analysis" plug-in, where trabecular and cortical bone were segmented using the Buie algorithm[193] to assess morphometry parameters in each compartment. In the parietal region, bones and sagittal suture were segmented to then evaluate their thickness using the "Volume thickness map" operation. Slice analysis in 2D was performed to evaluate sagittal suture length. Hyperspectral Raman maps were segmented by a clustering algorithm (K-means) using the "sklearn.cluster" library in Python 3.8.10 to separate different ROIs (mineralized cartilage islands in the femurs and highly mineralized bone in the calvaria). Different Raman measures were then evaluated in each region separately.

In Paper II, nanosized particles in HAADF-STEM images were segmented using Fiji[194] to evaluate their average dimensions. Intensity profiles were also extracted from HAADF-STEM images to measure the periodicity of the banding pattern characteristic of collagen fibrils.

In Paper VI, electron tomograms were visualized and analyzed using the ORS Dragonfly software. Data were segmented mostly based on grey-level thresholding to label both dark nanosized spaces within bone and the mineral phase to evaluate feature size and connectivity. EDX tomograms were also segmented to quantify the content of different elements within the segmented nanosized spaces. Manual segmentation followed by slice analysis in 2D was completed to measure the dimensions of the mineral plates.

Segmentation was also carried out for visualization purposes, such as in Paper III where the LCN was segmented to better examine its organization within peri-implant bone. In Paper V, qualitative segmentation was completed by adjusting colour-levels and opacity in the 3D volume rendering to assess collagen fibrils orientation at the interface with bioactive glass. The ORS Dragonfly and Avizo software programs were used in Papers III and V, respectively.

STATISTICAL ANALYSIS

In Papers I-II, two groups were compared, hence statistical significance was evaluated with the Student's *t*-test or Welch's *t*-test, or, alternatively, the non-parametric Mann-Whitney U test with small sample size and/or violation of normality distribution. Specifically, statistical significance of micro-CT data in Paper I was assessed with the Student's *t*-test (in the case of equal variance) or the Welch's *t*-test (in the case of unequal variance or sample size) after verifying normality and homoscedasticity with the Shapiro-Wilk test and the Brown-Forsythe test, respectively. Micro-Raman spectroscopy results were compared with the Mann-Whitney U test in Papers I-II. This test was also used to evaluate statistical significance in qBEI and RPI data in Paper I, and SEM-EDX data in Paper II.

In Paper IV, six different groups were compared, hence statistical significance was evaluated using a one-way ANOVA (analysis of variance) with a Tukey's post-hoc test for data obtained from micro-CT, removal torque, gene expression, and dynamic histology (mineral apposition rate and neoformed bone area). Fluorochrome area in dynamic histology was compared using a two-way ANOVA.

For all statistical tests, significance level was set at $\alpha = 0.05$. In Papers I-II, statistical analysis was completed in Python 3.8.10 using the "scipy.stats" library, while GraphPad Prism 8.1.1 was used in Paper IV. In all the Papers, data are reported as mean ± standard deviation.

Results

PAPER I

In this work, the structure and composition of bone in a novel preclinical model for LepR deficiency, hyperglycemia, and obesity, the Lund MetS rat, was characterized, focusing on bone material properties of femurs and calvaria at the microscale. A graphical summary of the main findings is found below in Figure 8.

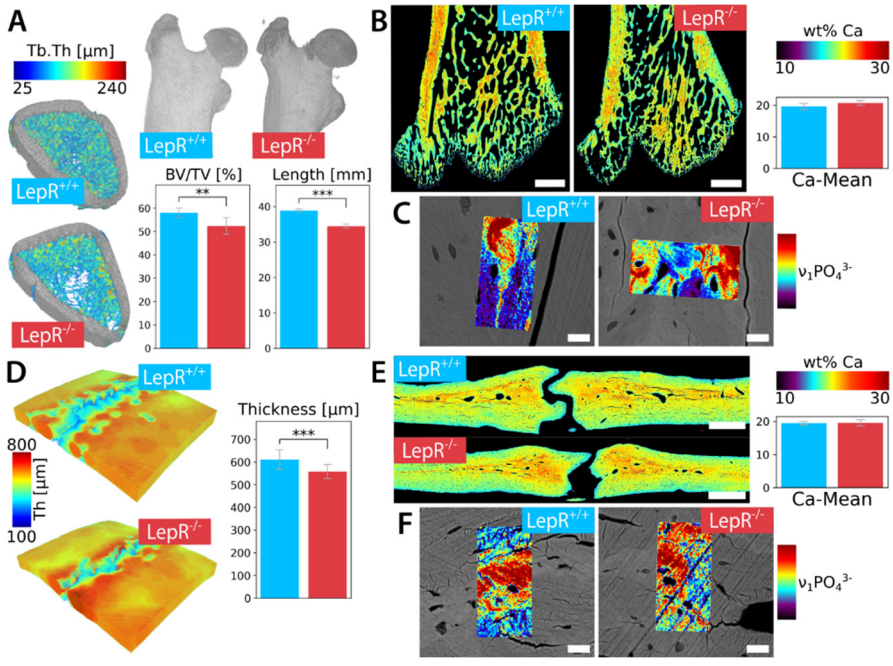

Figure 8. *Micro-CT reconstructions of the trabecular compartment in the distal femurs, coloured based on trabecular thickness (Tb.Th) and of proximal femurs (right), together with bar plots of bone volume fraction (BV/TV) and femur length (A). qBEI images of the femurs where pixel intensity corresponds to mineral concentration (wt% Ca), with relative bar plots of mean calcium concentration (Ca-Mean) (B). BSE-SEM images of areas with mineralized cartilage islands with superimposed Raman maps of the* $\nu_1PO_4^{3-}$ *peak intensity (C). Micro-CT reconstructions of parietal bones in the calvarium coloured based on bone thickness (Th), with relative bar plot (D). qBEI images of calvaria in the parietal region, where pixel intensity corresponds to mineral concentration (wt% Ca), with relative bar plots of Ca-Mean (E). BSE-SEM images of areas with highly mineralized bone with superimposed Raman maps of the* $\nu_1PO_4^{3-}$ *peak intensity (F). Healthy (LepR*$^{+/+}$*) and LepR-deficient (LepR*$^{-/-}$*) animals are colour-coded in blue and red, respectively. Scale bars are 1 mm in B, 20 µm in C and F, and 500 µm in E. ** and *** denote statistical significance (*$p < 0.01$ *and* $p < 0.001$*, respectively). [Adapted with permission from Paper I].*

Results summary: Paper I

LepR-deficient animals ($LepR^{-/-}$) displayed severe obesity and hyperglycemia compared to the healthy control group ($LepR^{+/+}$), as indicated by their statistically significant higher weight and blood glucose levels, respectively ($p < 0.001$).

From the 3D micro-CT reconstruction of the proximal femurs, it was apparent that the femoral head and neck were incompletely developed in the $LepR^{-/-}$ animals. Caliper measurements of the entire femur showed that the bone was significantly shorter in the $LepR^{-/-}$ animals ($p < 0.001$). Morphometry analysis in the distal portion of the femurs revealed that the microstructure was altered in both cortical and trabecular regions of the $LepR^{-/-}$ rodents. Specifically, $LepR^{-/-}$ animals had thinner trabeculae ($p > 0.05$) and cortices ($p < 0.001$) than their healthy counterparts. The trabecular compartment was overall more porous in the $LepR^{-/-}$ group ($p < 0.01$), with fewer trabeculae ($p < 0.05$) and an increased trabecular separation ($p < 0.01$). Cortical bone area and area fraction were also smaller in the $LepR^{-/-}$ animals ($p < 0.001$ and $p < 0.01$, respectively). Calvaria also displayed altered morphology in the $LepR^{-/-}$ rats, which had thinner parietal bones ($p < 0.001$), while the sagittal suture was found to have a reduced length ($p < 0.01$) and width ($p < 0.001$).

On the other hand, no differences in bone matrix composition between $LepR^{-/-}$ and $LepR^{+/+}$ animals were detected in neither femur nor calvarium in the parietal region ($p > 0.05$). This similarity was consistently found regardless of the compositional metrics considered, i.e., TMD in micro-CT, BMD distribution in qBEI, and mineral-to-matrix and carbonate-to-phosphate ratios in micro-Raman spectroscopy. Resistance to indentation measured by RPI on the periosteal surface of the proximal femurs also displayed comparable results in $LepR^{-/-}$ and $LepR^{+/+}$ animals ($p > 0.05$), indicating analogous mechanical properties of the bone matrix.

Due to the compositional nature of the contrast in BSE-SEM images, some relevant microstructural features were noted in both femurs and parietal bones. These structures were identified as islands of mineralized cartilage in the femurs, given their appearance as more highly mineralized, osteocyte-free areas surrounded by "normal" bone matrix. In the cross-sectional views of the parietal bones, areas with a greater degree mineralization were mostly located in the central portion of the section and in the regions close to the sagittal suture. The higher mineral content of both mineralized cartilage islands in the femurs and highly mineralized bone in the parietal bones was confirmed by high-resolution Raman maps (1 μm), although the increase in mineral content compared to bone matrix was not statistically significant ($p > 0.05$). Moreover, the composition of these microstructural features did not display any differences when comparing $LepR^{-/-}$ and $LepR^{+/+}$ animals ($p > 0.05$). qBEI data were examined in distinct intervals of wt% Ca to determine whether mineralized cartilage islands in the femurs and highly mineralized bone in the calvaria were differently distributed in the two animal groups. However, no differences were found ($p > 0.05$), indicating a comparable amount of these microstructural features.

PAPER II

This study examined the interface between bone and bacteria in a case of MRONJ developed by an osteoporotic female individual after 23 years of treatment with alendronate, a common bisphosphonate. The interface was characterized using different techniques spanning from the micro- to the nanoscale. Figure 9 shows the main results, summarized in the following page.

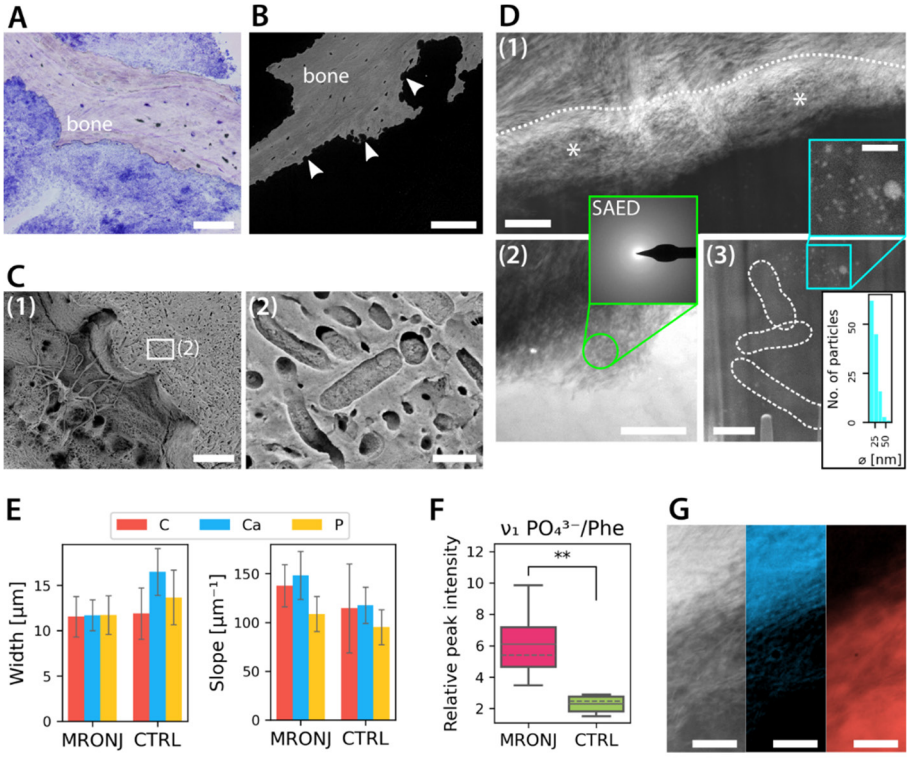

Figure 9. *Histological section (A) and BSE-SEM image (B) of necrotic bone, showing a ragged surface (arrowheads in B). SE-SEM images of necrotic bone after resin cast etching (C), where bacteria are clearly visible in the resin space (magnified in C-2). HAADF-STEM image of the bone-bacteria interface (D), demonstrating the presence of a hyper-mineralized band (dotted line in D-1) fading into a region of high disorder lacking crystallinity (marked by * in D-1), as confirmed by SAED (D-2). In the resin space, bacteria (dashed contour) and nanosized particulate can be observed (D-3). SEM-EDX indicates that the interface is narrower and more abrupt in necrotic bone ("MRONJ" label) (E), which micro-Raman spectroscopy confirms having a higher mineral content than non-necrotic bone ("CTRL" label), as shown by the higher mineral-to-matrix ratio ($\nu_1 PO_4^{3-}$/Phenylalanine, Phe) (F). EELS corroborates that calcium (blue) decreases across the bone bacteria-interface (G; left to right: HAADF image and EELS maps for calcium, in blue, and carbon, in red). Scale bars are 100 µm in A and B, 10 µm in C-1, 1 µm in C-2, 500 nm in D, and 200 nm in the blue inset in D-3 and G. ** denotes statistical significance ($p < 0.01$). [Adapted with permission from Paper II].*

Results summary: Paper II

Bone samples were retrieved from both non-necrotic and necrotic areas in the jaw of the individual diagnosed with MRONJ. Toluidine blue-stained histological sections confirmed the necrotic status of bone tissue sampled from the regions deemed necrotic in the oral cavity, while no signs of necrosis were evident in the non-necrotic sample. Bacterial colonization was also evident in the histological sections throughout the regions interfacing with necrotic bone.

Bacteria were imaged at higher resolution in SE mode in SEM after resin cast etching. Rod-shaped bacteria like those identified by the microbial swab (Prevotella and *Haemophilus*-like rods) were found in significant amounts in the outer space surrounding necrotic bone, which was filled with resin during sample embedding. Conversely, bacteria were absent in the resin region surrounding non-necrotic bone. In this case, bone cells like osteoblasts and bone lining cells were instead found at the bone-resin interface, while no such cells were noted in necrotic bone.

While already visible in histological sections examined by visible light microscopy, BSE-SEM images better highlighted differences in the morphology of the bone surface in the necrotic *vs.* non-necrotic samples. Specifically, the surface profile was irregular and jagged in necrotic bone, but had a rather smooth appearance in non-necrotic bone. Some mineral nodules resembling magnesium whitlockite were sometimes noted in the osteocyte lacunae in necrotic bone.

The degree of mineralization in bone close to the resin region was compared in necrotic and non-necrotic samples through the mineral-to-matrix ratio measured in micro-Raman spectroscopy. A higher ratio was found in necrotic bone, indicating a higher mineral content of the bone matrix ($p < 0.01$). Variations in calcium, phosphorus, and carbon were measured across the bone-resin interface by SEM-EDX, which revealed a more abrupt and narrower interface for the necrotic samples, although not in statistically significant terms ($p > 0.05$).

A region of necrotic bone interfacing with resin was resolved at the nanoscale by HAADF-STEM imaging. This made it possible to observe bacteria in the resin space, together with some high Z-contrast particulate located in their proximity or interior. This particulate had dimensions in the nanometer range, with an average size of 24 ± 8 nm. Away from the interface with the bacteria-filled resin space, bone displayed a normal ultrastructure, indicated by the characteristic banding pattern of in-plane collagen fibrils. The interface itself consisted of two main areas, i.e., a hyper-mineralized band (towards the bone side) and a highly disordered region (towards the bacteria side). The lack of crystallinity in this disordered region, where mineral appeared loosely organized, was confirmed by the absence of diffraction spots/rings in SAED patterns. EELS maps of calcium and phosphorus confirmed the decrease in mineral content from the hyper-mineralized band towards the resin region.

PAPER III

In this study, a multimodal and multiscale (micro-to-nano) characterization approach was applied to evaluate the bone response to a novel implant manufactured by L-PBF and designed to combine internal porosity, surface topography modification by acid etching, and surface functionalization with genistein for use in osteoporosis. Figure 10 summarizes the main observations.

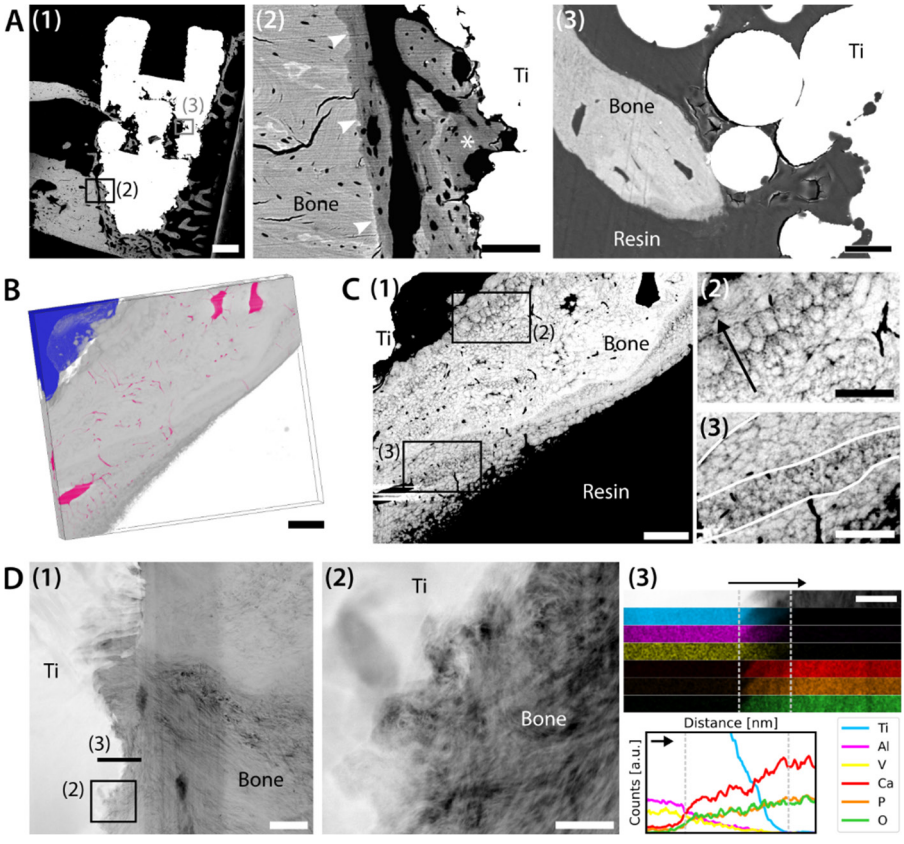

Figure 10. *BSE-SEM image showing new bone growth in the peri-implant space (A-1), and examples of distance osteogenesis (A-2, where arrowheads mark the boundary between native cortical bone and new bone) and contact osteogenesis (A-2, marked by *) also within the implant pores in contact with surface microparticles (A-3). PFIB-SEM 3D tomogram where an extensive LCN (pink) is present in peri-implant bone (bone is grey and implant is blue) (B) and an individual slice (C-1) where mineral ellipsoids display varying size (C-2; ellipsoids become larger in the direction of the arrow) and orientation (C-3; similarly oriented ellipsoids are enclosed by white lines). HAADF-STEM demonstrates osseointegration at the nanoscale (D-1, magnified in D-2) and STEM-EDX corroborates the gradual nature of the interface (D-3). Scale bars are 500 μm in A-1, 100 μm in A-2, 20 μm in A-3, 10 μm in B and C-1, 5 μm in C-2 and C-3, 1 μm in D-1, and 200 nm in D-2 and D-3.*

Results summary: Paper III

Instances of both distance and contact osteogenesis were observed in BSE-SEM survey images in the peri-implant compartment. Distance osteogenesis was especially apparent thanks to the compositional-contrast of BSE-SEM, making it possible to distinguish older bone in the native cortices from newer bone formed as part of the osseointegration process. The most significant example of contact osteogenesis was provided by bone ingrowth in the internal porosity of the implant. Bone in contact with the implant was also noted in correspondence of surface microparticles characteristic of parts manufactured by L-PBF.

Osseointegration was confirmed at the nanoscale by HAADF-STEM imaging and STEM-EDX. Specifically, bone and implant formed a continuous and gradual interface, where implant elements and bone elements intermixed. Such an intimate contact was mediated by the TiO_2 passivation layer that spontaneously forms on titanium, as oxygen was also detected within the bone-implant interface.

Bone regeneration in the peri-implant space was also assessed by examining the LCN. Despite a thin layer of resin or cracks being sometimes present at the bone-implant interface, SE-SEM images after resin cast etching demonstrated canaliculi extending towards the implant surface. This was better shown over a larger field of view and in 3D with PFIB-SEM tomography. Several osteocyte lacunae were present in the implant space, mostly co-aligned with each other and with their longest dimension parallel to the implant surface. Their canaliculi ran in the perpendicular direction, i.e., reaching towards the implant surface.

Some high Z-contrast features resembling cell membranes enclosing intracellular bodies were also noted in the PFIB-SEM image stack. When these features were close to the bone front, they could offer insights into the direction of the mineralization front. Two fronts were noted, one directed towards the implant, and one away from it. One lacuna becoming progressively enclosed by the bone matrix was also observed, likely indicating that an osteoblast-to-osteocyte transition was taking place as osteoid mineralization proceeded.

Mesoscale bone structure imaged by PFIB-SEM tomography revealed the presence of mineral ellipsoids with heterogenous sizes and orientations, as abrupt transitions from regions where they were cross-sectioned transversally *vs.* longitudinally were present throughout the 3D volume. Differing orientations were also confirmed at the nanoscale in HAADF-STEM images, where collagen fibrils transitioned from in-plane to out-of-plane views.

PAPER IV

This work examined the effect of bioactive glass (Biogran®) functionalized with PTH 1-34 on bone repair and osseointegration in ORX rats (abbreviated as ORQ in the Paper). Both the biological response and the micro-to-nanoscale characteristics of peri-implant bone were studied. Figure 11 shows some of the relevant findings.

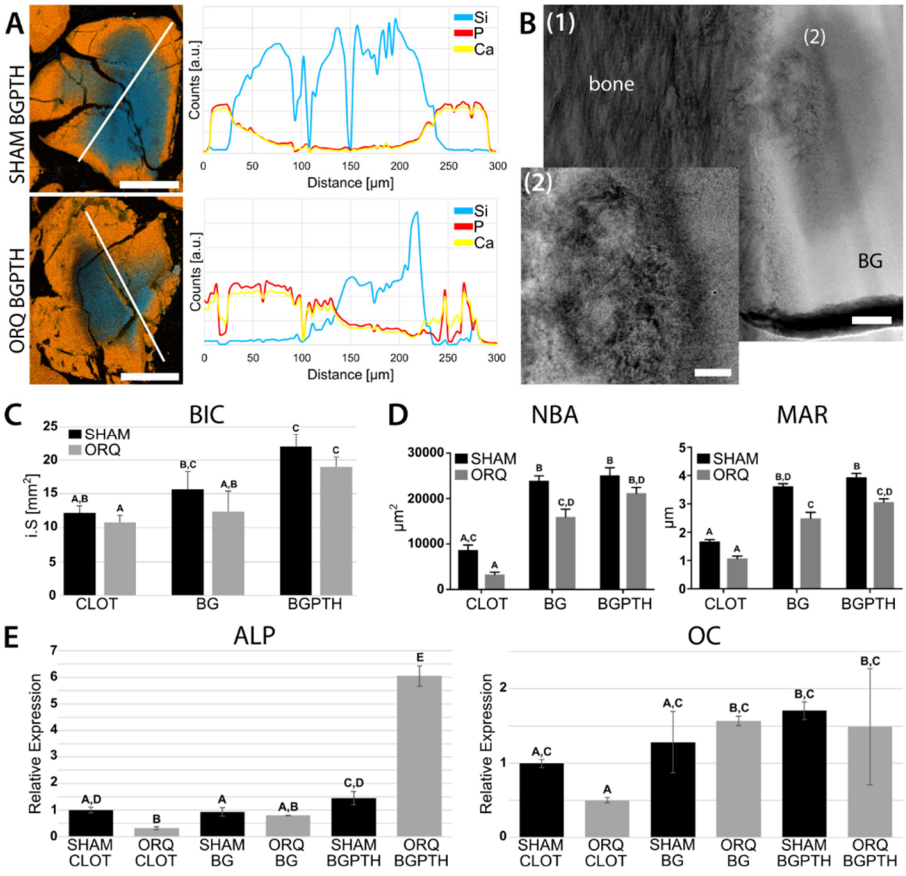

Figure 11. *SEM-EDX maps of silicon (blue), phosphorus (red), and calcium (yellow) for Biogran® particles functionalized with PTH 1-34 placed in the control (SHAM BGPTH) and ORX groups (ORQ BGPTH), and relative line scans across the particles (white lines) (A). HAADF-STEM images of the bone-Biogran® (BG) interface for particles functionalized with PTH 1-34 in an ORX animal (B), where dissolution/reprecipitation can be observed, together with bone formation within the particle (magnified in B-2). Bar plots summarizing the measurements obtained for: BIC (C); neoformed bone area (NBA) and mineral apposition rate (MAR) (D); and gene expression of alkaline phosphatase (ALP) and osteocalcin (OC) (E). Labels indicate: SHAM - healthy animals; ORQ - ORX animals; CLOT - animals receiving no Biogran®; BG and BGPTH - animals receiving Biogran® without and with PTH 1-34 functionalization, respectively. Scale bars are 100 µm in A, 500 nm in B-1, and 200 nm in B-2. Different letters denote statistical significance ($p < 0.05$). [Adapted with permission from Paper IV].*

Results summary: Paper IV

Rats were subjected to ORX or placebo surgery (SHAM). In both ORX and SHAM groups, one sub-group did not receive Biogran® (CLOT group), while the surgical defect was filled with Biogran® without and with PTH 1-34 functionalization in the sub-groups labelled as BG and BGPTH, respectively, prior to implant installation.

Contrast differences between the inner and outer portions of the Biogran® particles in the peri-implant space were often noted in BSE-SEM images. Compositional gradients were confirmed by SEM-EDX maps, showing that the particles were richer in silicon in their core, and in calcium and phosphorus towards their exterior. This was observed for both functionalized and non-functionalized particles. The silicon-rich core appeared more extended in the healthy animals than in the ORX ones, but sample size did not allow for statistical comparisons.

The formation of a gradual interface between bone and Biogran® was confirmed at the nanoscale by HAADF-STEM imaging, demonstrating the presence of an interfacial layer created by dissolution and reprecipitation ranging from 150 nm to 900 nm in width. In two samples, SHAM BG and ORX BGPTH, bone ingrowth in cavities within the biomaterial was also noted. Regarding bone ultrastructure, collagen fibrils mostly oriented parallel to the Biogran® surface were observed in all groups. In the ORX samples, mineral ellipsoids were also distinguished.

Micro-CT revealed higher bone volume in the animals receiving Biogran®, both with and without PTH 1-34 functionalization, accompanied by a lower trabecular separation and higher trabecular number than in the animals with implant only ($p < 0.05$). On the other hand, trabecular thickness was comparable in all groups ($p > 0.05$). Removal torque was overall lower in ORX than healthy animals, while higher values were measured in BG and BGPTH groups compared to CLOT for both healthy and ORX animals, especially in the SHAM BGPTH group ($p < 0.05$). Similar trends were found in BIC measurements. In this case, the use of functionalized Biogran® led to a statistically significant increase in BIC in both ORX and healthy animals compared to those receiving the implant only ($p < 0.05$). In both removal torque and BIC measurements, values in the ORX BGPTH group were comparable to those of the SHAM BG group ($p > 0.05$). This trend was also identified in the fluorochrome (calcein and alizarin red) analyses in terms of fluorochrome area, neoformed bone area, and mineral apposition rate. Additionally, values of neoformed bone area did not show any statistically significant difference between healthy and ORX animals that received functionalized Biogran® ($p > 0.05$).

ORX animals that received functionalized Biogran® had a significantly higher expression of alkaline phosphatase compared to all the other groups ($p < 0.05$). Osteocalcin expression was greater in the ORX animals receiving Biogran®, regardless of the presence of PTH 1-34, compared to those with the implant only ($p < 0.05$). In ORX animals, TRAP (tartrate-resistant acid phosphatase) immunolabelling was discrete in the CLOT group, discrete-to-moderate in the BG group, and moderate in the BGPTH group. In the healthy controls, discrete-to-moderate labelling was found in the sub-groups receiving Biogran®.

PAPER V

This study provided a workflow for the characterization of the interface between bone and bioactive glass (Biogran®), as well as for the ultrastructure of newly formed bone, going from 2D microscale imaging to 3D reconstruction with electron tomography at the nanoscale. The main results are graphically summarized below (Figure 12).

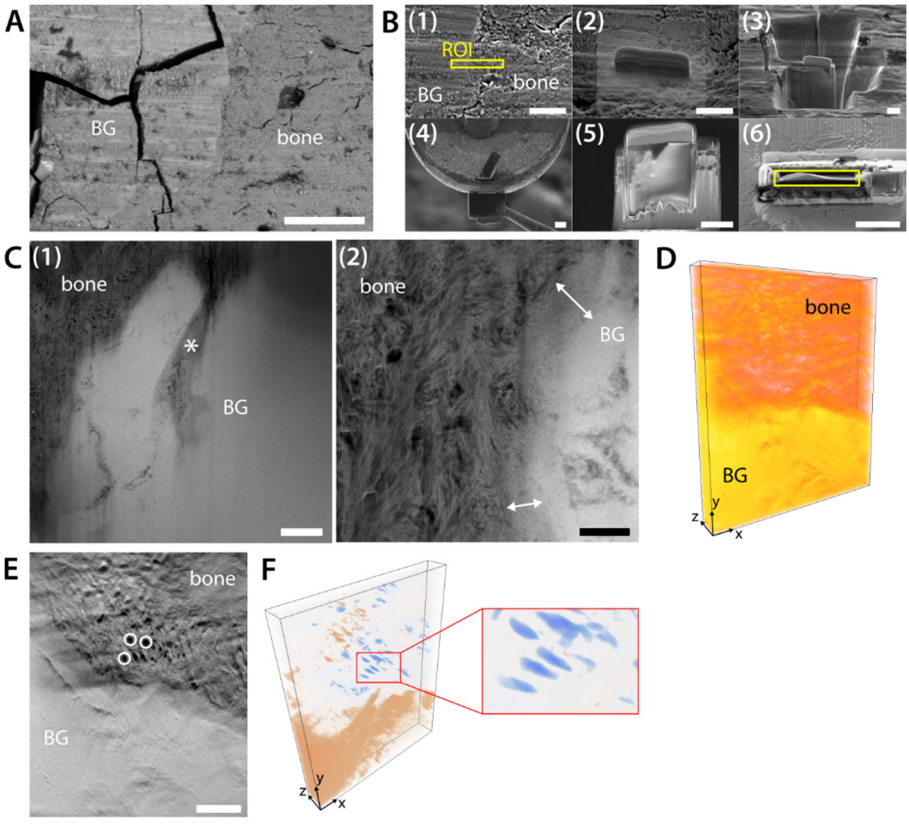

Figure 12. *Area of new bone growing in close contact with a Biogran® (BG) particle (A; BSE-SEM image), where a ROI was selected to prepare a STEM sample by FIB in situ lift-out (B-1, yellow rectangle). The main sample preparation steps involved depositing a protective coating over the ROI (B-2), milling coarse trenches around it (B-3), lifting-out and attaching the sample to a copper grid (B-4), and thinning to electron transparency (B-5; final sample is marked by the yellow rectangle in B-6). HAADF-STEM images show bone-Biogran® contact at the nanoscale with bone ingrowth within Biogran® cavities (* in C-1) and the formation of a 120-200 nm-wide interfacial layer (C-2, white arrows). Nano-osseointegration is confirmed in 3D by electron tomography (D). Collagen fibrils can be seen out-of-plane in individual reconstructed slices (E, white circles), and 3D rendering clearly shows they are parallel to the Biogran® surface (F; blue rods represent collagen fibrils). Scale bars are 20 μm in A, 5 μm in B, 1 μm in C-1, 200 nm in C-2, and 250 nm in E. The dimensions (x, y, z) of the 3D volume in E and F are 1231 × 1494 × 161 nm³. [Adapted with permission from Paper V].*

Results summary: Paper V

After the retrieval *en bloc* of the implant together with its peri-implant space, which included both new and native bone, as well as Biogran® particles, samples were prepared by embedding, sectioning, and polishing for electron microscopy experiments. A thin layer of conductive coating (carbon) was applied to minimize charging in high-vacuum imaging conditions.

BSE-SEM imaging was completed to identify areas of new bone forming in contact with Biogran® particles. Bone and biomaterial displayed a similar contrast, as they both contain calcium and phosphorus. Bone was easily identified by the presence of osteocyte lacunae, while cracks were often observed running through the Biogran® particles. Compositional gradients within the Biogran® particles could be inferred from BSE-SEM images due to the presence of a darker core surrounded by a brighter outer layer.

From the BSE-SEM survey, an area of bone-Biogran® contact on the microscale level was selected for the preparation of an electron transparent sample for STEM experiments. This was accomplished following a FIB *in situ* lift-out protocol in a dual-beam instrument, which allowed for the preservation of an intact interface, despite the different milling behaviour of bone and Biogran® posed some technical challenges.

HAADF-STEM imaging confirmed that the contact between new bone and Biogran® was continuous at the nanoscale, beyond what could be resolved by BSE-SEM. The Z-contrast in HAADF-STEM images also made it possible to better visualize the compositional gradients present in such a gradual interface, for which the term "biointerphase" is perhaps more appropriate. This was further corroborated in 3D by Z-contrast electron tomography, especially when examining individual slices of the reconstructed volume.

Nanoscale imaging in both 2D and 3D also provided information on the ultrastructure of bone forming in contact with Biogran®. Overall, new bone did not appear highly organized, but some distinct collagen fibrils could be distinguished. The fibrils appeared out-of-plane in HAADF-STEM images, but were better visualized and segmented in the 3D electron tomogram. This analysis confirmed that the collagen fibrils were oriented parallel to the biomaterial surface.

PAPER VI

In this work, a correlative characterization approach combining on-axis Z-contrast electron tomography and EDX tomography was used to resolve nanoscale features in human bone, with a focus on the low-contrast nanosized spaces (termed "holes" in the Paper) typical of the lacy pattern of bone, and on the morphology and spatial organization of bone mineral, especially the extra-fibrillar component. Figure 13 provides an overview of the main results.

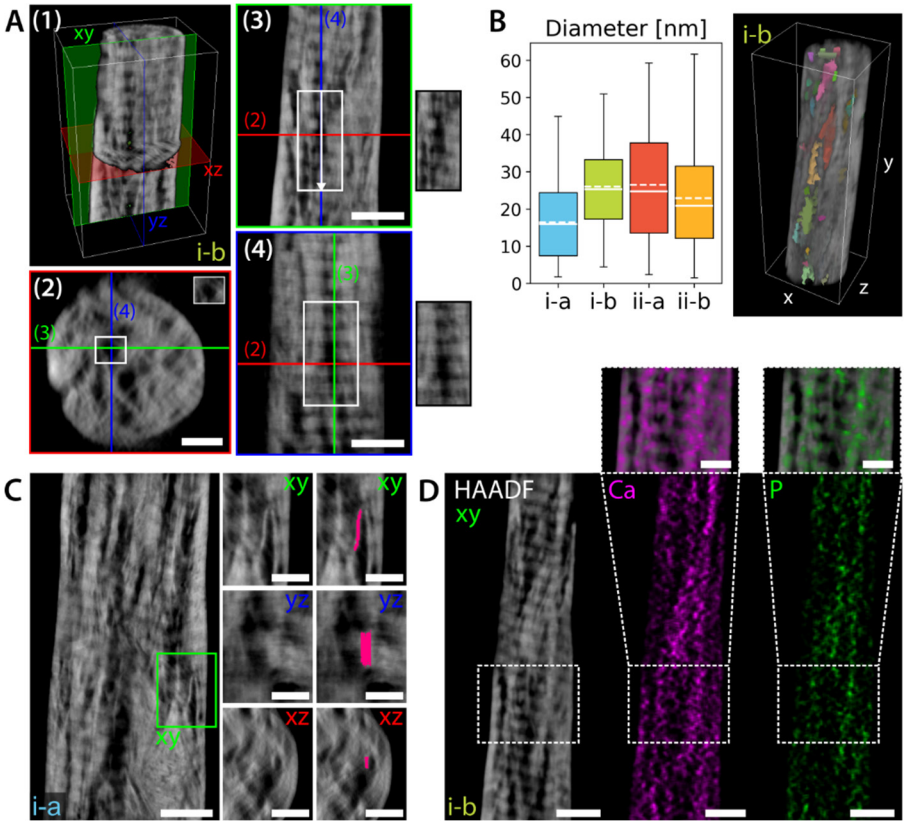

Figure 13. *3D reconstruction (A-1) showing three representative mutually orthogonal slices where a "hole" in the xz plane (A-2, red) corresponds to banding pattern in the xy (A-3, green) and yz (A-4, blue) planes, demonstrating correspondence between "holes" and collagen fibrils. "Holes" have an average diameter going from 16.4 nm to 26.4 nm in the four tomograms (B, box plot) and are disconnected from each other (B, 3D rendering). Mineral structures appear plate-shaped when viewed in three mutually orthogonal planes (C). EDX reconstructed maps demonstrate presence of calcium and phosphorus both in the intra- and extra-fibrillar regions, although the signal appears stronger in the latter (D). The labels "i-a" and "i-b" refer to the naming convention used for the tomograms in the Paper. Scale bars are 100 nm in A-2, C (right magnified panels), and D (top magnified panels), and 200 nm in A-3, A-4, C (left image), and D (bottom images). The dimensions (x, y, z) of the white boxes in the 3D reconstructions are 555.55 × 865.10 × 457.15 nm³ in A-1 and 555.55 × 1611.30 × 457.15 nm³ in B.*

Results summary: Paper VI

Two rod-shaped samples were prepared from individual osteonal lamellae in the femoral cortex by FIB annular milling. The samples were almost cylindrical, with a diameter going from 200-300 nm at the top to 700 nm at the bottom. In one of the samples, the banding pattern of collagen fibrils was observed along the rod length at all tilt angles, confirming collagen fibrils oriented in-plane. In the other sample, the banding pattern was noted only at certain tilt angles, while disordered or more mineral-rich regions, resembling rosettes, were present at other orientations. These features, i.e., collagen banding pattern and rosettes, were also identified in three conventional wedge-shaped samples prepared by FIB *in situ* lift-out. These samples, having known orientations with respect to the osteonal axis, confirmed the characteristic longitudinal and lacy motifs observed in bone in mutually orthogonal sections. Correspondence between the longitudinal and lacy motifs was confirmed by the electron tomography 3D reconstructions when reslicing along representative orthogonal planes. This demonstrated the reciprocity between the "holes" in the lacy motif and the collagen banding pattern in the longitudinal motif. In particular, "holes" appeared to mostly match the overlap regions of the collagen fibrils.

Segmentation of the "holes" in 3D over the entire tomograms showed that their shape is approximately that of rods. These rods were mostly disconnected from each other, and aligned with their long axis in the direction orthogonal to the banding pattern, i.e., in the same direction as the collagen fibrils. The average diameter of the "holes" in the four datasets examined varied from 16.4 nm to 26.4 nm. In one tomogram where a partial mineral ellipsoid was observed, the 3D segmentation of the "holes" showed that these features were mostly located outside the ellipsoid around its periphery.

Simultaneously to Z-contrast electron tomography acquisition, EDX tomography was completed to acquire elemental maps of calcium and phosphorus, representative of the mineral phase, and carbon and nitrogen, representative of the organic phase (type I collagen). EDX maps of carbon and nitrogen appeared quite noisy due to the overall weak signal, hence they proved to be inconclusive in determining the composition of the "holes". Nonetheless, the intersection analysis between the segmented "holes" and the reconstructed EDX maps showed higher spatial correspondence of the "holes" with the maps of carbon and nitrogen over those of calcium and phosphorus.

From the reconstructed EDX maps it was possible to observe the presence of calcium and phosphorus in the gap zones of the collagen fibrils, demonstrating intra-fibrillar mineralization. However, the signals of these two elements appeared more intense in correspondence with the extra-fibrillar component. In the extra-fibrillar space, some individual mineral structures were segmented, showing that bone mineral is in the form of plates with dimensions around 5-9 × 33-43 × 100 nm^3. The extra-fibrillar mineral also seemed to be mostly interconnected and spanning over multiple collagen fibrils.

Discussion

Two conditions affecting bone quantity and/or quality were subject of study in this thesis: LepR deficiency, associated with hyperglycemia (T2DM-like) and obesity in the Lund MetS rat model[110,188] [Paper I]; and osteopenia/osteoporosis, typical of the aging population and mimicked by hormone deficiency in OVX/ORX animal models[120,121] [Papers III-IV]. An extreme case of impaired bone metabolism, i.e., necrotic bone, resulting from anti-resorptive therapy (MRONJ) was also examined [Paper II].

Abnormalities in the overall energy metabolism, such as in the combination of hyperglycemia, obesity, and LepR deficiency[102], or more specifically in bone metabolism, such as imbalanced bone remodeling in osteoporosis[112], can impact not just biological functions, but also structural and compositional properties of the bone matrix. These changes in material properties can be reflected at various levels of bone's architecture, in turn affecting bone strength[83,84]. In the studies included in this thesis, a characterization approach typical of materials science was thus adopted, often combining different tools (multimodal characterization) to access information across several length scales (multiscale characterization), with a focus on the micro-nano continuum. The need for such a multimodal and multiscale approach stems from the trade-off between the volume of material that can be analyzed and the spatial resolution achievable[159,195,196]; the higher the resolution required, the smaller the volume that can be analyzed, especially when acquisition time matters.

The following sections discuss in more detail the application of multimodal and multiscale tools in probing bone quality-related aspects in compromised conditions affecting native bone (first section of this chapter) and osseointegration (second section of this chapter). A discussion on advanced characterization techniques and their implications on our understanding of bone ultrastructure concludes this chapter.

MULTIMODAL AND MULTISCALE CHARACTERIZATION OF DISEASED BONE

An example of multimodal characterization applied to bone is offered by Paper I. Therein, such an approach was selected to determine structural and compositional properties of bone matrix at the microscale in a novel preclinical model for T2DM/MetS, the Lund MetS rat[110,188]. To this author's knowledge, this is the first study examining skeletal attributes of the Lund MetS rat, originally investigated for diabetic vascular complications[110,197,198]. Rat models are frequently employed in preclinical research due to their low cost and good availability, although some dissimilarities in bone metabolism compared to human bone exist, such as the lack of Haversian remodeling[199]. Hence, when a new model is developed, a better understanding of its bone structure and composition is necessary to understand potential translation into human bone research. Interestingly, the LepR-deficient Lund MetS animals examined in Paper I displayed similar microstructural alterations to those commonly reported in widespread monogenic models of obesity with LepR deficiency, i.e., the Zucker fatty and Zucker diabetic fatty rat[200–202]. A deteriorated architecture in the trabecular compartment has also been reported in humans with T2DM[203]. The structural changes observed in the LepR-deficient animals encompassed both the overall bone geometry, with shorter femurs and thinner parietal bones, and the microstructure, with thinner cortices and fewer trabeculae, as well as shorter and less interdigitated sagittal sutures. All these alterations point towards a delayed skeletal development in the LepR-deficient rodents, independently on the ossification mechanism, i.e., endochondral in the femur and intramembranous in the parietal bones of the calvarium. Humans with congenic Lep/LepR deficiency also display severe obesity and delayed growth[107–109], hence suggesting that the Lund MetS rat could find applications in this translational research context.

Regarding the characterization of bone structure, the use of micro-CT in Paper I confirmed the advantages of quantitative morphometry in 3D over 2D, as microstructural differences between groups were not apparent in BSE-SEM images. On the other hand, the greater resolution of SEM compared to micro-CT, combined with the compositional-contrast in BSE-SEM, made it possible to attest to the presence of mineralized cartilage islands in the femurs and highly mineralized bands in the parietal bones. Mineralized cartilage islands, in particular, are a relevant structural feature in rat bone, but are absent in larger mammals, including humans, as they are likely removed by Haversian remodeling[204,205]. Hence, more attention should be paid to better characterize these islands in the future.

In both Paper I and Paper II, direct imaging to qualitatively/quantitatively probe structural aspects was combined with compositional analyses, primarily using spectroscopy, but also based on calibration of BSE-SEM images using a qBEI approach in Paper I. Specifically, in Paper I, characterization of bone composition was accomplished in a truly multimodal way, combining three techniques with different

probes (red light, X-rays, electrons) and targeting progressively smaller fields of view at increasingly smaller pixel/voxel size, exemplifying the compromise between volume analyzed and resolution. This helped confirm the comparable bone matrix composition in LepR-deficient and healthy animals, ruling out technique-dependent limitations in capturing eventual differences. Not surprisingly, the comparable composition was reflected by analogous resistance to indentation, as RPI is more sensitive to local structural/compositional properties of the bone matrix[206].

Paper II expands the multimodal characterization approach by encompassing length scales from the micro- to the nano-level. Specifically, nanoscale imaging provided valuable insights into the impact of MRONJ on bone, beside the necrosis already apparent on a "macroscopic" level in the oral cavity. In a sense, necrotic bone can be considered as an extreme case of diseased bone. In this context, it is relevant to shed light on what happens where the necrotic bone front interfaces with the surrounding environment, where biofilm formation is commonly observed[142–144]. Bacterial colonization in necrotic bone in Paper II was confirmed by histology, a more traditional examination, as well as by SE-SEM imaging after resin cast etching. Treatments to remove or preserve specific elements can provide additional information compared to what an embedded and polished bone sample can reveal[154,157]. For example, in Paper II, resin cast etching was used, for the first time, to expose bacteria in a case of MRONJ. This confirmed the extensive bacterial colonization at a much higher resolution than that of visible light microscopy, allowing for a better visualization of the rod shape of the bacteria, while excluding the presence of mineralized bacteria seen instead in dental calculus[207]. Moreover, after resin cast etching, the presence of osteoblasts and bone lining cells in non-necrotic bone, or better, their absence in necrotic bone, could be noted, indicating no ongoing mineralization at the necrotic bone front. This qualitative observation was supported by the determination of compositional gradients across the interface between bone and resin (filled with bacteria in MRONJ) using SEM-EDX, and of bone mineral content close to said interface using micro-Raman spectroscopy.

A multiscale imaging approach similar to that used for bone-biomaterial interfaces, involving microscale imaging with BSE-SEM followed by nanoscale analyses with HAADF-STEM[57], was applied to probe the interface between necrotic bone and the bacteria-invaded resin in Paper II. This nanoscale resolution of the interface provided new insights into the role of bacteria in MRONJ. The structure and composition of the interface, consisting of both a hyper-mineralized band and a disordered and amorphous region, together with particulates around and within the bacteria, suggests that bacteria may have an active role in degrading bone *in vivo*. It is especially relevant for this discussion section to point out that, while SEM-EDX and micro-Raman spectroscopy indicated mineralization abnormalities in necrotic bone, only direct imaging at higher resolution by HAADF-STEM made it possible to determine the nature of the bone-bacteria interface, further corroborating the importance of multiscale characterization.

MULTIMODAL AND MULTISCALE CHARACTERIZATION OF BONE INTERFACES

An intriguing possibility is that of using bone implants as drug-eluting platforms to promote osseointegration and/or suppress undesired phenomena such as inflammation and infection. Currently, clinical applications are limited, but *in vitro* and preclinical research on the subject is quite extensive[77]. In this thesis, two different systems for local drug delivery aiming to counteract the increased bone resorption in osteoporosis, which may affect osseointegration[125], were investigated: an AM Ti-6Al-4V implant functionalized with genistein, a phytoestrogen [Paper III]; and particles of bioactive glass (Biogran®) functionalized with PTH 1-34, an anabolic agent [Paper IV]. Both these drugs offer an alternative to bisphosphonates, for which side affects like MRONJ have been reported[137–140], as also highlighted in Paper II.

Bone response to the biomaterial solutions for local drug delivery proposed in Papers III-IV was evaluated with a multiscale and multimodal characterization approach to examine osseointegration in a comprehensive way across several length scales of interest. This characterization workflow is well exemplified by Paper III, where analyses focused on both the bone-implant interface and the LCN in peri-implant bone going from the micro- to the nanoscale. At the microscale, BSE-SEM images provided information on new bone formation in the peri-implant space, especially in regard to the osseointegration "direction", i.e., distance *vs.* contact osteogenesis[61]. Beyond the microscale, HAADF-STEM images and STEM-EDX confirmed nano-osseointegration. Although these analyses are not routinely performed in osseointegration studies, their application has been demonstrated before[171,172,183]. The main element of novelty in Paper III lies within bridging these two length scales with examinations targeting the mesoscale. This was enabled by PFIB-SEM tomography, a relatively new tool in bone research with limited applications to date[31,208]. Compared to traditional FIB-SEM tomography using a Ga^+ ion beam, bigger volumes of material can be probed with Xe^+ PFIB-SEM, while preserving a good spatial resolution[31,160]. At the bone-implant interface, this means being able to examine the peri-implant space at greater distances from the implant surface and over bigger depths (where "depth" refers to the direction perpendicular to the image plane). In Paper III, seven osteocyte lacunae and relative canaliculi were distinctly visualized in the PFIB-SEM volume. As osteocytes have an important function in mechanotransduction, including when connected to the implant surface[60], PFIB-SEM tomography can find applications in the study of their organization in newly formed bone, offering complementary information, and an additional dimensionality, to 2D SEM images after resin cast etching.

The advent of P/FIB-SEM tomography in bone research has also opened possibilities in the 3D characterization of bone hierarchical structure at the mesoscale, where features are smaller than those resolved with micro-CT and span a larger field of view than those available with electron tomography. Recent studies using this technique have shown that

bone mineral forms ellipsoidal aggregates[22,31], which tessellate the collagen matrix in a cross-fibrillar pattern[22]. These features were identified and reviewed by the author of this thesis in HAADF-STEM images of both native and peri-implant bone (see reference 33). Hence, given their increased recognition, examination of mineral ellipsoids was undertaken in Paper III. Therein, the mineral ellipsoids showed varying sizes, in some instances displaying transverse cross-sections larger than those reported in previous studies[22,31]. This could be due to the systemic impairment in bone regeneration in OVX rats and/or to the local release of genistein. Sudden changes in ellipsoid orientation from longitudinal to transverse views within the image plane were also noted, confirming what was found in the only other PFIB-based work examining ellipsoids in peri-implant bone to date[208]. The origins and implications of size and orientation variations of the mineral ellipsoids are not known, hence P/FIB-SEM tomography should increasingly be implemented in the osseointegration characterization workflow. Transverse cross-sectional views of mineral ellipsoids, i.e., rosettes, were also observed in HAADF-STEM images of the bone-bioactive glass interface in Paper IV, providing yet further evidence of their ubiquitous nature.

A similar approach to that presented in Paper III was applied in Paper V, which placed additional emphasis on nanoscale characterization using electron tomography to resolve the bone-biomaterial interface in the third dimension, limiting overlapping artifacts in 2D S/TEM projection images. Two very dissimilar biomaterials, i.e., a permanent Ti-6Al-4V implant and a degradable bioactive glass, were studied in Paper III and Paper V, respectively, showcasing the versatility of multiscale characterization workflows for bone-biomaterial interfaces. However, these investigations were limited one/two samples, which is often the case in osseointegration studies, in particular when targeting the nanoscale. This workflow can be used as a first approach to minimize the number of animals required when gaining insights into bone response to specific biomaterials, for example for novel implant designs such as that in Paper III. However, the biological response to biomaterials should also be determined in a more quantitative way. In Paper IV, the micro-to-nanoscale evaluation of the bone-implant interface was implemented in a broader characterization context to assess biomechanics, mineralization dynamics, bone resorption, and gene expression. From these analyses, it emerged that Biogran® functionalized with PTH 1-34 could be a promising solution to improve osseointegration in osteoporotic conditions. In fact, ORX rats receiving the functionalized particles often displayed a similar behaviour as the control group receiving non-functionalized Biogran®. Conversely, PTH 1-34 functionalization did not seem to play any additional role in promoting bone repair in healthy animals. A similar preclinical investigation should be conducted for the genistein-functionalized implant in Paper III, although a pilot study (*unpublished*) demonstrated improvements in bone repair.

Despite its wide clinical use, there are not many studies focusing on the bone-Biogran® interface at the nanoscale. This lack was compensated for by Paper V, where both 2D STEM and 3D electron tomography experiments were completed. Compared to previous work where the interface between bone and bioactive glass was resolved in BF-TEM[209], Z-contrast in HAADF-STEM better captured the compositional gradients at the

interface. Individual cross-sectional slices in the reconstructed electron tomogram corroborated that the dissolution/reprecipitation layer is characteristic of this type of interface, and not an artifact arising from feature overlap in 2D HAADF-STEM images. By using electron tomography, it was also possible to better visualize collagen fibrils and their orientation relative to the biomaterial surface in 3D. Nanoscale resolution of the bone-Biogran® interface by HAADF-STEM was also employed in Paper IV. This confirmed that the formation of a gradual interface was not affected by the functionalization with PTH 1-34, nor by systemic changes induced by ORX.

The effects of biomaterial implantation are not limited to the host, but changes also occur in the biomaterial itself[210]. In Paper V, these changes were evident in BSE-SEM images of Biogran® particles where compositional gradients from the core to the outer regions and extensive cracks were observed in the particles, overall confirming known mechanisms of ion exchange and dissolution of bioactive glasses[75,76]. In Paper IV, SEM-EDX showed that neither PTH 1-34 functionalization nor hormone deficiency due to ORX altered the behaviour of Biogran® *in vivo*. Interestingly, ion exchange appeared slightly enhanced in the ORX rats. Further analyses, e.g., involving a greater sample size, should be completed to confirm this enhancement and determine eventual causes, possibly related to differences in local pH or availability of calcium and phosphorus.

EXTENDING THE FRONTIERS OF NANOSCALE CHARACTERIZATION IN BONE RESEARCH

A powerful prospect in multiscale/multimodal characterization stems from the possibility of correlating structural and composition information in 3D, opening avenues into "4D characterization", where the fourth dimension refers to the chemistry[55]. At the nanoscale, 4D characterization can be accomplished by combining S/TEM electron tomography to acquire images and resolve structural details, with spectroscopy tomography, using energy-filtered TEM, STEM-EDX, or STEM-EELS to obtain elemental maps in 3D[211,212]. In bone research, the correlative use of Z-contrast electron tomography and EELS tomography has been applied at the interface between human bone and a dental cp-Ti implant, revealing nanoscale integration between bone elements and the TiO_2 surface oxide[187]. In this thesis, on-axis Z-contrast electron tomography was instead combined with EDX tomography to address some of the debated aspects regarding bone ultrastructure [Paper VI]. Despite EELS typically yielding higher spatial resolution than EDX[184], EDX tomography was chosen over EELS tomography in Paper VI to simplify the acquisition workflow, as well as to avoid the strict limitations in sample thickness in EELS. In fact, the rod-shaped samples used in Paper VI were thicker than common electron transparent bone samples (e.g., 100-200 nm in Papers III-V), with diameters up to 700 nm. This made it possible to reconstruct more information in the direction perpendicular to the image plane (z direction), while preserving the nanoscale resolution typical of electron tomography. Resolution in Paper VI was further improved due to the on-axis nature of the electron tomography acquisition, where rod-shaped samples are mounted on a specialized holder that allows to access the missing wedge region forbidden in conventional single-tilt experimental set-ups (i.e., beyond ±70°)[173,175]. Previous electron tomography work on bone-implant interfaces showed that extending the tilt range to encompass high tilt angles, up to ±90°, led to a greater fidelity and quality in the final reconstruction[179]. This was confirmed in Paper VI, despite the larger diameter of the rod-shaped samples used. Improvements in the reconstruction in on-axis electron tomography *vs.* conventional electron tomography were also observed when comparing Paper VI with Paper V, where elongation artifacts typical of the missing wedge were present.

Overall, Paper VI showcased a new technique to expand the characterization toolbox for bone research where artifact-free 3D reconstructions of structure and composition can be obtained for relatively thick samples. Most importantly, this technique also offered new insights into bone ultrastructure. This is especially significant considering the essential role of the mineralized collagen fibrils as building block units not only of native bone[9], but also of bone-biomaterial interfaces[56]. The spatial organization of collagen fibrils and mineral, together with the morphology of the mineral phase, can indeed influence the mechanical properties of bone[213], but also determine diffusion pathways within the bone matrix.

One key aspect investigated in Paper VI was the nature of low-contrast regions, the "holes", characteristic of the lacy pattern of out-of-plane collagen fibrils[169]. It is worth pointing out that these "holes" were deemed to be cross-sectional views of collagen fibrils in Papers IV-V (chronologically antecedent to Paper VI), adopting the interpretation proposed by several authors[21,168–170,177,214]. However, this correspondence is not universally accepted in the bone research community, and other authors have identified the "holes" as nanochannels[163,164], intra-fibrillar unmineralized spaces hosting macromolecules[215], or provided no clear explanation other than their unlikely correspondence to collagen fibrils[23]. Thanks to on-axis electron tomography in Paper VI, direct confirmation of the fact that most "holes" are collagen fibrils seen in cross-section was obtained. Dissimilarly from previous work assessing this relationship in a more global way through the reciprocity of longitudinal and lacy motifs[169,170], Paper VI provided direct evidence of the collagenous nature of the "holes" in a nearly point-specific manner by slicing the electron tomography reconstructions in mutually orthogonal planes. This demonstrated that the "holes" correspond to dark bands, i.e., overlap zones, in the banding pattern of in-plane fibrils. Interestingly, the rod-like appearance of "holes" segmented in 3D can also be observed in the visualization/segmentation of the electron tomogram in Paper V. However, the more optimal orientation of the samples in Paper VI and their rod shape, together with the removal of missing wedge artifacts thanks to on-axis electron tomography, allowed for more detailed analyses of the "holes".

In Paper VI, EDX tomography proved to be more suited to the analysis of bone mineral rather than of the organic phase. By considering individual 2D slices in the 3D reconstructed maps of calcium and phosphorus and correlating them to the corresponding HAADF-STEM slices, it was possible not only to confirm intra-fibrillar mineralization, but also to reveal higher signal intensity for the extra-fibrillar mineral. Conversely, reconstructed maps of carbon and nitrogen appeared rather noisy and could not be well correlated to specific structural features such as the "holes". A 4D characterization tool not explored in this thesis which could overcome this limitation is atom probe tomography (APT), where compositional information is spatially resolved in 3D by exploiting field ion microscopy and mass spectrometry[216]. APT combines ppm (parts per million) chemical sensitivity with nanoscale spatial resolution[216], making it possible to study individual collagen fibrils, as demonstrated by Lee et al. in leporine bone[217]. Other uses of APT in bone research have focused on resolving bone-implant interfaces at the atomic scale[187,218,219]. These and other applications of APT in bone and other biominerals were reviewed by the author of this thesis and co-workers (see reference 196).

Conclusions

Overall, the multimodal and multiscale characterization approach applied in this thesis revealed structural and compositional changes of bone in the compromised conditions examined, informed perspectives on biomaterial functionalization strategies to improve bone response in the presence of disease, and shed light on the ultrastructure of bone in both native tissue and at biomaterial interfaces.

In Paper I, the multimodal characterization of bone structure and composition highlighted geometrical and microstructural abnormalities in LepR-deficient Lund MetS rats, indicating a delay in their skeletal development which did not seem to affect bone matrix composition.

In Paper II, the multiscale investigation of the bone-bacteria interface in a case of MRONJ, especially when considering nanoscale information, demonstrated the existence of a hyper-mineralized band fading into an amorphous and disordered region. This suggests that, together with uncontrolled precipitation of calcium and phosphorus from the surrounding environment, bacteria actively degrade bone in MRONJ.

In Paper III, micro-to-nanoscale characterization of the interface between bone and an AM porous implant, acid-etched, and functionalized with genistein, showed a promising bone response despite the compromised bone repair in OVX rats. Moreover, Paper III highlighted the importance of including mesoscale analyses to investigate the LCN in 3D and the organization of mineral ellipsoids in peri-implant bone.

In Paper IV, microscopy-based analyses of the interface between bone and bioactive glass confirmed nano-osseointegration and unaffected dissolution/reprecipitation mechanisms in the presence of PTH 1-34 functionalization and altered bone metabolism in ORX rats. Quantitative evaluation of the biological response showed promising results in terms of bone repair in ORX rats when using bioactive glass functionalized with PTH 1-34.

In Paper V, a workflow to characterize the bone-bioactive glass interface was demonstrated, introducing 3D analyses at the nanoscale with electron tomography that further corroborated the gradual nature of the interface and highlighted that collagen fibrils are oriented parallel to the interface.

In Paper VI, on-axis Z-contrast electron tomography and EDX tomography were combined for the first time to resolve bone structure and composition at the nanoscale. This provided a direct identification of the low-contrast nanosized spaces seen in the lacy pattern as collagen fibrils. Additionally, it showed the extra-fibrillar mineral to be made of thin platelets merging in larger aggregates spanning over several fibrils.

Future perspectives

The multiscale and multimodal approach adopted in this thesis captured relevant information on bone structure and/or composition in the cases under investigation. However, many of the studies lacked quantitative investigations and statistical comparisons. This was mostly due to the small sample size (n = 1-2) especially in electron microscopy experiments (PFIB-SEM tomography, S/TEM, and electron tomography) [Papers II-VI]. Restrictions in sample size are indirectly related to high experimental costs, as well as lengthy protocols. Automating at least part of the experimental workflow could mitigate these limitations. For example, tools for automating STEM sample preparation by FIB lift-out have already been developed, demonstrating high sample quality and throughput[220]. However, they have yet to be tested on more complex materials like bone and bone-biomaterial interfaces. In the future, it would be interesting to implement these procedures to afford a higher sample size. For example, this would make it possible to examine broader records of MRONJ-affected individual to corroborate the observations in Paper II.

Even with the implementation of automated sample preparation workflows for S/TEM experiments, technical challenges would persist due to the electron beam sensitivity of biological samples like bone. These challenges become especially relevant when high beam doses are required such as in EDX or EELS, and in long experiments such as electron tomography. The compromise between resolution and exposure is exemplified by Paper VI, where large tilt increments and short dwell times were selected for EDX tomography to limit sample damage, albeit leading to sub-optimal EDX maps. Reconstruction algorithms like compressed sensing could be explored in future work, as they allow for under-sampling, requiring fewer projection images to produce high-quality 3D reconstructions[221]. Faster and more sensitive detectors could also mitigate challenges in electron tomography of beam-sensitive materials. As the acquisition of HAADF-STEM tilt series in ~360 s has been shown[222], it would be interesting to apply this fast electron tomography approach to bone.

There are also opportunities to improve tools for image analysis. Deep learning has emerged as a powerful aid to examine features of interest in large/multidimensional datasets, (semi)automating image segmentation to extract quantitative information[223]. However, complex structures like that found in bone at the nanoscale are difficult to be accurately segmented by algorithms. For example, in Paper VI, it was necessary to segment individual mineral plates manually. Improvements in machine learning algorithms could make it possible to analyze features with greater complexity and to examine larger amount of data, while also limiting operator bias in feature selection.

A main limitation of the characterization tools used in Papers III-IV stems from the inability to visualize the biomaterial surface functionalization, i.e., the layer of genistein or PTH 1-34. At this time, it is not possible to determine how much of the drug coating is still present at the time of retrieval, or if it has all been released in the peri-implant space. This could not be determined by EDX due to the similar elements present in both the drugs under investigation and bone, as well as the embedding resin. Other approaches should then be explored. In a previous study, ^{14}C radiolabelling was used to assess the release of bisphosphonates by autoradiography *ex vivo*, correlating the autoradiographs with BSE-SEM images[224]. Hence, similar methodologies based on tagging the therapeutics used in Papers III-IV with easily identifiable signals could be tested.

Apart from technical limitations, some biology-related questions remain unanswered in this thesis, calling for further investigations. In Paper I, mechanistic insights into the origins of the altered microstructure in the LepR-deficient animals are needed, especially to decouple LepR deficiency, obesity, and hyperglycemia, as well as to study bone remodeling, with a specific focus on mineralized cartilage islands. These features should also be examined at smaller length scales, for example by P/FIB-SEM tomography and S/TEM, in particular to highlight how type I and type II collagen interface. In Paper I, structure-function relationships should also be better confirmed, for example by mechanical testing on whole bones. In Paper III, a preclinical study involving a greater sample size should be undertaken to quantify the effect of genistein functionalization on osseointegration, combining microscopy with other analytical techniques as done in Paper IV (e.g., biomechanics, mineralization dynamics, and gene expression).

This thesis mainly focused on assessing changes in bone structure and composition in the presence of disease [Papers I-IV]. In Paper V, a characterization workflow encompassing electron tomography was highlighted, and an advanced electron tomography approach was demonstrated in Paper VI. The high-resolution, artifact-free, 3D reconstruction of bone ultrastructure offered by on-axis electron tomography, especially when correlated with compositional information using EDX tomography, could find broader applications in bone research, for example to probe disease-induced changes in bone quality at the nanoscale.

Lastly, the multimodal and multiscale characterization approach adopted in this thesis only involved *ex situ* analyses. While developments in electron microscopy are aiming to get closer to native and dynamic conditions with liquid imaging[225], they still lack clinical relevance. More work needs to be done to implement materials science characterization workflows in clinically relevant contexts, for example identifying metrics that correlate to those measurable *in vivo*.

Acknowledgements

I have often thought about my PhD as a journey, an analogy also applicable in a literal sense for the several trips back and forth on opposite sides of the Atlantic Ocean. This journey would not have been possible without my three amazing supervisors, who let me fly my own plane, but were always there when I needed them. Thank you to Kathryn, Anders, and Furqan for all the support throughout the years and for emboldening me to fly high. Thank you, Kathryn, for offering me the plane ticket in the first place, for all the research opportunities, and for your encouragement and mentoring beyond the lab. Thank you, Anders, for embarking on this *cotutelle* trip despite all the extra paperwork you had to deal with, for your practical and always on-point advice, and for staying calm during the storms. Thank you, Furqan, for the endless scientific discussions, for sharing your encyclopedic knowledge with me, and for the Friday jokes!

Thank you to all my collaborators, especially Roberta Okamoto and Pedro Gomes-Ferreira at UNESP for taking me aboard very interesting projects. Thank you to Cecilia Larsson Wexell, Le Fu, and Henry Schwarcz for providing me with unique samples to look at. Thank you to Peter Ercius and Alex Lin for hosting me at the Berkeley National Lab in sunny California to take a break from the Hamilton winter with some exciting science. Thank you to Aurélien Gourrier for insightful discussions on bone structure over the years, and to Brian Langelier and Gabe Arcuri for introducing me to the APT world. Thank you to Ariana and Anna for contributing during their summer research internships. A sincere thank you also to Gianluigi Botton for accepting to be a member of my supervisory committee, giving precious feedback on electron microscopy experiments and stimulating ideas to expand my research further.

Thank you to all the technical staff who helped with my research. A special acknowledgement to those at the CCEM – Travis for the great FIB samples, Jhoynner and Chris for SEM advice and help with sample preparation, and Carmen and Natalie for TEM assistance. Thank you to Stefan at CMAL for trusting my microscopy skills. At GU, a special thank you to Lena for sharing her knowledge of bone sample preparation with me, and to Nesrin for thesis writing advice. I am also grateful for all the administrative support received from Samantha and Mary-Anne at McMaster, and from Rosie and Cina at GU.

This journey would have not been the same without my travel companions. Thank you to the GRG team – Alessandra, Joe, Liza, Alyssa, Bryan, Toni, Shane, Jeromy, and all the undergrad students. Covid-19 got in the way for a long time, but we were still able to build memories that I will cherish. Thank you to the fellow PhD travellers at GU – Martina, Paula, Adam, Heithem, Marsel, and Jincy. Thank you for the group therapy sessions during *fika* and for all the carefree and happy moments (especially with food!) we shared.

Thank you to all the other people in the Department of Biomaterials at GU for welcoming me and making me feel like home in Gothenburg – *tack!*

Thank you to my friends outside the lab, especially Dakota and Meghan, for being my first "travel guides" in Canada and for all the memories shared over the years, and Margherita and Federica, with whom I started my journey in the engineering world as first year students. Thank you also to my French family, Elodie, Alex, Lukas, and Myla, for all the fun moments spent together and the meaningful conversations.

An immense thank you to my parents, Emanuela and Renato, and my sister, Elisa, who watched me take off towards far destinations, but never stopped cheering for me, celebrating my achievements along the way. Thank you to my grandma, Delfina, for her unconditional love.

Lastly, thank you to Viktor, my safe harbour during this PhD journey. Thank you for holding my hand during turbulence, for believing in me when I did not, for taking care of me, for encouraging and supporting me even when that brought me away from you. Thank you for listening to my research doubts and ideas, for the occasional Python advice, and for all the proof-reading. Words cannot express how grateful I am to have you as my partner in this journey of life.

Funding acknowledgements. I am grateful for scholarship support from the Ontario Graduate Scholarship, the Blanceflor Foundation, the Mitacs Globalink Research Award, the James F. Harvey and Helen S. Harvey Travel Scholarship, the Yates Scholarship Fund, and the Svenska Sällskapet för Medicinsk Forskning (SSMF). Financial support is also acknowledged from the Swedish Research Council (grant no. 2020-04715), the Swedish state under the agreement between the Swedish government and the county councils (ALF agreement ALFGBG-725641), the Adlerbertska Foundation, the IngaBritt and Arne Lundberg Foundation, the Kungliga Vetenskaps-och Vitterhets-Samhället i Göteborg, the Hjalmar Svensson Foundation, the Västra Götaland Region, the Area of Advance Materials at Chalmers and at the Department of Biomaterials (University of Gothenburg) within the Strategic Research Area initiative launched by the Swedish government, SSMF, the Natural Sciences and Engineering Research Council of Canada (NSERC) (grant no. RGPIN-2020-05722), the Ontario Ministry of Research, Innovation and Science (Early Researcher Award ER17-13-081), the NSERC Alliance International Catalyst Program (grant no. ALLRP 576146-22), the Canada Research Chairs Program, the Academy of Osseointegration, CAPES (Print Project), FINEP (01.12.0530.00 PROINFRA 01/2011), and the São Paulo Research Foundation (FAPESP) (process no. 2015/14688-0, 2017/08187-3, 2021/06849-4, and 2021/13026-4).

References

1. Tortora GJ, Derrickson B. The skeletal system: Bone tissue. In: Principles of anatomy and physiology. Hoboken, NJ: John Wiley & Sons; 2009. p. 175–97.
2. Huiskes R. If bone is the answer, then what is the question? J Anat. 2000;197:145–56.
3. Ritchie RO. The conflicts between strength and toughness. Nat Mater. 2011;10:817–22.
4. Skinner HCW. Biominerals. Mineral Mag. 2005;69:621–41.
5. Currey JD. Bones: Structure and mechanics. Princeton, NJ: Princeton University Press; 2002.
6. Glimcher MJ. Bone: Nature of the calcium phosphate crystals and cellular, structural, and physical chemical mechanisms in their formation. Rev Mineral Geochem. 2006;64:223–82.
7. Weiner S, Wagner HD. The material bone: Structure-mechanical function relations. Annu Rev Mater Sci. 1998;28:271–98.
8. Weiner S, Traub W, Wagner HD. Lamellar bone: Structure-function relations. J Struct Biol. 1999;126:241–55.
9. Reznikov N, Shahar R, Weiner S. Bone hierarchical structure in three dimensions. Acta Biomater. 2014;10:3815–26.
10. Ritchie RO, Buehler MJ, Hansma P. Plasticity and toughness in bone. Phys Today. 2009;62:41–7.
11. Sasaki N, Enyo A. Viscoelastic properties of bone as a function of water content. J Biomech. 1995;28:809–15.
12. Weiner S, Traub W. Bone structure: From ångstroms to microns. FASEB J. 1992;6:879–85.
13. Hulmes DJS. Collagen diversity, synthesis and assembly. In: Fratzl P, editor. Collagen: Structure and mechanics. New York, NY: Springer; 2008. p. 1–13.
14. Hodge AJ, Petruska JA. Recent studies with the electron microscope on ordered aggregates of the tropocollagen macromolecule. In: Ramachandran GN, editor. Aspects of protein structure. New York, NY: Academic Press; 1963. p. 289–300.
15. Orgel JPRO, Miller A, Irving TC, Fischetti RF, Hammersley AP, Wess TJ. The in situ supermolecular structure of type I collagen. Structure. 2001;9:1061–9.
16. Weiner S, Traub W. Organization of hydroxyapatite crystals within collagen fibrils. FEBS Lett. 1986;206:262–6.
17. Landis WJ, Hodgens KJ, Song MJ, Arena J, Kiyonaga S, Marko M, et al. Mineralization of collagen may occur on fibril surfaces: Evidence from conventional and high-voltage electron microscopy and three-dimensional imaging. J Struct Biol. 1996;117:24–35.
18. Landis WJ, Song MJ, Leith A, McEwen L, McEwen BF. Mineral and organic matrix interaction in normally calcifying tendon visualized in 3D by HV EM tomography and graphic image reconstruction. J Struct Biol. 1993;110:39–54.
19. Lees S, Prostak KS, Ingle VK, Kjoller K. The loci of mineral in turkey leg tendon as seen by atomic force microscope and electron microscopy. Calcif Tissue Int. 1994;55:180–9.
20. Pidaparti RMV, Chandran A, Takano Y, Turner CH. Bone mineral lies mainly outside collagen fibrils: Predictions of a composite model for osteonal bone. J Biomech. 1996;29:909–16.
21. Schwarcz HP. The ultrastructure of bone as revealed in electron microscopy of ion-milled sections. Semin Cell Dev Biol. 2015;46:44–50.
22. Buss DJ, Reznikov N, McKee MD. Crossfibrillar mineral tessellation in normal and Hyp mouse bone as revealed by 3D FIB-SEM microscopy. J Struct Biol. 2020;212:107603.
23. Reznikov N, Bilton M, Lari L, Stevens MM, Kröger R. Fractal-like hierarchical organization of bone begins at the nanoscale. Science. 2018;360:eaao2189.
24. Traub W, Arad T, Weiner S. Three-dimensional ordered distribution of crystals in turkey tendon collagen fibers. Proc Natl Acad Sci USA. 1989;86:9822–6.

25. Landis WJ, Hodgens KJ, Arena J, Song MJ, McEwen BF. Structural relations between collagen and mineral in bone as determined by high voltage electron microscopic tomography. Microsc Res Tech. 1996;33:192–202.
26. Robinson RA. An electron-microscopic study of the crystalline inorganic component of bone and its relationship to the organic matrix. J Bone Joint Surg Am. 1952;34-A:389–434.
27. Bocciarelli DS. Morphology of crystallites in bone. Calcif Tissue Res. 1970;5:261–9.
28. Arsenault AL. Crystal-collagen relationships in calcified turkey leg tendons visualized by selected-area dark field electron microscopy. Calcif Tissue Int. 1988;43:202–12.
29. Lees S, Prostak K. The locus of mineral crystallites in bone. Connect Tissue Res. 1988;18:41–54.
30. Fratzl P, Schreiber S, Klaushofer K. Bone mineralization as studied by small-angle X-ray scattering. Connect Tissue Res. 1996;34:247–54.
31. Binkley DM, Deering J, Yuan H, Gourrier A, Grandfield K. Ellipsoidal mesoscale mineralization pattern in human cortical bone revealed in 3D by plasma focused ion beam serial sectioning. J Struct Biol. 2020;212:107615.
32. Buss DJ, Kröger R, McKee MD, Reznikov N. Hierarchical organization of bone in three dimensions: A twist of twists. J Struct Biol X. 2022;6:100057.
33. Micheletti C, Hurley A, Gourrier A, Palmquist A, Tang T, Shah FA, et al. Bone mineral organization at the mesoscale: A review of mineral ellipsoids in bone and at bone interfaces. Acta Biomater. 2022;142:1–13.
34. Boyde A. Electron microscopy of the mineralizing front. Metab Bone Dis Rel Res. 1980;2:69–78.
35. Weiner S, Arad T, Sabanay I, Traub W. Rotated plywood structure of primary lamellar bone in the rat: Orientations of the collagen fibril arrays. Bone. 1997;20:509–14.
36. Wagermaier W, Gupta HS, Gourrier A, Burghammer M, Roschger P, Fratzl P. Spiral twisting of fiber orientation inside bone lamellae. Biointerphases. 2006;1:1–5.
37. Mitchell J, van Heteren AH. A literature review of the spatial organization of lamellar bone. C R Palevol. 2016;15:23–31.
38. Stock SR. The mineral-collagen interface in bone. Calcif Tissue Int. 2015;97:262–80.
39. Schwarcz HP, McNally EA, Botton GA. Dark-field transmission electron microscopy of cortical bone reveals details of extrafibrillar crystals. J Struct Biol. 2014;188:240–8.
40. Allen MR, Burr DB. Bone modeling and remodeling. In: Allen MR, Burr DB, editors. Basic and applied bone biology. London, UK: Academic Press; 2014. p. 75–90.
41. Galea GL, Zein MR, Allen S, Francis-West P. Making and shaping endochondral and intramembranous bones. Dev Dyn. 2021;250:414–49.
42. Hall BK. Bone. In: Bones and cartilage. London, UK: Academic Press; 2015. p. 17–42.
43. Opperman LA. Cranial sutures as intramembranous bone growth sites. Dev Dyn. 2000;219:472–85.
44. Wolff J. The law of bone transformation. Berlin, Germany: Hirschwald; 1892.
45. Bonewald LF. The amazing osteocyte. J Bone Miner Res. 2011;26:229–38.
46. Buckwalter JA, Glimcher MJ, Cooper RR, Recker R. Bone biology – Part I: Structure, blood supply, cells, matrix and mineralization. J Bone Joint Surg Am. 1995;77:1256–75.
47. Buenzli PR, Sims NA. Quantifying the osteocyte network in the human skeleton. Bone. 2015;75:144–50.
48. Dallas SL, Bonewald LF. Dynamics of the transition from osteoblast to osteocyte. Ann NY Acad Sci. 2010;1192:437–43.
49. Pacureanu A, Langer M, Boller E, Tafforeau P, Peyrin F. Nanoscale imaging of the bone cell network with synchrotron X-ray tomography: Optimization of acquisition setup. Med Phys. 2012;39:2229–38.
50. Robling AG, Bonewald LF. The osteocyte: New insights. Annu Rev Physiol. 2020;82:485–506.
51. Li MCM, Chow SKH, Wong RMY, Qin L, Cheung WH. The role of osteocytes-specific molecular mechanism in regulation of mechanotransduction – A systematic review. J Orthop Transl. 2021;29:1–9.

52. Shah FA, Wang X, Thomsen P, Grandfield K, Palmquist A. High-resolution visualization of the osteocyte lacuno-canalicular network juxtaposed to the surface of nanotextured titanium implants in human. ACS Biomater Sci Eng. 2015;1:305–13.
53. Einhorn TA, Gerstenfeld LC. Fracture healing: Mechanisms and interventions. Nat Rev Rheumatol. 2015;11:45–54.
54. Albrektsson T, Brånemark PI, Hansson HA, Lindström J. Osseointegrated titanium implants: Requirements for ensuring a long-lasting, direct bone-to-implant anchorage in man. Acta Orthop Scand. 1981;52:155–70.
55. Grandfield K. Bone, implants, and their interfaces. Phys Today. 2015;68:40–5.
56. Shah FA, Thomsen P, Palmquist A. Osseointegration and current interpretations of the bone-implant interface. Acta Biomater. 2019;84:1–15.
57. Palmquist A. A multiscale analytical approach to evaluate osseointegration. J Mater Sci Mater Med. 2018;29:60.
58. Grandfield K, Palmquist A, Engqvist H. Three-dimensional structure of laser-modified Ti6Al4V and bone interface revealed with STEM tomography. Ultramicroscopy. 2013;127:48–52.
59. Shah FA, Nilson B, Brånemark R, Thomsen P, Palmquist A. The bone-implant interface – Nanoscale analysis of clinically retrieved dental implants. Nanomedicine. 2014;10:1729–37.
60. Shah FA, Thomsen P, Palmquist A. A review of the impact of implant biomaterials on osteocytes. J Dent Res. 2018;97:977–86.
61. Davies JE. Understanding peri-implant endosseous healing. J Dent Educ. 2003;67:932–49.
62. Niinomi M. Mechanical properties of biomedical titanium alloys. Mater Sci Eng. 1998;243:231–6.
63. Kasemo B. Biocompatibility of titanium implants: Surface science aspects. J Prosthet Dent. 1983;49:832–7.
64. Bauer S, Schmuki P, von der Mark K, Park J. Engineering biocompatible implant surfaces. Part I: Materials and surfaces. Prog Mater Sci. 2013;58:261–326.
65. Palmquist A, Lindberg F, Emanuelsson L, Brånemark R, Engqvist H, Thomsen P. Biomechanical, histological, and ultrastructural analyses of laser micro- and nano-structured titanium alloy implants: A study in rabbit. J Biomed Mater Res A. 2010;92A:1476–86.
66. Davies JE, Ajami E, Moineddin R, Mendes VC. The roles of different scale ranges of surface implant topography on the stability of the bone/implant interface. Biomaterials. 2013;34:3535–46.
67. Davies JE, Mendes VC, Ko JCH, Ajami E. Topographic scale-range synergy at the functional bone/implant interface. Biomaterials. 2014;35:25–35.
68. Pyka G, Burakowski A, Kerckhofs G, Moesen M, van Bael S, Schrooten J, et al. Surface modification of Ti6Al4V open porous structures produced by additive manufacturing. Adv Eng Mater. 2012;14:363–70.
69. Heinl P, Müller L, Körner C, Singer RF, Müller FA. Cellular Ti-6Al-4V structures with interconnected macro porosity for bone implants fabricated by selective electron beam melting. Acta Biomater. 2008;4:1536–44.
70. Palmquist A, Jolic M, Hryha E, Shah FA. Complex geometry and integrated macro-porosity: Clinical applications of electron beam melting to fabricate bespoke bone-anchored implants. Acta Biomater. 2023;156:125–45.
71. Koschwanez HE, Reichert WM. Textured and porous materials. In: Ratner BR, Hoffman AS, Schoen FJ, Lemons JE, editors. Biomaterials science: An introduction to materials in medicine. Oxford, UK: Academic Press; 2013. p. 321–31.
72. Wang Z, Wang C, Li C, Qin Y, Zhong L, Chen B, et al. Analysis of factors influencing bone ingrowth into three-dimensional printed porous metal scaffolds: A review. J Alloy Compd. 2017;717:271–85.
73. Hench LL. The story of Bioglass®. J Mater Sci Mater Med. 2006;17:967–78.
74. Tadjoedin ES, de Lange GL, Lyaruu DM, Kuiper L, Burger EH. High concentrations of bioactive glass material (BioGran®) vs. autogenous bone for sinus floor elevation. Clin Oral Impl Res. 2002;13:428–36.

75. Hench LL, Andersson Ö. Bioactive glasses. In: Hench LL, Wilson J, editors. An introduction to bioceramics. Singapore: World Scientific; 1993. p. 41–62. (McLaren M, Niesz DE, editors. Advanced series in ceramics; vol. 1).
76. Schepers E, de Clercq M, Ducheyene P, Kempeneers P. Bioactive glass particulate material as a filler for bone lesions. J Oral Rehabil. 1991;18:439–52.
77. Kunrath MF, Shah FA, Dahlin C. Bench-to-bedside: Feasibility of nano-engineered and drug-delivery biomaterials for bone-anchored implants and periodontal applications. Mater Today Bio. 2023;18:100540.
78. Kyllönen L, D'Este M, Alini M, Eglin D. Local drug delivery for enhancing fracture healing in osteoporotic bone. Acta Biomater. 2015;11:412–34.
79. Bai H, Cui Y, Wang C, Wang Z, Luo W, Liu Y, et al. 3D printed porous biomimetic composition sustained release zoledronate to promote osteointegration of osteoporotic defects. Mater Design. 2020;189:108513.
80. Kanis JA, McCloskey EV, Johansson H, Oden A, Melton LJ, Khaltaev N. A reference standard for the description of osteoporosis. Bone. 2008;42:467–75.
81. Bouxsein ML. Bone quality: Where do we go from here? Osteoporos Int. 2003;14:118–27.
82. Seeman E, Delmas PD. Bone quality – The material and structural basis of bone strength and fragility. N Engl J Med. 2006;354:2250–61.
83. Boskey AL, Imbert L. Bone quality changes associated with aging and disease: A review. Ann NY Acad Sci. 2017;1410:93–106.
84. Muñoz A, Docaj A, Ugarteburu M, Carriero A. Poor bone matrix quality: What can be done about it? Curr Osteoporos Rep. 2021;19:510–31.
85. World Health Organization. Classification of diabetes mellitus. 2019.
86. World Health Organization. Global report on diabetes. 2016.
87. Zimmet P, Alberti KGMM, Shaw J. Global and societal implications of the diabetes epidemic. Nature. 2001;414:782–7.
88. Eckel RH, Grundy SM, Zimmet PZ. The metabolic syndrome. Lancet. 2005;365:1415–28.
89. Vestergaard P. Discrepancies in bone mineral density and fracture risk in patients with type 1 and type 2 diabetes—a meta-analysis. Osteoporos Int. 2007;18:427–44.
90. Schwartz AV, Vittinghoff E, Sellmeyer D, Feingold K, de Rekeneire N, Strotmeyer ES, et al. Diabetes-related complications, glycemic control, and falls in older adults. Diabetes Care. 2008;31:391–6.
91. Lekkala S, Taylor EA, Hunt HB, Donnelly E. Effects of diabetes on bone material properties. Curr Osteoporos Rep. 2019;17:455–64.
92. Reid IR. Fat and bone. Arch Biochem Biophys. 2010;503:20–7.
93. Harada S, Rodan GA. Control of osteoblast function and regulation of bone mass. Nature. 2003;423:349–55.
94. Frost HM. Bone's mechanostat: A 2003 update. Anat Rec. 2003;275A:1081–101.
95. Saito M, Kida Y, Kato S, Marumo K. Diabetes, collagen, and bone quality. Curr Osteoporos Rep. 2014;12:181–8.
96. Yamagishi S. Role of advanced glycation end products (AGEs) and receptor for AGEs (RAGE) in vascular damage in diabetes. Exp Gerontol. 2011;46:217–24.
97. Cao JJ. Effects of obesity on bone metabolism. J Orthop Surg Res. 2011;6:30.
98. Yamamoto M, Sugimoto T. Advanced glycation end products, diabetes, and bone strength. Curr Osteoporos Rep. 2016;14:320–6.
99. Hamada Y, Fujii H, Fukagawa M. Role of oxidative stress in diabetic bone disorder. Bone. 2009;45:S35–8.
100. Halade GV, Jamali AE, Williams PJ, Fajardo RJ, Fernandes G. Obesity-mediated inflammatory microenvironment stimulates osteoclastogenesis and bone loss in mice. Exp Gerontol. 2011;46:43–52.
101. Tartaglia LA. The leptin receptor. J Biol Chem. 1997;272:6093–6.
102. Reid IR, Baldock PA, Cornish J. Effects of leptin on the skeleton. Endocr Rev. 2018;39:938–59.
103. Burguera B, Hofbauer LC, Thomas T, Gori F, Evans GL, Khosla S, et al. Leptin reduces ovariectomy-induced bone loss in rats. Endocrinology. 2001;142:3546–53.

104. Bartell SM, Rayalam S, Ambati S, Gaddam DR, Hartzell DL, Hamrick M, et al. Central (ICV) leptin injection increases bone formation, bone mineral density, muscle mass, serum IGF-1, and the expression of osteogenic genes in leptin-deficient ob/ob mice. J Bone Miner Res. 2011;26:1710–20.
105. King A, Austin A. Animal models of type 1 and type 2 diabetes mellitus. In: Conn PM, editor. Animal models for the study of human disease. London, UK: Academic Press; 2017. p. 245–65.
106. Montague CT, Farooqi IS, Whitehead JP, Soos MA, Rau H, Wareham NJ, et al. Congenital leptin deficiency is associated with severe early-onset obesity in humans. Nature. 1997;387:903–8.
107. Clément K, Vaisse C, Lahlou N, Cabrol S, Pelloux V, Cassuto D, et al. A mutation in the human leptin receptor gene causes obesity and pituitary dysfunction. Nature. 1998;392:398–401.
108. Farooqi IS, Wangensteen T, Collins S, Kimber W, Matarese G, Keogh JM, et al. Clinical and molecular genetic spectrum of congenital deficiency of the leptin receptor. N Engl J Med. 2007;356:237–47.
109. Farooqi IS, O'Rahilly S. 20 years of leptin: Human disorders of leptin action. J Endocrinol. 2014;223:T63–70.
110. Gomez MF, Åkesson L, Lernmark Å. A new rat model for diabetic vascular complications. Patent application WO-2015044339-A1.
111. Consensus development conference. Diagnosis, prophylaxis, and treatment of osteoporosis. Am J Medicine. 1993;94:646–50.
112. Ettinger MP. Aging bone and osteoporosis: Strategies for preventing fractures in the elderly. Arch Intern Med. 2003;163:2237–46.
113. Amin S, Achenbach SJ, Atkinson EJ, Khosla S, Melton LJ. Trends in fracture incidence: A population-based study over 20 years. J Bone Miner Res. 2014;29:581–9.
114. World Health Organization. Ageing and health [Internet]. 2022. Available from: https://www.who.int/news-room/fact-sheets/detail/ageing-and-health
115. Khosla S, Oursler MJ, Monroe DG. Estrogen and the skeleton. Trends Endocrinol Metab. 2012;23:576–81.
116. Riggs BL, Khosla S, Melton LJ. Sex steroids and the construction and conservation of the adult skeleton. Endocr Rev. 2002;23:279–302.
117. Khosla S, Melton LJ, Atkinson EJ, O'Fallon WM, Klee GG, Riggs BL. Relationship of serum sex steroid levels and bone turnover markers with bone mineral density in men and women: A key role for bioavailable estrogen. J Clin Endocrinol Metab. 1998;83:2266–74.
118. Daniell HW, Dunn SR, Ferguson DW, Lomas G, Niazi Z, Stratte PT. Progressive osteoporosis during androgen deprivation therapy for prostate cancer. J Urol. 1999;163:181–6.
119. Preston DM, Torréns JI, Harding P, Howard RS, Duncan WE, Mcleod DG. Androgen deprivation in men with prostate cancer is associated with an increased rate of bone loss. Prostate Cancer Prostatic Dis. 2002;5:304–10.
120. Kalu DN. The ovariectomized rat model of postmenopausal bone loss. Bone Miner. 1991;15:175–91.
121. Bonucci E, Ballanti P. Osteoporosis – Bone remodeling and animal models. Toxicol Pathol. 2014;42:957–69.
122. Wakley GK, Schutte HD, Hannon KS, Turner RT. Androgen treatment prevents loss of cancellous bone in the orchidectomized rat. J Bone Miner Res. 1991;6:325–30.
123. Giro G, Chambrone L, Goldstein A, Rodrigues JA, Zenobio E, Feres M, et al. Impact of osteoporosis in dental implants: A systematic review. World J Orthop. 2015;6:311–5.
124. Javed F, Ahmed HB, Crespi R, Romanos GE. Role of primary stability for successful osseointegration of dental implants: Factors of influence and evaluation. Interv Med Appl Sci. 2013;5:162–7.
125. Franchi M, Fini M, Giavaresi G, Ottani V. Peri-implant osteogenesis in health and osteoporosis. Micron. 2005;36:630–44.
126. Dereka X, Calciolari E, Donos N, Mardas N. Osseointegration in osteoporotic-like condition: A systematic review of preclinical studies. J Periodontal Res. 2018;53:933–40.

127. de Medeiros FCFL, Kudo GAH, Leme BG, Saraiva PP, Verri FR, Honório HM, et al. Dental implants in patients with osteoporosis: A systematic review with meta-analysis. Int J Oral Maxillofac Surg . 2018;47:480–91.
128. Russell RGG. Bisphosphonates: The first 40 years. Bone. 2011;49:2–19.
129. Reznikov N, Steele JAM, Fratzl P, Stevens MM. A materials science vision of extracellular matrix mineralization. Nat Rev Mater. 2016;1:16041.
130. Russell RGG, Mühlbauer RC, Bisaz S, Williams DA, Fleisch H. The influence of pyrophosphate, condensed phosphates, phosphonates and other phosphate compounds on the dissolution of hydroxyapatite in vitro and on bone resorption induced by parathyroid hormone in tissue culture and in thyroparathyroidectomised rats. Calcif Tissue Res. 1970;6:183–96.
131. Fleisch H. Diphosphonates: History and mechanisms of action. Metab Bone Dis Relat Res. 1981;3:279–87.
132. Million Women Study Collaborators. Breast cancer and hormone-replacement therapy in the Million Women Study. Lancet. 2003;362:419–27.
133. Adlercreutz H. Phytoestrogens: Epidemiology and a possible role in cancer protection. Environ Health Perspect. 1995;103:103–12.
134. Marini H, Minutoli L, Polito F, Bitto A, Altavilla D, Atteritano M, et al. Effects of the phytoestrogen genistein on bone metabolism in osteopenic postmenopausal women: A randomized trial. Ann Intern Med. 2007;146:839.
135. Hodsman AB, Bauer DC, Dempster DW, Dian L, Hanley DA, Harris ST, et al. Parathyroid hormone and teriparatide for the treatment of osteoporosis: A review of the evidence and suggested guidelines for its use. Endocr Rev. 2005;26:688–703.
136. Canalis E. Management of endocrine disease: Novel anabolic treatments for osteoporosis. Eur J Endocrinol. 2018;178:R33–44.
137. Bilezikian JP. Osteonecrosis of the jaw – Do bisphosphonates pose a risk? N Engl J Med. 2006;335:2278–81.
138. Reid IR. Osteonecrosis of the jaw – Who gets it, and why? Bone. 2009;44:4–10.
139. Ruggiero SL. Bisphosphonate-related osteonecrosis of the jaw (BRONJ): Initial discovery and subsequent development. J Oral Maxillofac Surg. 2009;67:13–8.
140. Ruggiero SL, Dodson TB, Aghaloo T, Carlson ER, Ward BB, Kademani D. American Association of Oral and Maxillofacial Surgeons' position paper on medication-related osteonecrosis of the jaw – 2022 update. J Oral Maxillofac Surg. 2022;80:920–43.
141. Drake MT, Clarke BL, Khosla S. Bisphosphonates: Mechanism of action and role in clinical practice. Mayo Clin Proc. 2008;83:1032–45.
142. Reid IR, Cornish J. Epidemiology and pathogenesis of osteonecrosis of the jaw. Nat Rev Rheumatol. 2012;8:90–6.
143. Allen MR, Burr DB. The pathogenesis of bisphosphonate-related osteonecrosis of the jaw: So many hypotheses, so few data. J Oral Maxillofac Surg. 2009;67:61–70.
144. Hinson AM, Smith CW, Siegel ER, Stack BC. Is bisphosphonate-related osteonecrosis of the jaw an infection? A histological and microbiological ten-year summary. Int J Dent. 2014;2014:452737.
145. Georgiadis M, Müller R, Schneider P. Techniques to assess bone ultrastructure organization: Orientation and arrangement of mineralized collagen fibrils. J R Soc Interface. 2016;13:20160088.
146. Binkley DM, Grandfield K. Advances in multiscale characterization techniques of bone and biomaterials interfaces. ACS Biomater Sci Eng. 2017;4:3678–90.
147. Dempster DW, Compston JE, Drezner MK, Glorieux FH, Kanis JA, Malluche H, et al. Standardized nomenclature, symbols, and units for bone histomorphometry: A 2012 update of the report of the ASBMR Histomorphometry Nomenclature Committee. J Bone Miner Res. 2013;28:2–17.
148. Orhan K, editor. Micro-computed tomography (micro-CT) in medicine and engineering. Cham, Switzerland: Springer Nature; 2020.
149. Bouxsein ML, Boyd SK, Christiansen BA, Guldberg RE, Jepsen KJ, Müller R. Guidelines for assessment of bone microstructure in rodents using micro-computed tomography. J Bone Miner Res. 2010;25:1468–86.

150. Li JY, Pow EHN, Zheng LW, Ma L, Kwong DLW, Cheung LK. Quantitative analysis of titanium-induced artifacts and correlated factors during micro-CT scanning. Clin Oral Impl Res. 2014;25:506–10.
151. Palmquist A, Shah FA, Emanuelsson L, Omar O, Suska F. A technique for evaluating bone ingrowth into 3D printed, porous Ti6Al4V implants accurately using X-ray micro-computed tomography and histomorphometry. Micron. 2017;94:1–8.
152. Goldstein JI, Newbury DE, Michael JR, Ritchie NWM, Scott JHJ, Joy DC. Scanning electron microscopy and X-ray microanalysis. New York, NY: Springer; 2018.
153. Williams DB, Carter CB. Transmission electron microscopy. New York, NY: Springer; 2009.
154. Shah FA, Ruscsák K, Palmquist A. 50 years of scanning electron microscopy of bone – A comprehensive overview of the important discoveries made and insights gained into bone material properties in health, disease, and taphonomy. Bone Res. 2019;7:15.
155. Roschger P, Fratzl P, Eschberger J, Klaushofer K. Validation of quantitative backscattered electron imaging for the measurement of mineral density distribution in human bone biopsies. Bone. 1998;23:319–26.
156. Shah FA, Ruscsák K, Palmquist A. Transformation of bone mineral morphology: From discrete marquise-shaped motifs to a continuous interwoven mesh. Bone Rep. 2020;13:100283.
157. Sato M, Shah FA. Contributions of resin cast etching to visualising the osteocyte lacuno-canalicular network architecture in bone biology and tissue engineering. Calcif Tissue Int. 2023;112:525–542.
158. Shah FA, Johansson ML, Omar O, Simonsson H, Palmquist A, Thomsen P. Laser-modified surface enhances osseointegration and biomechanical anchorage of commercially pure titanium implants for bone-anchored hearing systems. PLOS One. 2016;11:e0157504.
159. Cantoni M, Holzer L. Advances in 3D focused ion beam tomography. MRS Bull. 2014;39:354–60.
160. Burnett TL, Kelley R, Winiarski B, Contreras L, Daly M, Gholinia A, et al. Large volume serial section tomography by Xe Plasma FIB dual beam microscopy. Ultramicroscopy. 2016;161:119–29.
161. Reznikov N, Almany-Magal R, Shahar R, Weiner S. Three-dimensional imaging of collagen fibril organization in rat circumferential lamellar bone using a dual beam electron microscope reveals ordered and disordered sub-lamellar structures. Bone. 2013;52:676–83.
162. Reznikov N, Shahar R, Weiner S. Three-dimensional structure of human lamellar bone: The presence of two different materials and new insights into the hierarchical organization. Bone. 2014;59:93–104.
163. Tang T, Landis W, Raguin E, Werner P, Bertinetti L, Dean M, et al. A 3D network of nanochannels for possible ion and molecule transit in mineralizing bone and cartilage. Adv Nanobiomed Res. 2022;2:2100162.
164. Tang T, Landis W, Blouin S, Bertinetti L, Hartmann MA, Berzlanovich A, et al. Subcanalicular nanochannel volume is inversely correlated with calcium content in human cortical bone. J Bone Miner Res. 2023;38:313–25.
165. Giannuzzi LA, Giannuzzi NJ, Capuano MJ. FIB, SEM, and TEM of bone/dental implant interfaces. Microsc Microanal. 2005;11:998–9.
166. Grandfield K, Engqvist H. Focused ion beam in the study of biomaterials and biological matter. Adv Mater Sci Eng. 2012;2012:1–6.
167. Pennycook SJ. Z-contrast STEM for materials science. Ultramicroscopy. 1989;30:58–69.
168. Jantou V, Turmaine M, West GD, Horton MA, McComb DW. Focused ion beam milling and ultramicrotomy of mineralised ivory dentine for analytical transmission electron microscopy. Micron. 2009;40:495–501.
169. McNally EA, Schwarcz HP, Botton GA, Arsenault AL. A model for the ultrastructure of bone based on electron microscopy of ion-milled sections. PLOS One. 2012;7:e29258.
170. Grandfield K, Vuong V, Schwarcz HP. Ultrastructure of bone: Hierarchical features from nanometer to micrometer scale revealed in focused ion beam sections in the TEM. Calcif Tissue Int. 2018;103:606–16.

171. Palmquist A, Grandfield K, Norlindh B, Mattsson T, Brånemark R, Thomsen P. Bone-titanium oxide interface in humans revealed by transmission electron microscopy and electron tomography. J R Soc Interface. 2012;9:396–400.
172. Grandfield K, Palmquist A, Ericson F, Malmström J, Emanuelsson L, Slotte C, et al. Bone response to free-form fabricated hydroxyapatite and zirconia scaffolds: A transmission electron microscopy study in the human maxilla. Clin Implant Dent Relat Res. 2012;14:461–9.
173. Bals S, van Aert S, van Tendeloo G. High resolution electron tomography. Curr Opin Solid State Mater Sci. 2013;17:107–14.
174. Ercius P, Alaidi O, Rames MJ, Ren G. Electron tomography: A three-dimensional analytic tool for hard and soft materials research. Adv Mater. 2015;27:5638–63.
175. Kawase N, Kato M, Nishioka H, Jinnai H. Transmission electron microtomography without the "missing wedge" for quantitative structural analysis. Ultramicroscopy. 2007;107:8–15.
176. Midgley PA, Weyland M. 3D electron microscopy in the physical sciences: The development of Z-contrast and EFTEM tomography. Ultramicroscopy. 2003;96:413–31.
177. McNally E, Nan F, Botton GA, Schwarcz HP. Scanning transmission electron microscopic tomography of cortical bone using Z-contrast imaging. Micron. 2013;49:46–53.
178. Grandfield K, Palmquist A, Engqvist H. High-resolution three-dimensional probes of biomaterials and their interfaces. Philos Trans A Math Phys Eng Sci. 2012;370:1337–51.
179. Wang X, Shah FA, Palmquist A, Grandfield K. 3D characterization of human nano-osseointegration by on-axis electron tomography without the missing wedge. ACS Biomater Sci Eng. 2017;3:49–55.
180. Pasteris JD, Beyssac O. Welcome to Raman spectroscopy: Successes, challenges, and pitfalls. Elements. 2020;16:87–92.
181. Morris MD, Mandair GS. Raman assessment of bone quality. Clin Orthop Relat Res. 2011;469:2160–9.
182. Gamsjaeger S, Masic A, Roschger P, Kazanci M, Dunlop JWC, Klaushofer K, et al. Cortical bone composition and orientation as a function of animal and tissue age in mice by Raman spectroscopy. Bone. 2010;47:392–9.
183. Grandfield K, Gustafsson S, Palmquist A. Where bone meets implant: The characterization of nano-osseointegration. Nanoscale. 2013;5:4302–8.
184. Egerton RF. Electron energy-loss spectroscopy in the electron microscope. New York, NY: Springer; 2011.
185. Jantou-Morris V, Horton MA, McComb DW. The nano-morphological relationships between apatite crystals and collagen fibrils in ivory dentine. Biomaterials. 2010;31:5275–86.
186. Lee BEJ, Luo L, Grandfield K, Andrei CM, Schwarcz HP. Identification of collagen fibrils in cross sections of bone by electron energy loss spectroscopy (EELS). Micron. 2019;124:102706.
187. Wang X, Langelier B, Shah FA, Korinek A, Bugnet M, Hitchcock AP, et al. Biomineralization at titanium revealed by correlative 4D tomographic and spectroscopic methods. Adv Mater Interfaces. 2018;5:1800262.
188. Janvier Labs. Lund MetS rat [Internet]. 2019. Available from: https://janvier-labs.com/en/fiche_produit/lund-mets_rat/
189. Gomes-Ferreira PHS, Lisboa-Filho PN, da Silva AC, Bim-júnior O, de Souza Batista FR, Silva ACE, et al. Sonochemical time standardization for bioactive materials used in perimplantar defects filling. Ultrason Sonochem. 2019;56:437–46.
190. Jarmar T, Palmquist A, Brånemark R, Hermansson L, Engqvist H, Thomsen P. Technique for preparation and characterization in cross-section of oral titanium implant surfaces using focused ion beam and transmission electron microscopy. J Biomed Mater Res A. 2008;87A:1003–9.
191. Li C, Habler G, Baldwin LC, Abart R. An improved FIB sample preparation technique for site-specific plan-view specimens: A new cutting geometry. Ultramicroscopy. 2018;184:310–7.
192. Huang J, Wang X, Grandfield K. FIB preparation of bone-implant interfaces for correlative on-axis rotation electron tomography and atom probe tomography. Microsc Microanal. 2014;20:352–3.

193. Buie HR, Campbell GM, Klinck RJ, MacNeil JA, Boyd SK. Automatic segmentation of cortical and trabecular compartments based on a dual threshold technique for in vivo micro-CT bone analysis. Bone. 2007;41:505–15.
194. Schindelin J, Arganda-Carreras I, Frise E, Kaynig V, Longair M, Pietzsch T, et al. Fiji: An open-source platform for biological-image analysis. Nat Methods. 2012;9:676–82.
195. Möbus G, Inkson BJ. Nanoscale tomography in materials science. Mater Today. 2007;10:18–25.
196. Grandfield K, Micheletti C, Deering J, Arcuri G, Tang T, Langelier B. Atom probe tomography for biomaterials and biomineralization. Acta Biomater. 2022;148:44–60.
197. Gomez MF, Silvola J, Berglund LM, Kiugel M, Åkesson L, Knuuti J, et al. Cardiac hypertrophy and oxidative metabolism in novel congenic leptin receptor deficient BBDR.cg-lepr.cp rats. FASEB J. 2014;28:1155.10.
198. Berglund L, Åkesson L, Garcia-Vaz E, Zetterqvist A, Kotova O, Andersson AD, et al. Diabetes complications in congenic leptin receptor deficient BBDR.cg-lepr.cp rats. FASEB J. 2014;28:1072.6.
199. Wancket LM. Animal models for evaluation of bone implants and devices. Vet Pathol. 2015;52:842–50.
200. Reinwald S, Peterson RG, Allen MR, Burr DB. Skeletal changes associated with the onset of type 2 diabetes in the ZDF and ZDSD rodent models. Am J Physiol Endocrinol Metab. 2009;296:E765–74.
201. Tamasi JA, Arey BJ, Bertolini DR, Feyen JH. Characterization of bone structure in leptin receptor-deficient Zucker (fa/fa) rats. J Bone Miner Res. 2003;18:1605–11.
202. Zeitoun D, Caliaperoumal G, Bensidhoum M, Constans JM, Anagnostou F, Bousson V. Microcomputed tomography of the femur of diabetic rats: Alterations of trabecular and cortical bone microarchitecture and vasculature – A feasibility study. Eur Radiol Exp. 2019;3:17.
203. McCabe L, Zhang J, Raehtz S. Understanding the skeletal pathology of type 1 and 2 diabetes mellitus. Crit Rev Eukaryot Gene Expr. 2011;21:187–206.
204. Shipov A, Zaslansky P, Riesemeier H, Segev G, Atkins A, Shahar R. Unremodeled endochondral bone is a major architectural component of the cortical bone of the rat (Rattus norvegicus). J Struct Biol. 2013;183:132–40.
205. Bach-Gansmo FL, Irvine SC, Brüel A, Thomsen JS, Birkedal H. Calcified cartilage islands in rat cortical bone. Calcif Tissue Int. 2013;92:330–8.
206. Allen MR, McNerny EM, Organ JM, Wallace JM. True gold or pyrite: A review of reference point indentation for assessing bone mechanical properties in vivo. J Bone Miner Res. 2015;30:1539–50.
207. Shah FA. Micro-Raman spectroscopy reveals the presence of octacalcium phosphate and whitlockite in association with bacteria-free zones within the mineralized dental biofilm. Microsc Microanal. 2019;25:129–34.
208. Deering J, Chen J, Mahmoud D, Tang T, Lin Y, Fang Q, et al. Characterizing mineral ellipsoids in new bone formation at the interface of Ti6Al4V porous implants. bioRxiv. 2023;2023.01.20.524810.
209. Hench LL, Paschall HA. Direct chemical bond of bioactive glass-ceramic materials to bone and muscle. J Biomed Mater Res. 1973;4:25–42.
210. Puleo DA, Nanci A. Understanding and controlling the bone-implant interface. Biomaterials. 1999;20:2311–21.
211. Möbus G, Doole RC, Inkson BJ. Spectroscopic electron tomography. Ultramicroscopy. 2003;96:433–51.
212. Collins SM, Midgley PA. Progress and opportunities in EELS and EDS tomography. Ultramicroscopy. 2017;180:133–41.
213. Schwarcz HP, Abueidda D, Jasiuk I. The ultrastructure of bone and its relevance to mechanical properties. Front Phys. 2017;5:39.
214. Cressey BA, Cressey G. A model for the composite nanostructure of bone suggested by high-resolution transmission electron microscopy. Mineral Mag. 2003;67:1171–82.

215. Macías-Sánchez E, Tarakina NV, Ivanov D, Blouin S, Berzlanovich AM, Fratzl P. Spherulitic crystal growth drives mineral deposition patterns in collagen-based materials. Adv Funct Mater. 2022;32:2200504.
216. Gault B, Chiaramonti A, Cojocaru-Mirédin O, Stender P, Dubosq R, Freysoldt C, et al. Atom probe tomography. Nat Rev Methods Primers. 2021;1:51.
217. Lee BEJ, Langelier B, Grandfield K. Visualization of collagen-mineral arrangement using atom probe tomography. Adv Biol. 2021;5:2100657.
218. Karlsson J, Sundell G, Thuvander M, Andersson M. Atomically resolved tissue integration. Nano Lett. 2014;14:4220–3.
219. Sundell G, Dahlin C, Andersson M, Thuvander M. The bone-implant interface of dental implants in humans on the atomic scale. Acta Biomater. 2017;48:445–50.
220. Tsurusawa H, Nakanishi N, Kawano K, Chen Y, Dutka M, Leer BV, et al. Robotic fabrication of high-quality lamellae for aberration-corrected transmission electron microscopy. Sci Rep. 2021;11:21599.
221. Leary R, Saghi Z, Midgley PA, Holland DJ. Compressed sensing electron tomography. Ultramicroscopy. 2013;131:70–91.
222. Albrecht W, Bals S. Fast electron tomography for nanomaterials. J Phys Chem C. 2020;124:27276–86.
223. Reznikov N, Buss DJ, Provencher B, McKee MD, Piché N. Deep learning for 3D imaging and image analysis in biomineralization research. J Struct Biol. 2020;212:107598.
224. Karlsson J, Harmankaya N, Allard S, Palmquist A, Halvarsson M, Tengvall P, et al. Ex vivo alendronate localization at the mesoporous titania implant/bone interface. J Mater Sci Mater Med. 2015;26:11.
225. Kelly DF, DiCecco LA, Jonaid GM, Dearnaley WJ, Spilman MS, Gray JL, et al. Liquid-EM goes viral – Visualizing structure and dynamics. Curr Opin Struct Biol. 2022;75:102426.